공학박사 학위논문

Constructing Initial Models for Full Waveform Inversion using Strip-off Controlled Directional Reception Velocity Analysis

Strip-off CDR 속도분석법을 이용한

완전파형역산 초기모델 구축

2016 년 8 월

서울대학교 대학원

협동과정 계산과학전공

박 은 진

Abstract

The controlled directional reception (CDR) method is a velocity analysis method using ray-tracing. It is one of the tomographic methods that use slope (or ray parameter), so it is often called the "slope tomography method". It does not require a pre-picking operation like traveltime tomography does. Auto-picked information from the local slant stack is regarded as more reliable than reflection traveltime picked directly from the seismic data. The method also provides more detailed information about the moveout than the imaging operator in migration-based velocity analysis (MVA). Therefore, we constructed a velocity macro-model using this strip-off CDR velocity analysis. When compared to the conventional CDR method, it increased the resolution of common receiver gathers (CRG) data and reduced computer storage space dramatically. Additionally, it improved the accuracy of the velocity model by using the migrated image as a background panel during the velocity analysis.

The results obtained by this method were applied to full waveform inversion (FWI) as the initial velocity model. In FWI, an exact initial model is important because it reduces instability and increases the probability of convergence to the global minimum. It is significant that the CDR model is first applied as the initial model of FWI. We confirmed good inverted results from two realistic synthetic data tests by comparison with the results obtained using the conventional Laplace inverted model and the linearly increasing model. In addition, the CDR macro-model has strength to seismic data with a weathered layer or short offset. Furthermore, it is possible to apply to multi-parameter inversion. Finally, we performed this method on real seismic data. Although we could not know the true velocity model for the real seismic data, we confirmed that the RMS error of the CDR model was

lower than that of the Laplace inverted model. Additionally, the migrated images and common image gathers (CIGs) also proved that the inverted CDR model showed a good result.

Strip-off CDR velocity analysis has a disadvantage in computing time compared with Laplace domain inversion. However, even if the computation time is greater, the method has great value because of its high accuracy. In particular, it is expected to provide good results with difficult data, such as seismic data with a weathered zone or short offset, and so increase the accuracy compared with the conventional method. CDR velocity analysis also may be useful for work favoring higher accuracy over fast calculation time, such as some resource exploration and geological surveying. Furthermore, the good initial model can reduce computing time for inversion as well as increase the accuracy of the inverted results.

In summary, the macro-model obtained from strip-off CDR velocity analysis is suitable for frequency domain FWI. Three-dimensional exploration and exploration in complex terrains are being conducted more often, so seismic data with short offset or recording time are also encountered more frequently. This method will demonstrate strength with these seismic data. Additionally, it can be expected to be applicable to land seismic or ocean bottom seismic (OBS) data and also extend into other inversion fields such as multi-parameter inversion.

Keywords : Controlled directional reception, Velocity analysis, Initial model, Full waveform inversion, ray parameter

Student Number : 2012-30115

Table of Contents

List of Tables

List of Figures

1. Introduction

Full waveform inversion (FWI) is a technique for deriving a subsurface velocity model from acquired seismic data, and this field has been widely studied since the 1980's (Lailly, 1983; Tarantola, 1984; Bunks et al., 1995; Pratt et al., 1998; Operto et al., 2004; Shin and Min, 2006; Warner et al., 2013). However, it still has a lot of difficulties because it is an ill-posed problem (Tarantola, 1984; Pratt, 1999). This problem is mostly caused by noise in the seismic data, the limited bandwidth of the shots and the incomplete information of the subsurface provided by seismic exploration (Prieux et al., 2012). Therefore, it is a very difficult task to find accurate subsurface velocity model with only observed acquisition data. However, many ways to challenge the ill-posed problem of FWI have been devised. There are two main method: one is obtaining low frequencies in the field (Moldoveanu et al., 2007; Bagaini, 2008; Tsingas et al., 2015) and the other is constructing accurate initial velocity model (Chauris et al., 2008; Prieux et al., 2012). 'Initial velocity model' is one of the important factors to be considered in FWI. The results of FWI are significantly influenced by an initial velocity model (Shin and Ha, 2008; Prieux et al., 2012), same as in setting starting point in the maze. If the starting point is close to the target point, it is easy to find the goal. On the contrary, if you start near a trap it is likely that you fall into it. The goal of the FWI is to find global minima. Good initial velocity model increases the probability of convergence to the global minima avoiding local minima.

In the case of finding a subsurface structure using the wave

propagation information of observed seismic data – especially data with only short-angle reflections, it is good to go through a two-step process (Ravaut et al., 2004). The first step is building a macro-model or background model, and the second step is finding the short wavelength or high frequency component by using the macro-model of the first step. In the technique of velocity modeling, the first process can be called initial velocity model building phase. It is very difficult to connect seismic traces with the velocity model because it has a strong non-linearity. Regarding the research of an initial model of FWI, migration-based velocity analysis (MVA) (Yilmaz and Chambers, 1984; Symes and Carazzone, 1991; Symes, 2008) was used first, and then the method using traveltime tomography (Zelt and Barton, 1998; Operto et al., 2006; Woodward et al., 2008) was designed. Laplace-domain full waveform inversion by Shin and Cha (2009) is also widely used to build the long wavelength velocity model (Ha et al., 2012; Park et al, 2013).

MVA is largely divided into residual-curvature analysis (RCA) and depth focusing analysis (DFA). RCA (Al-Yahya, 1989; Liu and Bleistein, 1995) was started from the idea that transforms the residual moveout information of common-image gathers (CIGs) into velocity update. If the velocity macro-model is exact, common-shot or common-offset depth migrated profile provides same migrated images. Based on these ideas, we obtain macro-model by applying repeatedly pre-stack depth migration and velocity analysis. The velocity is updated in the direction to minimize the differential semblance function. The disadvantages of this method are a large computational cost and difficulty about meeting the numerical

requirement (Billette and Lambare, 1998; Prieux et al., 2012). DFA (Doherty and Claerbout, 1976; Yilmaz and Chambers, 1984; MacKay and Abma, 1992) is a way to make the focusing image in zero time and offset using the stacking power.

Traveltime tomography is a method to estimate the velocity model using the traveltime picked from prestack data and the horizon picked from migrated section. Tomographic velocity estimation can be also applied in the structure with dip reflector or strong lateral variation. However, the biggest drawback of this method is picking traveltimes. Picking is not only time-consuming procedure, but also it has a problem for the systematic error (Biondi, 1992). The systematic error consists of external error, instrumental error and personal error. Picking process is mainly influenced on the individual error among them. Traveltime tomography is divided into the refraction traveltime tomography, the reflection traveltime tomography and combination of both.

Refraction traveltime tomography is also called as first-arrival traveltime tomography because it uses the first-arrival picked from the observed seismic data. In order to use this method, usually seismic data with 4 times or more long-offset than the target depth is required (Prieux et al., 2012). Above all, the first-arrival picking is very difficult when the low velocity layer exists, because seismic wave has a property going along the high velocity layer.

Reflection traveltime tomography picks traveltime by selecting the

reflection events from the acquired seismic data. It is meticulous and hard work to pick continuous reflection events. It has high resolution when compared to refraction tomography, but it is hard to meet the kinematic accuracy. Also, velocity estimation and imaging problem are interrelated. While estimation of the Reflector is needed for tomography, determining reflector position depends on velocity model (Biondi, 1992).

Laplace-domain FWI is a method to construct the initial velocity model using the Laplace-transformed seismic data. Because the Laplace-domain inversion is sensitive to the noise recorded before the first-arrival, muting is very important (Shin and Cha, 2008; Ha et al., 2012). Laplace-domain inversion is the latest technique in the field of initial velocity modeling, and it shows good results with realistic synthetic data tests (Shin and Cha, 2008; Ha et al., 2010; Cha and Shin, 2010) and real data tests (Ha et al., 2012). However, a lot of research is still required because there are unresolved problems such as the amplitude decreasing rapidly along the offset (Shin and Ha, 2008; Park et al., 2013) or the appropriate damping constant (Shin, 2015).

Bae et al. (2012) compared the Laplace-domain FWI and refraction tomography. While refraction tomography deals with only first arrival, Laplace-domain inversion considers both the early and late signals. Therefore Laplace-domain inversion has good resolution about the deeper part because sensitivity on the late signal is higher than the refraction tomography. Although Laplace-domain FWI consumes more computing time, the implementation of the algorithm is relatively easy. Ray-based

algorithm is usually difficult than the wave equation and grid-based algorithm.

In this paper, an initial velocity model was constructed using a tomographic method with CDR (Controlled Directional Reception). CDR had been widely developed in the Soviet Union (Riabinkin et al, 1962) based on the study of the Rieber (1936) as a method for determining traveltime and ray parameter of the seismic wave. It has been developed to this day since the introduction in the West by the study of the Sword (1981). Sword (1987) introduced a method for estimating a velocity from the data converted by the local slant stack. Variables used in estimating velocity are ray parameter and traveltime auto-picked from common-shot gather (CSG) and common-receiver gather (CRG). Therefore, it does not require a pre-picking operation like traveltime tomography. Auto-picked information from the local slant stack is regarded as more reliable than reflection traveltime directly picked from the seismic data, because local slant stack is calculated with a lot of seismic traces. It also provides more detailed information about the moveout than the imaging operator in the MVA (Biondi, 1992).

Estimating the velocity with CDR also is one of the tomographic methods. So, Billette and Lambare (1998) named these tomographic approaches using the slope the "slope tomography method". Typical tomography method should seek to minimize the difference between the predicted and observed traveltime (Worthington, 1984). However, this method minimizes the horizontal distance between each endpoint after ray-

tracing using the ray parameter pair. Therefore, its goal is to obtain the interval velocity, not the depth of the reflecting boundary. Using this method, we can reduce the sensitivity of the velocity error on the ray parameter error than when you configure error function with the traveltime (sword, 1986).

Another advantage of the CDR tomographic method is that there is no need to make assumptions about the continuity or the shape of reflector. It works well for the seismic data obtained from the sloped, folded or faulted area as well as horizontal layer. Also, additional analysis on reflecting surface is not required because of auto-picking through the slope obtained from the local slant stack. Finally, we can save processing time or storage because picks of traveltime and ray parameter take up less space than the original data (sword, 1987).

On the other hand, CDR tomography has some problems such as the loss of robustness and sensibility on multiples and other coherent noise. There were several approaches to solve this problem. Biondi (1990) designed a fully automatic estimation by expanding the CDR tomographic method. Also, Billette and Lambare (1998) consider a method of applying source and receiver points and ray direction as variables of cost function. While the misfit function generally consists of the information on reflector with fixed information (position or ray parameter, etc.) on surface, Billette and Lambare (1998) set the shot and receiver position and ray parameter as variables and fix the reflected point. Although these efforts contribute to eliminate instability, it leads to another problem that the huge calculating

cost and time are consumed. Also, other problem still remained is that it is difficult to obtain clear boundary of the velocity model. Choi et al. (2014) contributed to increase the calculation speed and build velocity macro-model with clearer boundaries by proposing the strip-off CDR method.

In this paper, we have verified effectiveness of the strip-off CDR method with two realistic synthetic data sets and a real data set. We constructed the velocity macro-model using CDR velocity analysis. The results obtained by this method were applied to the FWI as the initial velocity model. The inverted models were compared to the results of Laplace domain inverted model that is the conventional methods for generating initial velocity model.

2. Theory

2.1. Modeling and imaging equations

The key theory of CDR method will be described in this section. As shown in Figure 2.1, there are shot, receiver and reflection point in the 2D surface. τ_s is traveltime from shot point to reflector and τ_r is travetime from reflector to receiver point. Then, total traveltime t is the sum of τ_s and τ_r.

$$\tau_s(x_s, x) + \tau_r(x, x_r) = t(x_s, x_r, x), \tag{1}$$

where x_s and x_r are the source and receiver position on the surface and x is the reflection point on the reflected layer. The following equation establishes according to Fermat's principle that wave moves along the shortest path.

$$[\nabla_x \tau_s(x_s, x) + \nabla_x \tau_r(x, x_r)] \cdot \frac{dx}{dx_i} = 0, \tag{2}$$

where x_i is a position parameter on the surface. Equation (1) and (2) are called the modeling equation because it represents the forward modeling process to obtain space-time curve from the given reflector.

If the several shot and receiver points are given, we can obtain the reflective point by modifying the modeling equation slightly. In order to use the rate of change of the traveltime, differential equation of the Equation (1) by x_i is needed. It is represented in the Equation (3).

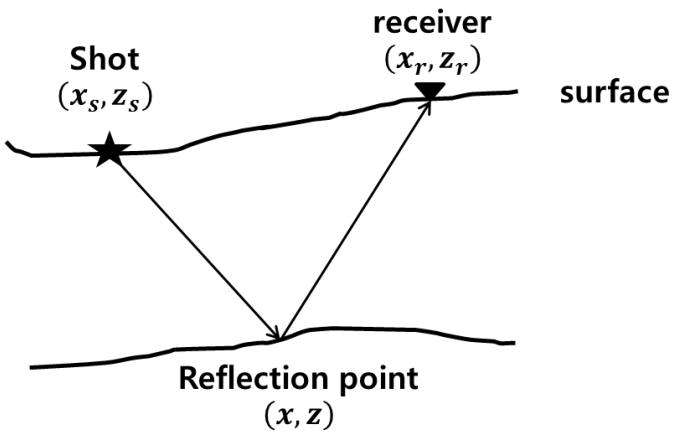

Figure 2.1. Shot, receiver and reflection points in the 2-D surface. The total traveltime is the sum of traveltime from shot point to reflector and travetime from reflector to receiver point.

$$\frac{d}{dx_i}[\tau_s(x_s, x) + \tau_r(x, x_r)] = \frac{d}{dx_i} t(x_s, x_r, x). \tag{3}$$

When unfolding the Equation (3),

$$\frac{\partial \tau_s}{\partial x_i} + \frac{\partial \tau_r}{\partial x_i} + [\nabla_x(\tau_s + \tau_r)] \cdot \frac{dx}{dx_i} = \frac{dt}{dx_i}. \tag{4}$$

We can remove the third term on the left side using Equation (2). Therefore, Equation (4) is simplified like the following:

$$\frac{\partial \tau_s}{\partial x_i} + \frac{\partial \tau_r}{\partial x_i} = \frac{dt}{dx_i}. \tag{5}$$

In contrast with the modeling equation, Equation (1) and (5) show migration imaging process that obtain reflector using the given space-time curve. Therefore, Liu (1995) called these two equations as 'imaging equation'.

Let's look again at Equation (5). In the case of CSG, x_i is equal to x_r.

$$\frac{\partial \tau_r}{\partial x_r} = \frac{dt}{dx_r}. \tag{6a}$$

As the same method, x_s is substituted for x_i in the CRG data.

$$\frac{\partial \tau_s}{\partial x_s} = \frac{dt}{dx_s}. \tag{6b}$$

This Equation (6) represents that we consider only the change of the time from reflective point to receiver in CSG data and from shot to reflective point in CRG data. If the velocity of the media is given, the direction of the

ray is determined. This is why the ray from shot to reflective point is just a ray parameter. In other word, we can obtain the reflective point from the travel-time and its spatial derivative value using the equation (1) and (6). It is the theoretical key of the velocity analysis with CDR or the prestack migration.

2.2. Ray parameter

A wave front is a line or surface connecting all points of same phase or equal travel time from the shot. Ripples on a pond are the example of wave fronts. Rays are the normal components to the wave fronts, and they indicate the direction of the wave propagation. While the mathematical description of the wave fronts is rather complex, that of the rays is simple. For many applications is it convenient to consider rays rather than wave fronts.

The ray parameter is the geometric property of a seismic ray that remains constant throughout its path. The mathematical sense of the ray parameter starts with Snell's law. Exact angles of incidence and refraction are given by:

$$\frac{\sin i}{v_i} = \frac{\sin r}{v_r} = p, \tag{7}$$

where i and r are angle of incidence and refraction, and v_i and v_r are velocity at each media. Here, p is defined as the ray parameter. Therefore the ray parameter is same for all rays originated from the same incoming ray.

Consider a plane wave that propagates as shown in Figure 2.2. We can express the angle of incidence (i) by using the small displacement of the r and x – each represents dr and dx.

$$\sin i = \frac{dr}{dx}. \tag{8}$$

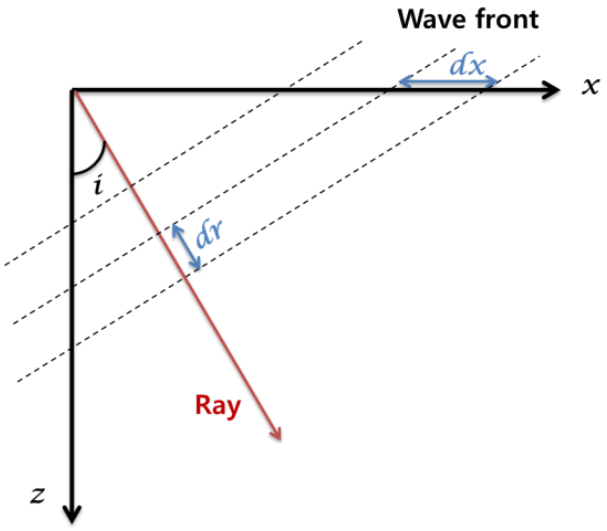

Figure 2.2. The ray in the propagation of plane wave. The ray parameter is the geometric property of a seismic ray and it is obtained by dividing propagation time (dt) into the displacement of x (dx). So, it may be thought as the horizontal slowness.

The displacement of r is equal to the product of propagation time and the reciprocal of the velocity. Using this relationship, Equation (7) and (8), we obtain the following Equation (9).

$$p = \frac{\sin i}{v} = \frac{dr}{v\,dx} = \frac{dt}{dx}. \tag{9}$$

Thus, the ray parameter may be thought as the horizontal slowness.

Determining the ray parameter from seismic data is difficult work. A traditional way of picking the ray parameter is to use a stacking chart with the principle of reciprocity about shot and receiver point. In this method, we do not have to consider the differences in the spacing between shots and receivers. However, a specific data acquisition like a split-spread recording scheme is needed for the establishment of reciprocity (Sword, 1984). Other method is performing slant stacks of traces of the seismic data. This method is widely use, so it is also selected on this method. It will be explained about this method from the following.

2.3. Local slant stack

Slant stack is one of the ways to obtain the ray parameter, and classified into global slant stack and local slant stack. Global slant stack is a method for moveout and stack about the whole trace of the seismogram. On the other hand, local slant stack obtains the ray parameter of the center trace using only a few traces around it. In this paper, the local slant stack was used. In order to apply this method, the seismic data should be divided to CSG and CRG. As seen from Equation (6), we consider only the rate of change of receiver point in CSG and shot point in CRG. Therefore, we can obtain ray parameter at receiver (p_r) from the result of local slant stack in CSG and ray parameter at shot (p_s) form that in CRG.

There are several issues to consider when performing local slant stack. The first is the number of traces to be used for local slant stack. We calculate the space differential value using n number of traces in the both side of the center trace. The n traces of seismogram edge are excluded from the calculation because the number of traces for the calculation is insufficient. The picked ray parameter values and calculation time depend on the number of traces. Information obtained using many traces assist in finding the exact ray parameter, but extra unnecessary information may interfere with the local trend. For solve this problem, it is sometimes used to weight at each trace with different value. The weighted value of the center trace is one, and it is close to zero if the distance is farther. In this paper, the following Hamming function is used:

$$H(x_i) = 0.5 + 0.5\cos(x_i),$$
$$x_i = \left(i - \frac{n+1}{2}\right)\frac{2\pi\Delta x}{n}, \tag{10}$$

where Δx is distance between traces. Another problem with the number of traces is the computation time and storage space. Therefore, appropriate number of traces should be determined by considering the both of accuracy and calculation time.

It is the time interval that should be considered in the second. After performing a linear moveout, it must set the time interval between local traces in order to stack the traces. A delayed time was adopted, which is applicable to slope with the negative sign (-slope) of the trace for shifting the both side traces of selected center trace. When not matching the time interval of the time-delayed trace and the time interval of the center trace, the traces are stacked after matching time interval by interpolating two points that is the most close to the time interval of center trace.

It should also be considered other issues that the each number of the shots and the receivers and its spacing interval is different. Generally, the receiver has more number and narrower interval than the shot. Many researchers tried to solve this problem by changing the location of the shot and the receiver using principle of reciprocity. However, this method cannot be applied to all the acquired data and is numerically very complex. So, the method to set interval of ray parameter (Δp) into each different value in CSG and CRG is also used for calculating the local slant stack (Choi et al., 2014). They perform the calculation of ray parameter more

densely by narrowing Δp in CRG data which is relatively sparse because of small number and wide interval of shot. In addition to this method, other method is also used in this paper. The shots and receivers were selectively used from the acquired seismic data, so we adjust the number of traces in CSG and CRG or fit the spacing interval similarly. This is not only able to relieve the imbalance of CSG and CRG data and also reduce computation time.

Finally, it is also important to determine the range of the ray parameter for calculating local slant stack. Threshold amount is preferably about equal to the inverse of the minimum velocity ($1/v_{min}$) of the media or put a little larger value. This prevents to pick the less value than the minimum velocity. Also, it can reduce the computation time because the unneeded values outside the range are excluded from the calculation.

2.4. Strip-off CDR velocity analysis

Briefly the CDR, it is a ‘slant stack over short bases’. Once you combine the CSG and CRG after local slant stack, the information such as ray parameters, traveltimes and shot and receiver points is stored. This information is used to build the velocity macro-model. The strip-off approach was opted for CDR velocity analysis (Choi et al., 2014).

It starts from the assumption that the subsurface structure is blocked and the velocity of each block is constant. First, we must specify the block by setting the continuous boundary in auto-picked events. CDR ray-tracing can be performed on given blocks using the traveltime and two ray parameters. Then, we decide the optimal velocity of the block, which the velocity minimize the distance between the destination point of the each ray started from the shot and receiver. In this case, the condition is applied that the sum of each traveltime to the reflection point is equal to the auto-picked total traveltime. This condition is usually fixed and only distance between two destination points is set as variable. This can be simple and quick calculation, but there is a limit to reducing the error. That is why it considers only the differences of the distance when the condition for time is fixed. Therefore, conditions for the time as well as the conditions for the distance should be determined as a variable and consider together.

Let's look at close conditions depending on the distance and time of the destination point. In the two-dimensional media, the location of shot

(x_s, z_s) and receiver (x_r, z_r) are given and the destination points (x_e, z_e) and total traveltime (t) are determined. Then, the destination point (x_{es}) of ray started from a shot is expressed as follows:

$$x_{es} = \frac{\sin\theta_s \cos\theta_r}{\cos\theta_s + \cos\theta_r}\left(vt - \frac{z_s - z_r}{\cos\theta_r}\right) + x_s \,. \tag{11a}$$

The destination point (x_{er}) of ray started from a receiver is also same.

$$x_{er} = \frac{\sin\theta_r \cos\theta_s}{\cos\theta_s + \cos\theta_r}\left(vt - \frac{z_r - z_s}{\cos\theta_r}\right) + x_r \,. \tag{11b}$$

where, θ_s and θ_r are angles of the each ray and v is the velocity of the media. If measured ray-parameters and traveltimes and estimated velocity are correct values, two horizontal end positions meet at the same point. We can use the differences in two positions as a distance criterion for the velocity estimation.

$$x_{criterion} = \frac{\cos\theta_s \cos\theta_r}{\sin(\theta_s - \theta_r)}\left(x_r - x_s + \frac{z_s \sin\theta_s}{\cos\theta_s} - \frac{z_r \sin\theta_r}{\cos\theta_r}\right). \tag{12}$$

In this paper, we used time criterion as well as distance criterion for organizing cost function of velocity estimation. The time criterion $t_{criterion}$ of two rays is calculated as follows.

$$t_{criterion} = t - \frac{z_{selected} - z_s}{v\cos\theta_s} + \frac{z_{selected} - z_r}{v\cos\theta_r}, \tag{13}$$

where, $z_{selected}$ is the depth that is selected when setting the layer

boundaries and t is auto-picked traveltime. We can also use the difference of calculated intersecting time and auto-picked traveltime t as a time criterion for the velocity estimation.

2.5. Damped least-square method

The smoothing process is necessary to apply the velocity model obtained from CDR method to the FWI. It is a method for solving minimization in non-linear inverse problems. Two essential methods are the Gauss-Newton algorithm and the damped least-square (DLS) method. The DLS is more reliable to derive solutions to non-linear inverse problems (Shirangi and Emerick, 2016). So, the DLS method is selected for smoothing process in this paper. This method was first mentioned by Levenberg (1944) and developed by Marquardt (1963). So, it is also called as the Levenberg-Marquardt algorithm.

The DLS is mainly used for solving the least squares curve fitting problems. When the dependent variables vector ($\mathbf{y}$) of empirical data and the model curve vector $\mathbf{M}$ with the independent variables are given, the sum of the squares of deviation is expressed by

$$\mathbf{S}(\alpha) = \|\mathbf{y} - \mathbf{M}(\alpha)\|^2 , \tag{14}$$

where α is the parameter of the model curve function. This equation is minimized through iterative calculation. In each iteration, α is updated to $\alpha + \delta$.

$$\begin{aligned} \mathbf{S}(\alpha + \delta) &= \|\mathbf{y} - \mathbf{M}(\alpha + \delta)\|^2 \\ &\approx \|\mathbf{y} - \mathbf{M}(\alpha) - \mathbf{J}\delta\|^2 , \end{aligned} \tag{15a}$$

where

$$\mathbf{M}(\alpha+\delta) \approx \mathbf{M}(\alpha) + \mathbf{J}\delta\,. \tag{15b}$$

The model curve function **M** can be approximated by linearization as Equation (15b). **J** is the Jacobian matrix of the model curve vector. Equation (15a) is differentiated with respect to α and arranged as

$$\left(\mathbf{J}^{\mathrm{T}}\mathbf{J}\right)\delta = \mathbf{J}^{\mathrm{T}}[\mathbf{y} - \mathbf{M}(\alpha)]\,. \tag{16}$$

Levenberg (1944) put a damping factor $\boldsymbol{\lambda}$ in Equation (16), so he suggested the following equation.

$$\left(\mathbf{J}^{\mathrm{T}}\mathbf{J} + \boldsymbol{\lambda}\mathbf{I}\right)\delta = \mathbf{J}^{\mathrm{T}}[\mathbf{y} - \mathbf{M}(\alpha)]\,, \tag{17}$$

where **I** is the identity matrix. The damping factor serves to adjust the amount of reduction about the sum of the squares of deviation (**S**). The small damping factor is required in a rapid reduction, whereas larger damping factor is used for a slow decrease.

However, there is a problem that cannot find the inverse of $\left(\mathrm{J}^{\mathrm{T}}\mathrm{J} + \lambda\mathrm{I}\right)$ when the damping factor is too large. To address this issue, Marquardt (1963) proposed the use of a diagonal matrix of $\mathrm{J}^{\mathrm{T}}\mathrm{J}$ instead of identity matrix (I).

$$\left(\mathbf{J}^{\mathrm{T}}\mathbf{J} + \boldsymbol{\lambda}\,\mathbf{diag}\left(\mathbf{J}^{\mathrm{T}}\mathbf{J}\right)\right)\delta = \mathbf{J}^{\mathrm{T}}[\mathbf{y} - \mathbf{M}(\alpha)]\,. \tag{18}$$

This method helps to avoid slow convergence in the direction of small gradient.

2.6. Objective function and source estimation in FWI

Full waveform inversion (FWI) is a method to build a subsurface velocity model by comparing the calculated value through modeling and observed value in seismic data. The difference between observed and modeled data is defined by using an objective function. Various objective functions such as l_2-norm, L_1-norm, Huber and logarithmic objective function have been used, and comparative study of the behavior of these objective functions were also conducted (Shin and Ha, 2008). According to this study, in the frequency domain, all the objective function used in this experiment showed a similar pattern. Therefore, in this paper, the logarithmic objective function as well as the l_2-norm objective function, which is mainly used in frequency domain, is performed on FWI and then we compared these two results. The method on source wavelet estimation also depends on the defined objective function.

2.6.1. L_2-norm objective function and source estimation

L_2-norm objective function at single frequency is expressed as follows (Pratt et al., 1998).

$$E = \sum_{i=1}^{n_s} \sum_{j=1}^{n_r} \frac{1}{2} \left[(u_{ij} - d_{ij}) (u_{ij} - d_{ij})^* \right], \tag{19}$$

where u is the modeled data, d is the observed data, n_s is the number of the sources, n_r is the number of the receivers and * denotes the complex conjugate. We can calculate the steepest-descent direction of the objective

function by partial-differentiating Equation (19) with respect to a model parameter m_k.

$$\frac{\partial E}{\partial m_k} = \sum_{i=1}^{n_s} \sum_{j=1}^{n_r} \mathrm{Re}\left[\frac{\partial u_{ij}}{\partial m_k}\left(u_{ij} - d_{ij}\right)^*\right]. \tag{20}$$

We called the first term ($\frac{\partial u_{ij}}{\partial m_k}$) as partial differential wavefeild, consider the wave equation for obtaining it.

In the frequency domain, the 2D acoustic wave equation for a homogeneous and isotropic media can be expressed as

$$\nabla^2 u(\mathbf{x}, \omega) - \frac{\omega^2}{c^2} u(\mathbf{x}, \omega) = f(\mathbf{x}, \omega)\,, \tag{21}$$

where c is the velocity of the media, ω is the angular frequency, $u(\mathbf{x}, \omega)$ is the wavefield and $f(\mathbf{x}, \omega)$ is the source function. By using finite difference method (FDM) or finite element method (FEM), Equation (19) can be written as

$$\mathbf{Su} = \mathbf{f}\,, \tag{22a}$$

with

$$\mathbf{S} = \mathbf{K} - \omega^2 \mathbf{M}\,, \tag{22b}$$

where **u** is the wavefield vector, **f** is the source vector, **S** is the impedance matrix, **K** is the stiffness matrix and **M** is the mass matrix. Equation (22a) also can be expressed by differentiating with respect to a model parameter m_k.

$$\frac{\partial \mathbf{u}}{\partial m_k} = \mathbf{S}^{-1}\mathbf{v}_k \,, \tag{23a}$$

with

$$\mathbf{v}_k = -\frac{\partial \mathbf{S}}{\partial m_k}\mathbf{u} \,, \tag{23b}$$

where $\mathbf{v}_k$ is the virtual source vector on the *k*th model parameter (Shin and Min, 2006). Substituting Equation (23a) into Equation (20) represents following equation.

$$\frac{\partial E}{\partial m_k} = \sum_{i=1}^{n_s}\sum_{j=1}^{n_r} \mathrm{Re}[(\mathbf{v}_k)^T(\mathbf{S}^{-1})^T\mathbf{r}] \,, \tag{24}$$

where $\mathbf{r} = \mathbf{u} - \mathbf{d}$ is the residual vector. We now can determine the direction that minimizes the objective function using a Gauss-Newton method. For this, normalization procedure using the Hessian matrix is necessary. The approximate Hessian matrix can be replaced with Psedo-Hessian matrix (Shin et al., 2001), because calculating the approximate Hessian matrix takes a lot of time and cost

When update velocity in the above method, we can obtain a more accurate velocity if the source wavelet is updated together. The wavefield of the frequency domain is expressed by the product of the Green's function and the source wavelet element. In order to develop an algorithm for estimating the source wavelet, each element should be divided into a real part and an imaginary part. When the source wavelet element is $a + ib$ and the Green's function is $c_j + id_j$, the wavefield is as follows.

$$u_j = (a+ib)(c_j+id_j) = (ac_j - bd_j) + i(ad_j + bc_j), \quad j = 1,2,\cdots,n_r. \tag{25}$$

If the observed data is written as $e_j + if_j$, the objective function using the residual can be expressed.

$$E_{src} = \sum_{j=1}^{n_r} \frac{1}{2}\left[(ac_j - bd_j - e_j)^2 + (ad_j + bc_j - f_j)^2\right]. \tag{26}$$

Using the full Newton method, we obtain $\delta\mathbf{p}_{src}$.

$$\begin{aligned}\delta\mathbf{p}_{src} &= -\mathbf{H}_{src}^{-1}\nabla E_{src} = -\begin{bmatrix}\frac{\partial^2 E_{src}}{\partial a^2} & \frac{\partial^2 E_{src}}{\partial a \partial b} \\ \frac{\partial^2 E_{src}}{\partial b \partial a} & \frac{\partial^2 E_{src}}{\partial b^2}\end{bmatrix}^{-1}\begin{bmatrix}\frac{\partial E_{src}}{\partial a} \\ \frac{\partial E_{src}}{\partial b}\end{bmatrix} \\ &= \begin{bmatrix}-a + \frac{\sum_{j=1}^{n_r}(c_j e_j + d_j f_j)}{\sum_{j=1}^{n_r}(c_j^2 + d_j^2)} \\ -b - \frac{\sum_{j=1}^{n_r}(d_j e_j - c_j f_j)}{\sum_{j=1}^{n_r}(c_j^2 + d_j^2)}\end{bmatrix}.\end{aligned} \tag{27}$$

Thus, the source wavelet of the next iteration with respect to the k-th source wavelet $p^k = a^k + ib^k$ can be updated as follows.

$$\begin{bmatrix}a^{k+1} \\ b^{k+1}\end{bmatrix} = \begin{bmatrix}\frac{\sum_{j=1}^{n_r}(c_j e_j + d_j f_j)}{\sum_{j=1}^{n_r}(c_j^2 + d_j^2)} \\ -\frac{\sum_{j=1}^{n_r}(d_j e_j - c_j f_j)}{\sum_{j=1}^{n_r}(c_j^2 + d_j^2)}\end{bmatrix}. \tag{28}$$

2.6.2. Logarithmic objective function and source estimation

In the same manner, let unfold the equation for the logarithmic objective function and the source wavelet estimation. The objective function and its steepest-descent direction are defined as follows (Shin and Min, 2006).

$$E = \sum_{i=1}^{n_s}\sum_{j=1}^{n_r}\frac{1}{2}\left(\ln\frac{u_{ij}}{d_{ij}}\right)\left(\ln\frac{u_{ij}}{d_{ij}}\right)^{*}, \tag{29a}$$

$$\frac{\partial E}{\partial m_k} = \sum_{i=1}^{n_s}\sum_{j=1}^{n_r}\mathrm{Re}\left[\frac{\partial u_{ij}}{\partial m_k}\frac{1}{u_{ij}}\left(\ln\frac{u_{ij}}{d_{ij}}\right)^{*}\right]. \tag{29b}$$

Equation (24) is derived by same process as the section 2.6.1. However, residual vector values are different.

$$r_{ij} = \frac{1}{u_{ij}}\left(\ln\frac{u_{ij}}{d_{ij}}\right). \tag{30}$$

The next following part is addressed about source wavelet estimation in the logarithmic objective function. When expressed the source wavelet elements as a product of amplitude and phase ($Ae^{i\varphi_{src}}$), the Fourier transformed wavefield is

$$u_j = \left(Ae^{i\varphi_{src}}\right)\left(B_j e^{i\varphi_{mod,j}}\right) = AB_j e^{i\left(\varphi_{src}+\varphi_{mod,j}\right)}, \quad j = 1,2,\cdots,n_r. \tag{31}$$

where B_j and $\varphi_{mod,j}$ are the amplitude and the phase of the modeled

wavefield. Similarly, the observed wavefield can be expressed as $C_j e^{i\varphi_{obs,j}}$. Then, the residual between modeled wavefild u and observed wavefield is expressed as

$$\begin{aligned}\delta r_j &= \ln\left(AB_j e^{i(\varphi_{src}+\varphi_{mod,j})}\right) - \ln\left(C_j e^{i\varphi_{obs,j}}\right) \\ &= \ln\left(\frac{AB_j}{C_j}\right) + i\left(\delta\varphi_j\right),\end{aligned} \tag{32}$$

where $\delta\varphi_j = \varphi_{src} + \varphi_{mod,j} - \varphi_{obs,j}$. We must update the amplitude and the phase of the source wavelet. The gradient with respect to φ_{src} and $z = \ln A$ are

$$\nabla_{\varphi_{src}} E_{src} = \sum_{j=1}^{n_r} \delta\varphi_j\,, \tag{33a}$$

$$\nabla_z E_{src} = \sum_{j=1}^{n_r} \left(z + \ln\frac{B_j}{C_j}\right). \tag{33b}$$

Using the full Newton method, $\delta\mathbf{p}_{src}$ is as follow.

$$\begin{aligned}\delta\mathbf{p}_{src} = -\mathbf{H}_{src}^{-1}\,\nabla E_{src} &= -\begin{bmatrix} \frac{\partial^2 E_{src}}{\partial\varphi_{src}{}^2} & \frac{\partial^2 E_{src}}{\partial\varphi_{src}\partial z} \\ \frac{\partial^2 E_{src}}{\partial z\partial\varphi_{src}} & \frac{\partial^2 E_{src}}{\partial z^2} \end{bmatrix}^{-1} \begin{bmatrix} \frac{\partial E_{src}}{\partial\varphi_{src}} \\ \frac{\partial E_{src}}{\partial z} \end{bmatrix} \\ &= -\begin{bmatrix} \sum_{j=1}^{n_r} 1 & 0 \\ 0 & \sum_{j=1}^{n_r} 1 \end{bmatrix}^{-1} \begin{bmatrix} \sum_{j=1}^{n_r} \delta\varphi_j \\ \sum_{j=1}^{n_r} \left(z + \ln\frac{B_j}{C_j}\right) \end{bmatrix}\end{aligned} \tag{34}$$

$$= \begin{bmatrix} -\dfrac{\sum_{j=1}^{n_r} \delta\varphi_j}{\sum_{j=1}^{n_r} 1} \\ -\dfrac{\sum_{j=1}^{n_r} \left(z + \ln\dfrac{B_j}{C_j}\right)}{\sum_{j=1}^{n_r} 1} \end{bmatrix}.$$

Therefore, (k + 1)-th source wavelet can be updated with respect to the k-th source wavelet.

$$\begin{aligned} \begin{bmatrix} \varphi_{src}^{k+1} \\ z^{k+1} \end{bmatrix} &= \begin{bmatrix} \varphi_{src}^{k} - \dfrac{\sum_{j=1}^{n_r} \delta\varphi_j}{\sum_{j=1}^{n_r} 1} \\ z^{k} - \dfrac{\sum_{j=1}^{n_r} \left(z + \ln\dfrac{B_j}{C_j}\right)}{\sum_{j=1}^{n_r} 1} \end{bmatrix} \\ &= \begin{bmatrix} \varphi_{src}^{k} - \dfrac{\sum_{j=1}^{n_r} \varphi_{src}^{k} + \varphi_{mod,j} - \varphi_{obs,j}}{\sum_{j=1}^{n_r} 1} \\ -\dfrac{\sum_{j=1}^{n_r} \ln\dfrac{B_j}{C_j}}{\sum_{j=1}^{n_r} 1} \end{bmatrix}. \end{aligned} \tag{35}$$

We simply compared the two objective functions and showed in the table 2.1.

	L_2-norm	logarithmic
Objective function	$\sum_{i=1}^{n_s}\sum_{j=1}^{n_r}\frac{1}{2}\left[(u_{ij}-d_{ij})(u_{ij}-d_{ij})^*\right]$	$\sum_{i=1}^{n_s}\sum_{j=1}^{n_r}\frac{1}{2}\left(\ln\frac{u_{ij}}{d_{ij}}\right)\left(\ln\frac{u_{ij}}{d_{ij}}\right)^*$
Residual	$ac_j - bd_j - e_j + i(ad_j + bc_j - f_j)$	$\ln\left(\frac{AB_j}{C_j}\right) + i(\delta\varphi_j)$
Source wavelet estimation	$\begin{bmatrix} a^{k+1} \\ b^{k+1} \end{bmatrix} = \begin{bmatrix} \frac{\sum_{j=1}^{n_r}(c_j e_j + d_j f_j)}{\sum_{j=1}^{n_r}(c_j^2 + d_j^2)} \\ -\frac{\sum_{j=1}^{n_r}(d_j e_j - c_j f_j)}{\sum_{j=1}^{n_r}(c_j^2 + d_j^2)} \end{bmatrix}$	$\begin{bmatrix} \varphi_{src}^{k+1} \\ z^{k+1} \end{bmatrix} = \begin{bmatrix} \varphi_{src}^{k} - \frac{\sum_{j=1}^{n_r}\varphi_{src}^{k} + \varphi_{mod,j} - \varphi_{obs,j}}{\sum_{j=1}^{n_r}1} \\ -\frac{\sum_{j=1}^{n_r}\ln\frac{B_j}{C_j}}{\sum_{j=1}^{n_r}1} \end{bmatrix}$

Table 2.1. The Comparison of the l_2-norm and logarithmic objective function.

2.7. Constructing initial model using the Laplace-domain FWI

The Laplace-domain FWI was selected for comparison with the macro velocity model of the strip-off CDR method. It is the latest technology and has been widely used in the field of initial velocity modeling. This method uses the Laplace transformed wave equation as follows:

$$\nabla^2 \tilde{u}(\mathbf{x}, s) - \frac{s^2}{c^2} \tilde{u}(\mathbf{x}, s) = \tilde{f}(\mathbf{x}, s) , \tag{36}$$

where c is the velocity, s is a Laplace damping constant, $\tilde{u}(\mathbf{x}, s)$ is the Laplace transformed wavefield and $\tilde{f}(\mathbf{x}, s)$ is the Laplace transformed source function. Equation (36) is expressed in matrix form as Equation (22).

$$\mathbf{S}\tilde{\mathbf{u}} = \tilde{\mathbf{f}} , \tag{37a}$$

with

$$\mathbf{S} = \mathbf{K} + s^2\mathbf{M} , \tag{37b}$$

where $\tilde{\mathbf{u}}$ is the wavefield vector and $\tilde{\mathbf{f}}$ is the source vector in the Laplace domain.

The logarithmic objective function is generally used for defining the residual of the modeled and observed data in the Laplace-domain FWI. The Theories of the logarithmic objective function and its source estimation are described in section 2.6.2. In order to minimize the objective function, the model parameter, $\mathbf{m}_l$, is updated by the preconditioned gradient method (Pratt et al., 1998).

$$\mathbf{m}_l^{n+1} = \mathbf{m}_l^n + \delta\mathbf{m}\,, \tag{38a}$$

with

$$\delta\mathbf{m} = -\mathbf{H}^{-1}\nabla_m E\,, \tag{38a}$$

where $\mathbf{H}$ is a Hessian matrix. We use the diagonal elements of the pseudo-Hessian matrix suggested by Shin et al. (2001) because the full Hessian matrix requires large computational cost.

The velocity of substructure is updated using the above formulas and the process is as follows. The steepest descent direction is divided by the pseudo-Hessian. Then we can normalize it using the maximum absolute value. This process is repeatedly performed for each Laplace damping constant. All calculated values on each Laplace damping constant are summed and normalized. In this way, the velocity is updated by using the gradient direction. By repeating this algorithm until the objective function has minimum, we can finally construct a long-wavelength velocity model. This Laplace inverted model is often used as an initial model for the frequency-domain FWI.

3. Strip-off CDR processing

3.1 Seismic data sorting into CSG and CRG

For the strip-off CDR processing, seismic data set has to be sorted into common-shot gather (CSG) and common-receiver gather (CRG). This step is for local slant stack of the next step and there are two things to consider for this purpose. The first is the balance of the information obtained from the CSG and the CRG, as mentioned above in section 2.3. Because most of the seismic data has small number and wide spatial interval of shots, it may cause problems of imbalance in the local slant stack. There are several ways to solve this problem. Among them, this stage uses the shot and receiver selectively. We can make the similar number of receivers per a shot in CSG and shots per a receiver in CRG, by limiting the number of receivers that have relatively large number than shots. Also, we can make the receiver interval to be equal with the shot interval by selecting the receivers at regular interval. The method for selecting the shots and receivers depend on the geometry of the acquired data or the range of target.

Let's look at the Overthrust model used in this paper as an example (Figure 3.1). This is synthetic model that made based on real subsurface structure. A seismic data was obtained from this velocity model by assuming similar to the real environment. Once we confirm the number, location and interval of the shot and receiver from the data header. The shot interval is 50 m and the receiver interval is 25 m, so we keep these

intervals intact because of relatively small difference. The number of shots is 312 and total number of traces is 95,856. The graph of the number of receivers per a shot is shown in Figure 3.2(a). The number of receivers is equal to the number of traces obtained from the receiver. Here we chose the part of the traces, which have constant number at 331. Then the CSGs consist of 210 seismograms, since the number of shot is 210 from 4800 to 15250 m with 50 m interval.

The number of the shots per a receiver also is shown in the graph (Figure 3.2(b)) for composing the CRG. The seismograms with more than 60 traces were used except the both ends of CRG that have too small number of traces. Then we get 523 seismograms in CRG from to 3500 to 16550 m with 25 m interval and the maximum number of traces is 168. Since CRGs have fewer traces and the wider interval than CSGs, we sought to align the balance of the information obtained from the local slant stack using CRGs more than twice that number of CSGs. In addition, we limited the area used for the calculation by controlling the horizontal range of the shots and receivers similarly. In Figure 3.1, the red solid-line box is the range of shots used in CSG and the blue dotted-line box is the range of receivers used in CRG. This can reduce the data in the regions with little information and increase the calculation speed.

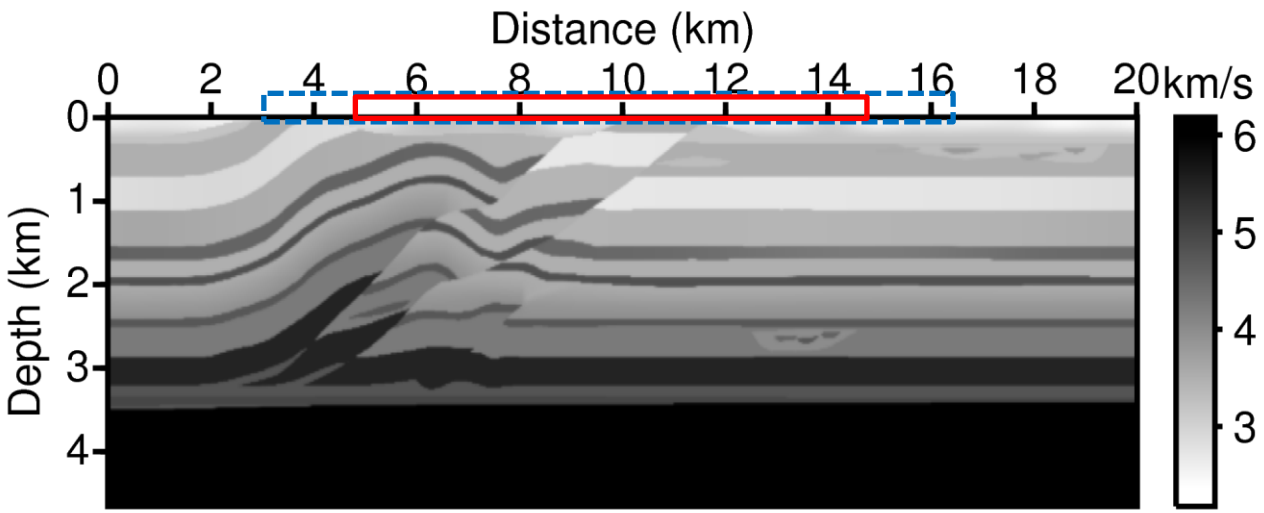

Figure 3.1. The true velocity model of the Overthrust synthetic seismic data. This synthetic model is made based on real subsurface structure and its seismic data is obtained by assuming similar to the real environment. The red solid-line box is the range of shots used in CSG and the blue dotted-line box is the range of receivers used in CRG

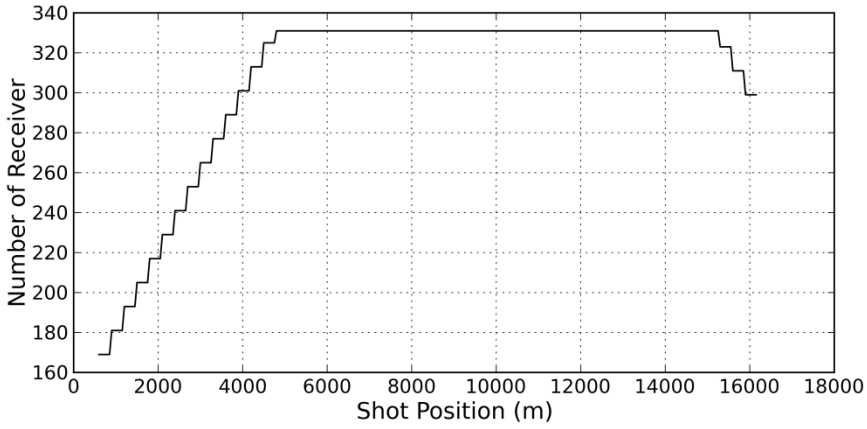

(a)

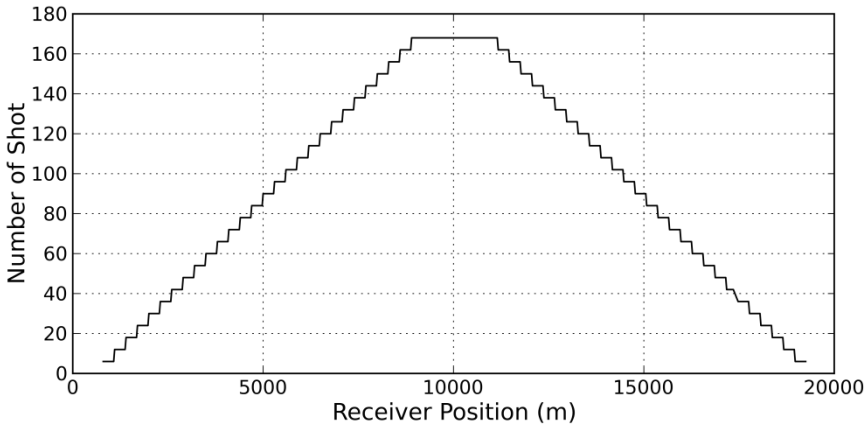

(b)

Figure 3.2. (a) The number of receivers as the shot position and (b) the number of shots as the receiver position. The part of the traces which have constant number at 331 is selected in Fig.3.2(a), so the CSGs consist of 210 seismograms. The CRGs have 523 seismograms with more than 60 traces in Fig.3.2(b).

The other one to consider for the local slant stack is shot or receiver interval. Local slant stack cannot be calculated if the trace interval is not constant, because the both sides are calculated by based on the center trace at regular interval. In general, this work is needed when dealing with real data. Most synthetic data has regular interval but most real data cannot have it because of irregular geometry. It is important to check carefully whether there is bad trace or no recorded trace when performing the real data test. If shot or receiver interval doesn't fit, we match the interval through an interpolation technique in case of 2D or a binning technique in case of 3D.

After this preparation, the sorting the exploration data based on the location of shots and receivers can give the CSG and the CRG. Using the above Overthrust model example, we divided seismic data into CSG and the CRG. CSG and CRG were compared in almost same range for verification as shown in Figure 3.3. We can see that the CSG (Figure 3.4(a)) and the CRG (Figure 3.4(b)) represent very similar shape. The resolution of CRG is slightly lower because of the less number of traces and a little poor continuity of data than CSG.

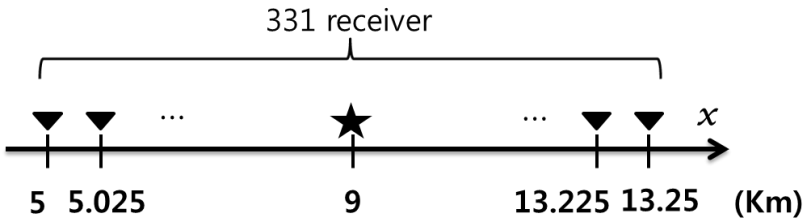

(a)

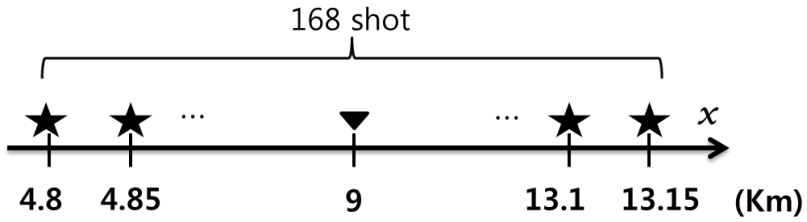

(b)

Figure 3.3. The position of shots and receivers of (a) common-shot gather in Figure 3.4(a) and (b) common-receiver gather in Figure 3.4(b). The CSG of 9 km has 331 receivers with 25 m interval and the CRG of 9 km has 168 shots with 50 m interval.

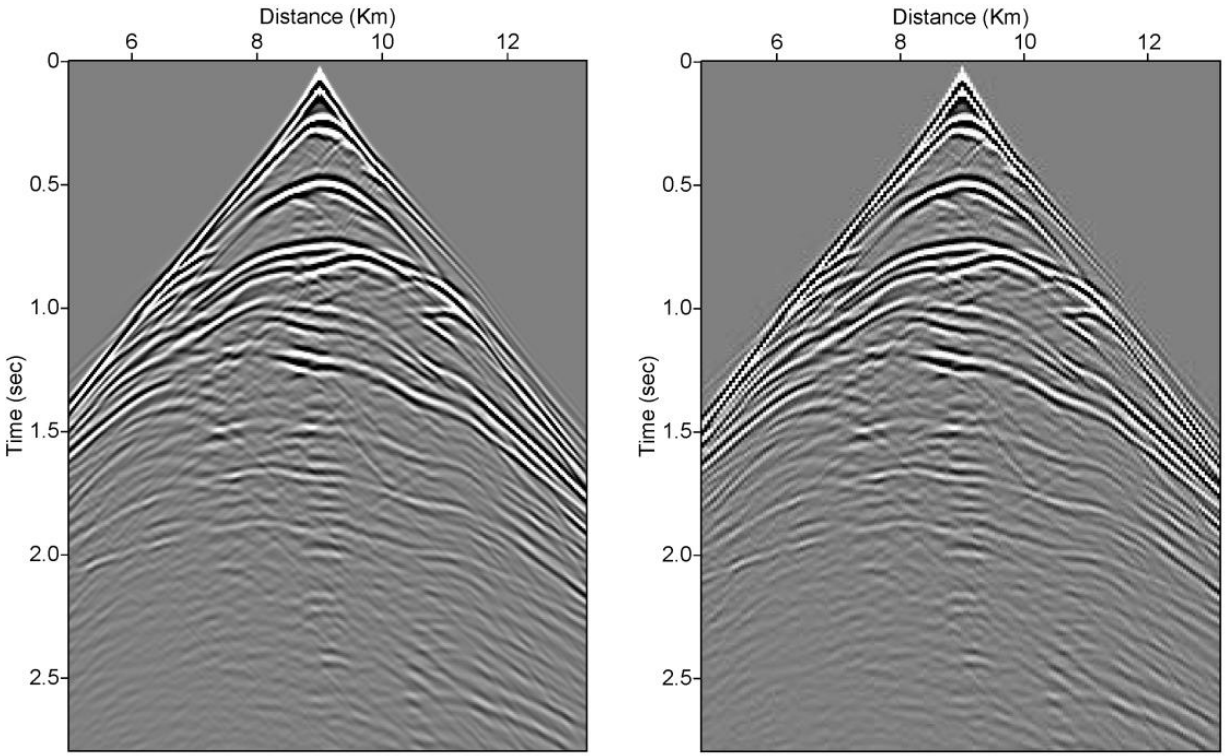

(a) (b)

Figure 3.4. (a) CSG at 9 km shot and (b) CRG at 9 km receiver. The CSG and the CRG represent very similar shape.

3.2 Local slant stack and picking ray parameter

In the aligned two data into CSG and CRG, local slant stack are carried out. We use total 7 traces with each 3 traces at both side of the reference trace. The range of the ray parameter is decided by the inverse of the minimum velocity. Through Figure 3.1, we can see that the minimum velocity of the Overthrust model is 2360 m/s. Therefore, the inverse of the velocity is $1/2360 \approx 4.24 \times 10^{-4}$ and we set a little larger value than it into the range of ray parameter for the calculation (p_{cal}).

$$-5 \times 10^{-4} \leq \mathrm{p_{cal}} \leq 5 \times 10^{-4}$$

Like this, in the synthetic velocity model we can visually know the minimum velocity, but we cannot use this method when using real data. Therefore, when there is a water layer, we use the p wave velocity in water, 1500 m/s. In case of no water layer, we use a maximum value of the slope of the seismogram.

The interval of ray parameter is also an important factor to be determined for local slant stack. CSG calculated 26 ray parameter with 4×10^{-5} interval and CRG does 51 ray parameter with 2×10^{-5} interval. We make the CRG be calculated more densely by reducing the interval of ray parameter by half because the trace interval of CRG wide twice than the CSG.

After performing local slant stack, ray parameters over time are saved for each trace, then the capturing the meaning signal of these values is the next action. The ray parameter with largest amplitude is selected for each trace, and then the events are auto-picked by setting a threshold on the basis of the

value. However, one $t-p$ panel per each trace requires a lot of storage space and the ray parameter should be read again for picking the events. Therefore, in this paper, local slant stack and event picking operation are proceeded simultaneously in order to save time and storage space.

To confirm the picking events, we show the figures with the seismogram of Figure 3.4 (Figure 3.5). The result of CSG seems relatively well-picking along events especially in the shallow part, even though it failed to catch weak signals in the deep part. In the case of CRG, the trend of picked events is similar as CSG but the connectivity is insufficient. However, the combining process will compensate for this low quality of CRG because CRG has seismograms more than twice than CSG.

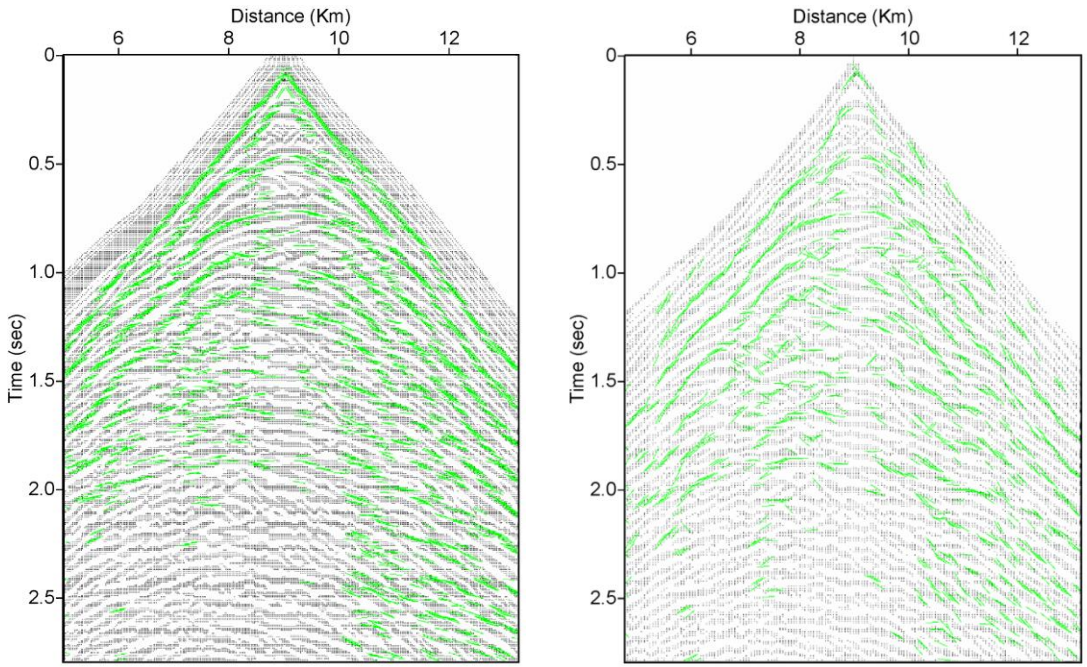

(a) (b)

Figure 3.5. The picked events with seismogram of (a) Figure 3.4(a) and (b) Figure 3.4(b). The result of CSG seems relatively well-picking along events especially in the shallow part, even though it failed to catch weak signals in the deep part. In the case of CRG, the trend of picked events is similar as CSG but the connectivity is insufficient.

3.3 Combining CSG and CRG event

Now, if the ray parameters obtained from the CSG (p_g) and the CRG (p_s) are same event, the two ray parameters are combined into one event. We first look for traces with same shot and receiver positions in CSG and CRG, and then we merge the events that exist at the same time. Theoretically, two ray-paths of same event should be present at exactly the same time on each trace. However, we set a tolerance range allowing for an error. In this example, we defined $0.16 \times 1/20 = 0.008\,s$ as time tolerance by allowing a 5% error of the source wavelength.

Figure 3.6 represents the combined event of CSG and CRG data. Compared to Figure 3.1, it appears well on the horizontal layers of the right side and the folding structure of the left side. In particular, it also appears the fault of the structure that is displayed in red dashed circles. However, it is hard to separate the layers in the deep part. Especially, the complex structure of the lower-left corner does not appear well. It is generally known that imaging deep part is a high-quality technique rather than shallow part in seismic data processing. Furthermore, our example seismic data processing is more difficult because of the short recording time.

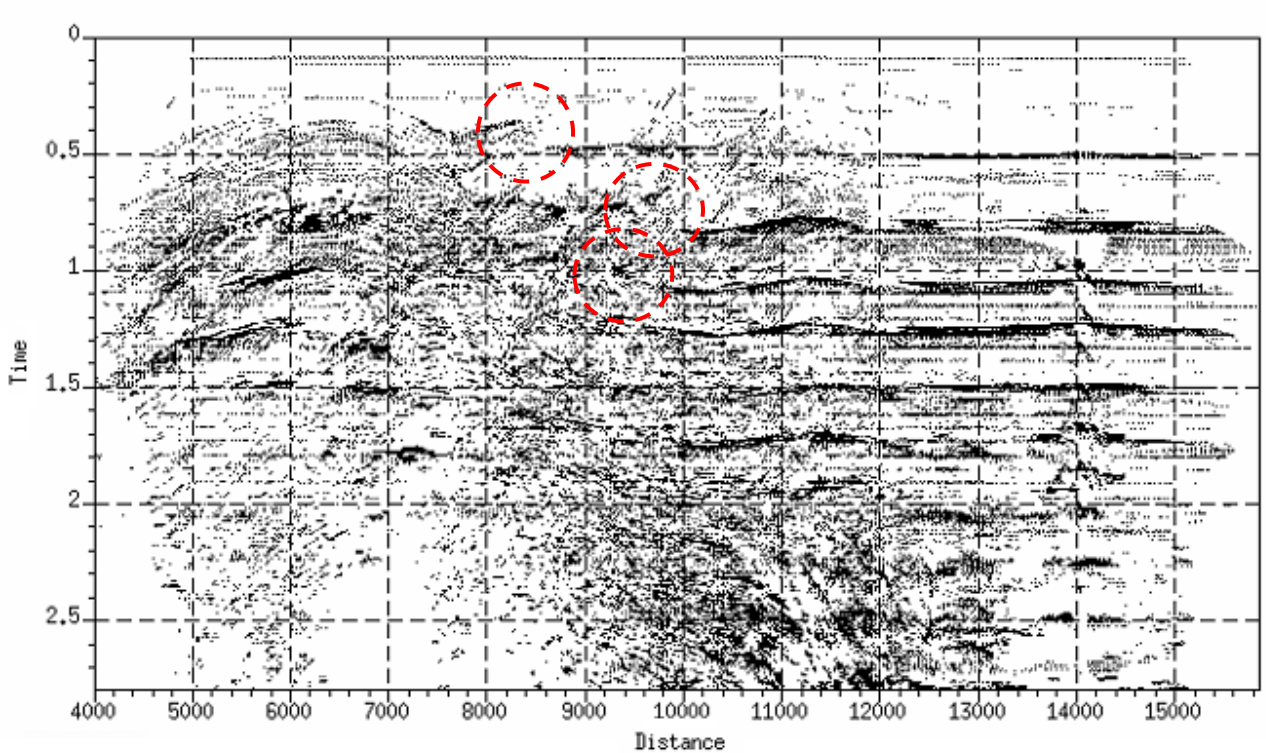

Figure 3.6. The combined events of CSGs and CRGs data. It appears well on the horizontal layers of the right side and the folding structure of the left side. The red dashed circles indicate the faults of the structure.

3.4 Constructing velocity macro-model for FWI

We made the velocity macro-model with the reflected event data obtained in the previous section. When determining the boundary with reflection point, we used migrated image together (Figure 3.7). By using with the reflection point and the migrated image, the accuracy of the boundary surface can be enhanced. At starting stage, the first migrated image obtained from the constant velocity model. If the migrated image is more accurate, the resolution of velocity model can be improved. Therefore, the kirchhoff migration was sometimes performed using updated velocity model of an intermediate step.

Figure 3.8(a) show the selected boundaries in the middle of processing. After determining the boundary of the layer, we selected representative velocity of the layer. We can calculate the velocity of each reflection point with given traveltime because the distance is given when setting the boundary. The representative velocity of the layer is selected to the most one among velocity of the reflection points used to set boundary. As mentioned earlier, conditions with time as well as with distance are also considered in this process. Figure 3.8(b) is the velocity model of the intermediate course.

Finally, it is needed to scale and smooth the finished velocity macro-model for the full waveform inversion. Depending on available range of inversion, we cut the velocity model from first shot to last shot or from first receiver to last receiver. Also, we determine the size of the padding by considering the boundary condition. In this example, the horizontal surface

range for inversion is from first shot to last shot, so we cut the velocity model from 4.8 to 15.25 km. The left and right padding for absorbing boundary condition is placed by 1.5 km. Therefore, the horizontal size of velocity model is 13.45 km. Smoothing velocity model was also performed because the FWI is a grid-based processing. A damped least squares technique was used with the damping parameter 5. The final velocity macro-model for FWI is shown in Figure 3.9.

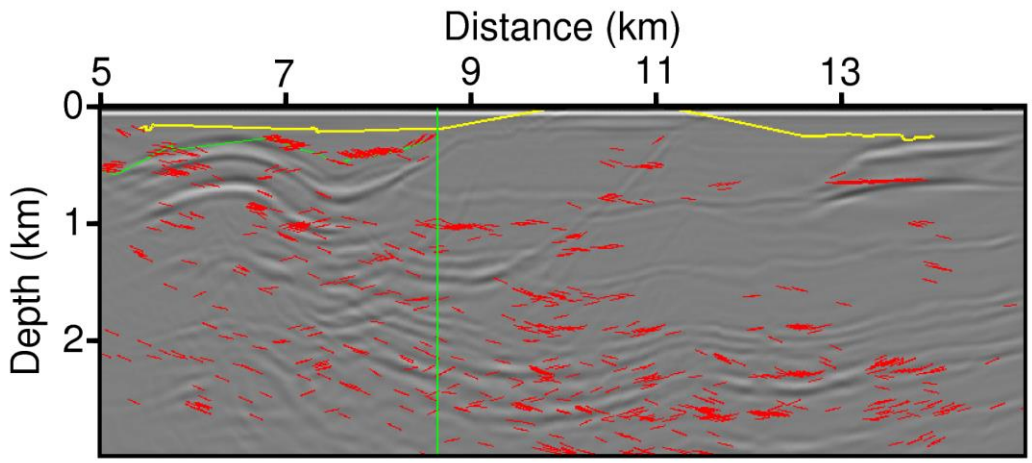

Figure 3.7. The process of the determining boundary by reflection point. The yellow line indicates selected layer boundary in the previous step and the red points are reflectors within determined velocity range. The migrated image is used as background. By using the reflection point and the migrated image together, the accuracy of the selecting boundary can be enhanced.

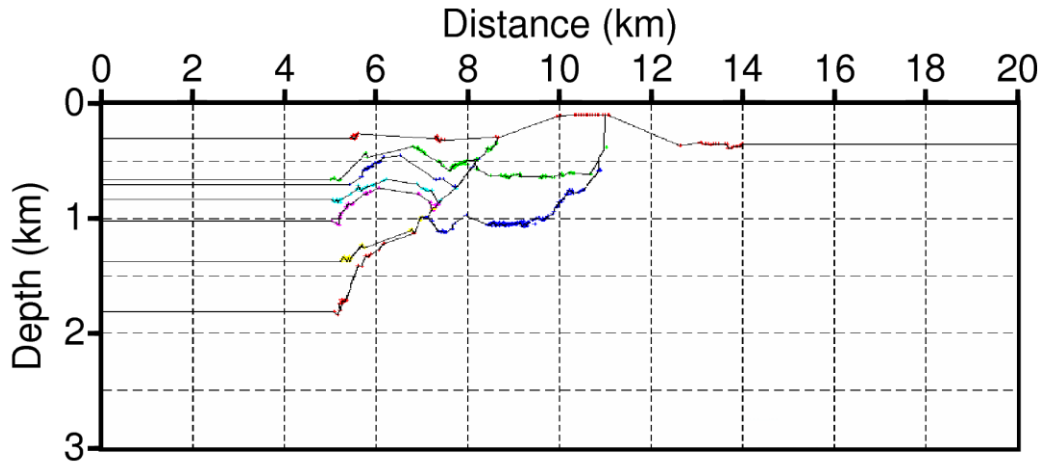

(a)

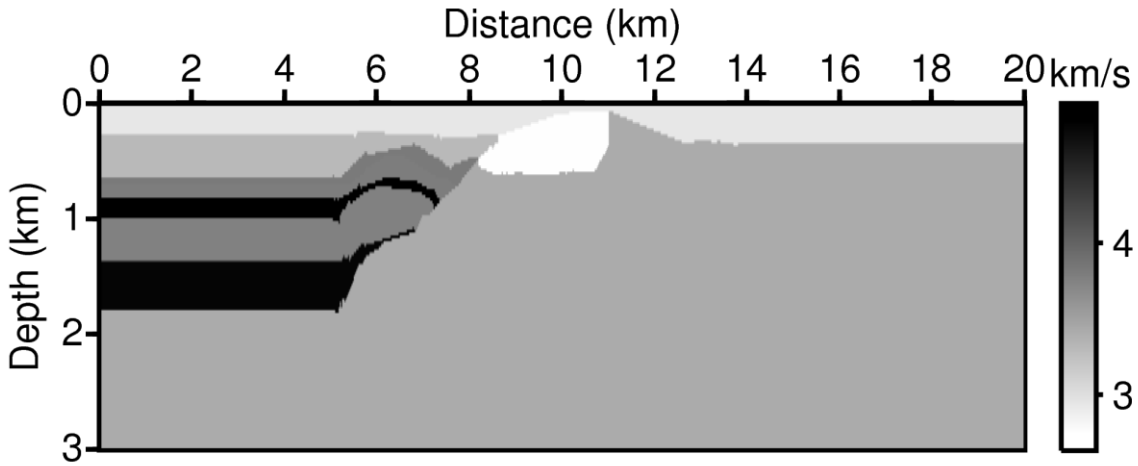

(b)

Figure 3.8. (a) The selected boundaries in the 10th processing and (b) its velocity model. After determining the boundary of the layer, we selected representative velocity of the layer.

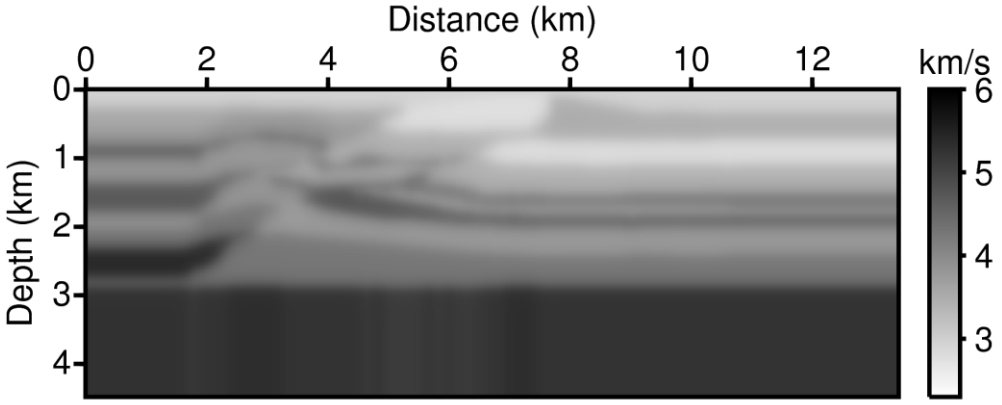

Figure 3.9. The final velocity macro-model of the Overthrust model for FWI. It was scaled and smoothed the finished velocity macro-model for the full waveform inversion. For smoothing, a damped least squares technique was used with the damping parameter 5.

4. FWI on synthetic data

4.1 Overthrust synthetic model

Overthrust model is a velocity model that is based on real subsurface structure as described in Section 3 (Figure 3.1). It has no water layer and complex velocity structures. There is an open seismic data obtained from this velocity model. It is hard to draw a good result from the open data by conventional inversion method, because it is made similar to the real seismic data. Particularly, it is very difficult to build deep velocity structure because of very short recording time. The maximum recording length is only 2.8 s and the time sampling interval is 8 ms. Shot and receiver information is same as mentioned in section 3.1.

There are three models to be used as the initial velocity conditions. The first one is the velocity model of Figure 3.9 by the strip-off CDR method in section 3. The other two models are shown in Figure 4.1. Figure 4.1(a) is obtained from Laplace-domain full-waveform inversion. The velocity of the starting model is increased linearly from 2.3 to 6.0 km/s and the step length for inversion is 0.025. The Laplace damping constants are used from 2 to 12 with an interval of 2, and a logarithmic objective function is applied. After the 42^{th} iteration, the inverted model is selected. Figure 4.1(b) is a linearly increasing model from 2.3 to 6.0 km/s and it is considered as a control group.

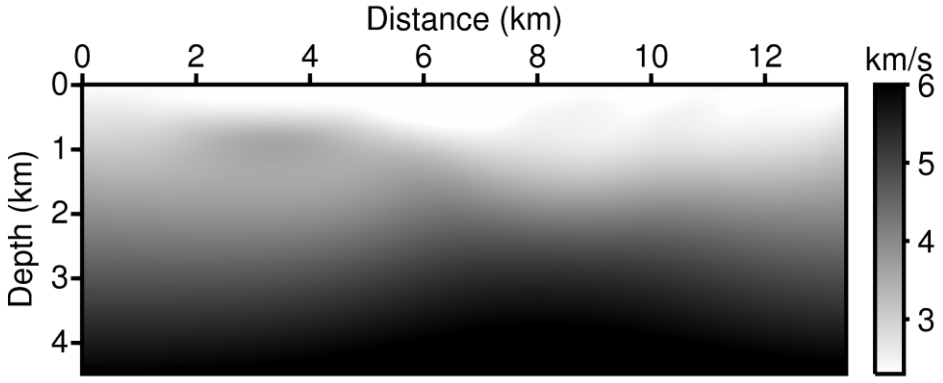

(a)

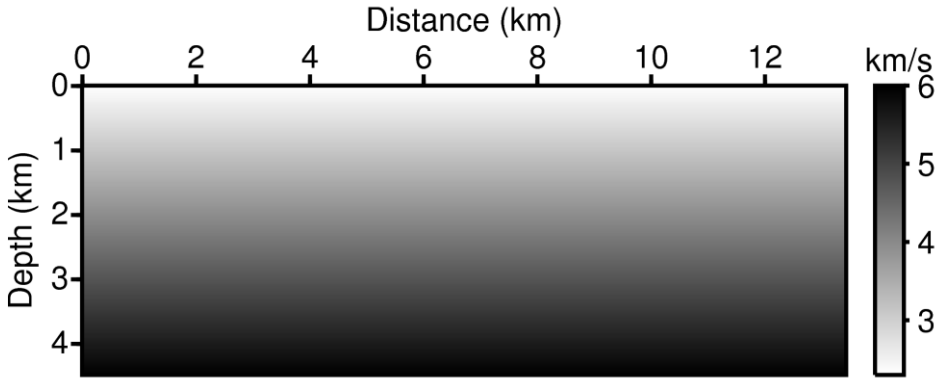

(b)

Figure 4.1. Initial models with (a) Laplace-domain inversion and (b) linearly increased method. Laplace damping constants are used from 2 to 12 with an interval of 2, and a logarithmic objective function is applied. It is 42th inverted model. The velocity of linearly increasing model is consists from 2.3 to 6.0 km/s.

The depth profiles were extracted to compare the change of velocity with depth in the initial models. True velocity model is shown in Figure 4.2 by reestablishing ranges as the position used in inversion scheme. We select three points for depth profile – 4 km point with a complex structure, 7 km point with high velocity layer in the early part and 10 km point with horizontal layers. The resulting graph is shown in Figure 4.3. The initial model from Laplace inversion is estimated incorrectly as low velocity in the early profile. Even though it follows major trend, the detailed velocity change is not found. The CDR macro-model shows relatively close value to the true model. It was hard to detect the velocity change in complex velocity structures (Figure 4.3(a)), but it found very good initial velocities in the horizontal layer (Figure 4.3(c)). This is a satisfactory result although it remains to solve problems that it didn't find the earlier high-velocity layer at 7 km point and the deeper velocity structure.

As mentioned as section 2.5, we applied the l_2-norm and logarithmic objective function because two objective functions have similar paten in the frequency domain inversion. The model size is 13.45 km x 3 km and the grid interval is 25m, so it has 538 x 120 elements. The shot for inversion is used 210 with 50 m interval. Thirty frequencies are selected from 3.0 to 13.44 with 0.36 intervals for inversion. Also, we performed same iteration number (250^{th}) of inversion on all models. To sum up, two groups have same conditions for inversion except for the objective function and three initial models are used in each group.

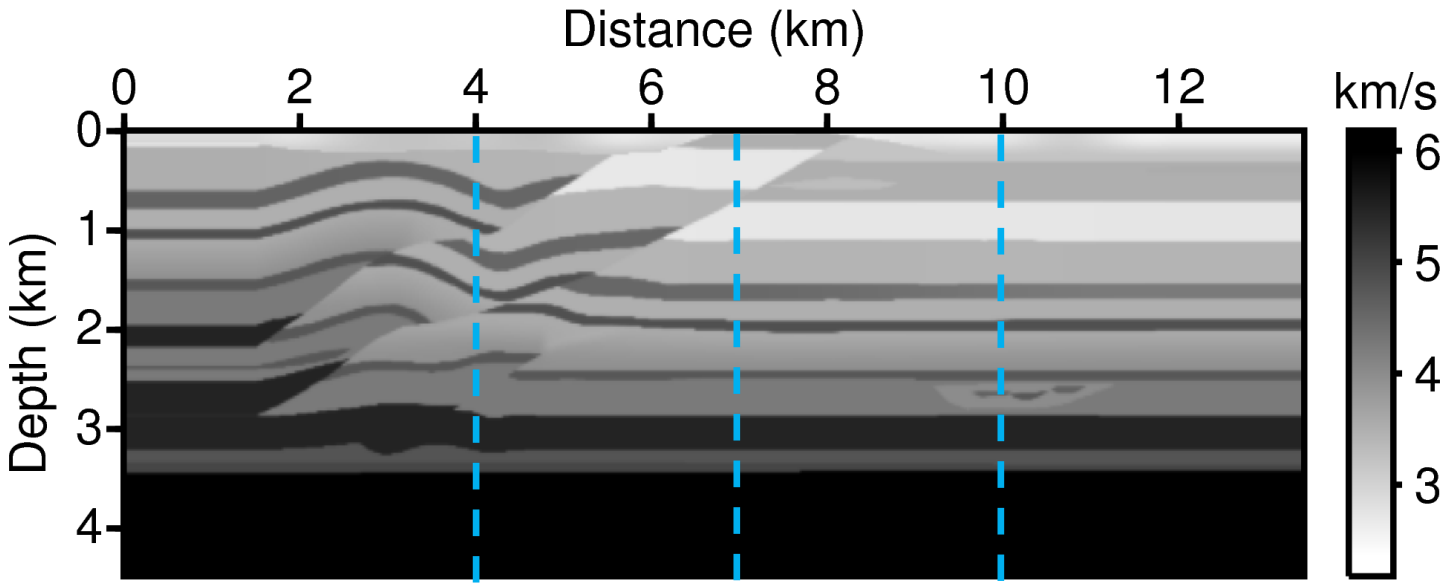

Figure 4.2. True Overthrust velocity model by reestablishing ranges as the position used in inversion scheme. The dotted lines indicate the depth profile line. 4 km point has complex velocity structure, 7 km point has high velocity layer in the early part and 10 km point with horizontal layers.

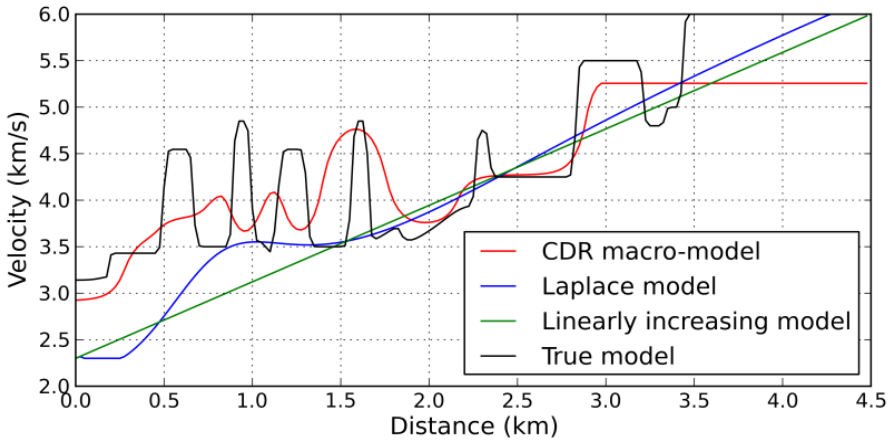
Velocity (km/s)
Distance (km)
CDR macro-model
Laplace model
Linearly increasing model
True model

(a)

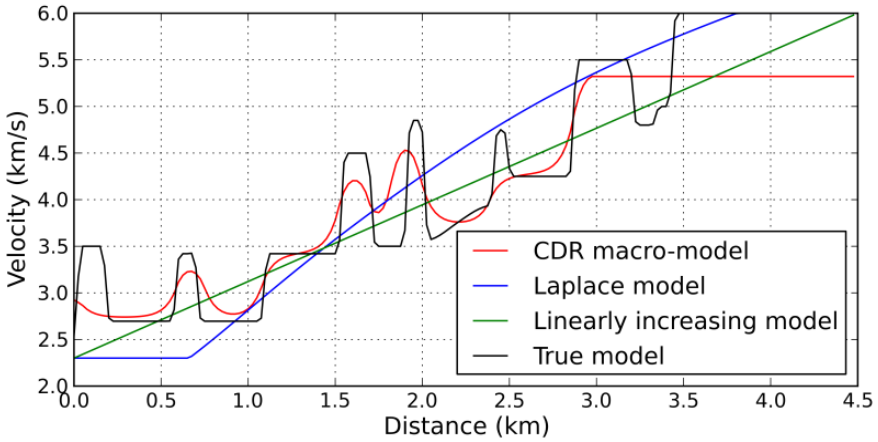
Velocity (km/s)
Distance (km)
CDR macro-model
Laplace model
Linearly increasing model
True model

(b)

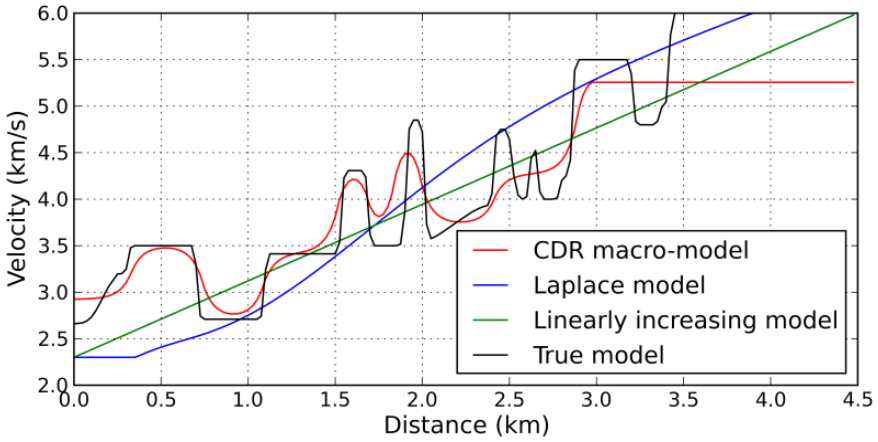

(c)

Figure 4.3. Depth profiles of initial models at (a) 4 km, (b) 7 km and (c) 10 km point. The CDR macro-model shows relatively close value to the true model.

The inversion results by using l_2-norm and logarithmic objective function are each represented in Figure 4.4 and 4.5. These are the results of 250th iteration. Figure 4.6 show the RMS error curve of amplitude and phase in the l_2-norm objective function. Root mean square (RMS) error is commonly used when dealing with the differences in the observed values in the real environment and the estimated or predicted value in the model. It is suitable to represent the precision. As defined above, each difference values are called residual. The root mean square deviation is used to integrate the residuals into a single measure. In Figure 4.6, the RMS errors of three models show a tendency to converge to a constant value. It has been alleged that the l_2-norm objective function falls in a local minima in many parts. So, Figure 4.4 shows the inverted result that is scarcely updated when compared to the initial models.

In the results of the logarithmic objective function, we can see the result of the CDR macro-model (Figure 4.5(a)) is better than that of the Laplace inverted model (Figure 4.5(b)). The inverted result with the Laplace model is estimated as lower velocity in the shallow part. However, the inverted model of the CDR macro-model found a distinct velocity structure in the shallower part although the velocity structure of the deep part doesn't appear well. It shows very similar structure to the true velocity model. Comparing the result of the Laplace model and a linearly increasing model (Figure 4.5(b)), the layer boundaries of the inverted model of the Laplace model show more clearly. In other words, the linearly increasing model couldn't find well the boundaries of the structure as well as the velocity of layer. Figure 4.7 is the RMS error as a function of iteration number. The RMS errors of the amplitude and the

phase are also shown the smallest value in the CDR model. The errors of other two models are very similar, but the Laplace model has a little smaller error. The Laplace model started with the largest error but it becomes smaller than the linearly increasing model.

Each three models show better results in the logarithmic than l_2-norm objective function. So, in order to check the results of the logarithmic objective function in more detail we drew the depth profile at 4 km, 7 km and 10 km distance (Figure 4.8). The velocity of CDR model follows very similar trend with true velocity than of Laplace inverted model especially in Figure 4.8(b) and (c). In the velocity oscillation part between 0.9 and 1.7 km of Figure 4.8(a), it doesn't show the well-inverted result. However, when considering that this seismic data is difficult to perform on the conventional inversion, this can be said remarkable result.

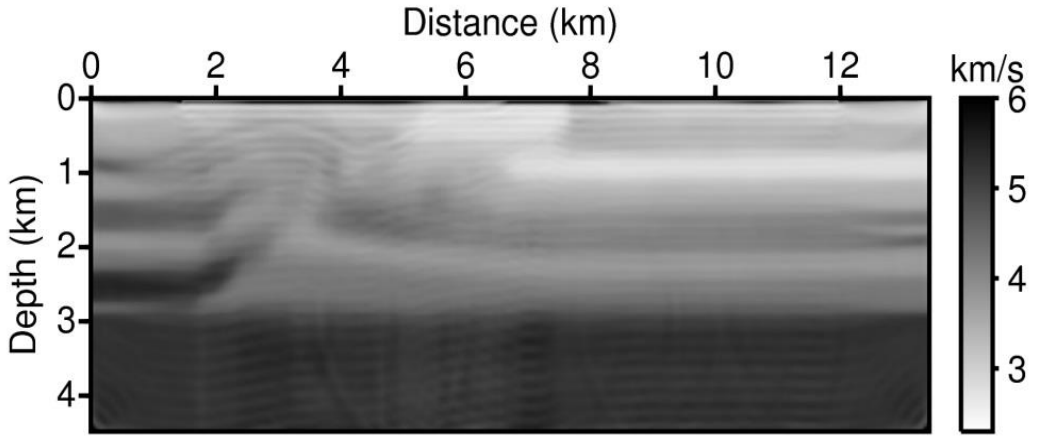
Distance (km)
0
2
4
6
8
10
12
km/s
6
5
4
3
Depth (km)
0
1
2
3
4

(a)

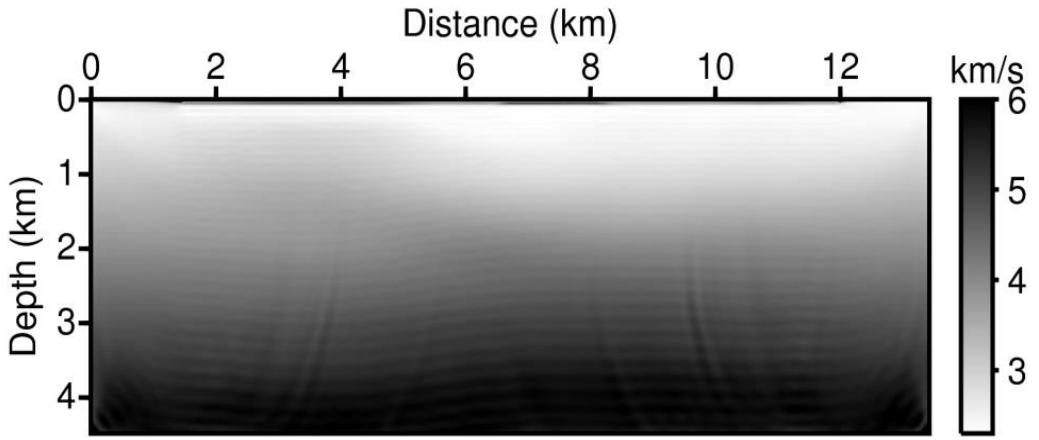
Distance (km)
0
2
4
6
8
10
12
km/s
6
5
4
3
Depth (km)
0
1
2
3
4

(b)

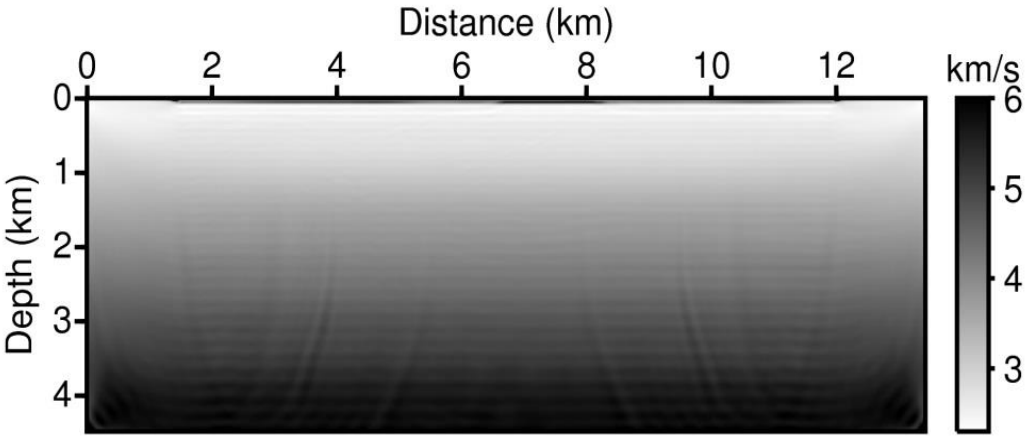

(c)

Figure 4.4. Inverted velocity models with l2-norm objective function and 250th iteration from (a) CDR macro-velocity model, (b) Laplace-domain inverted model and (c) linearly increasing model.

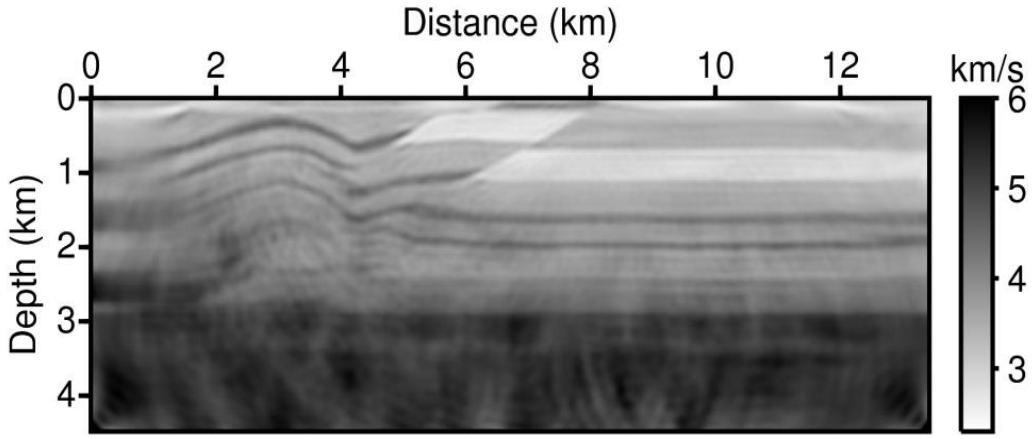
Distance (km)
0
2
4
6
8
10
12
km/s
6
5
4
3
Depth (km)
0
1
2
3
4

(a)

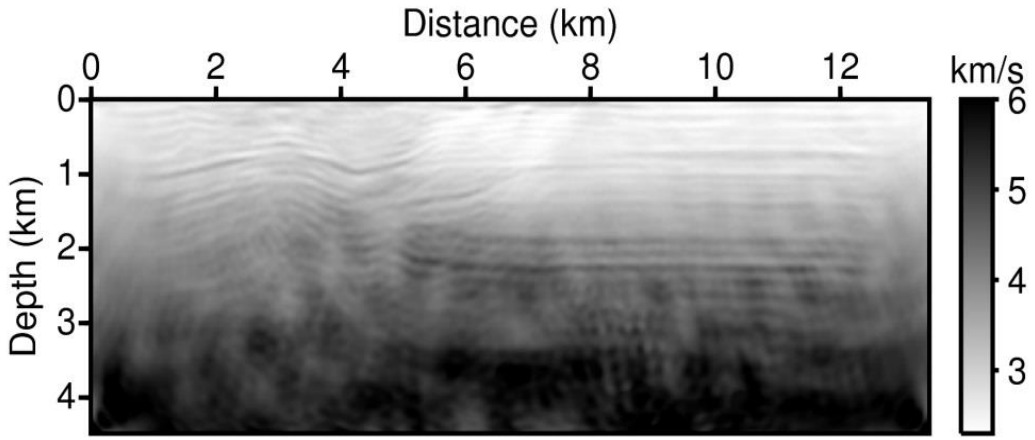
Distance (km)
0
2
4
6
8
10
12
km/s
6
5
4
3
Depth (km)
0
1
2
3
4

(b)

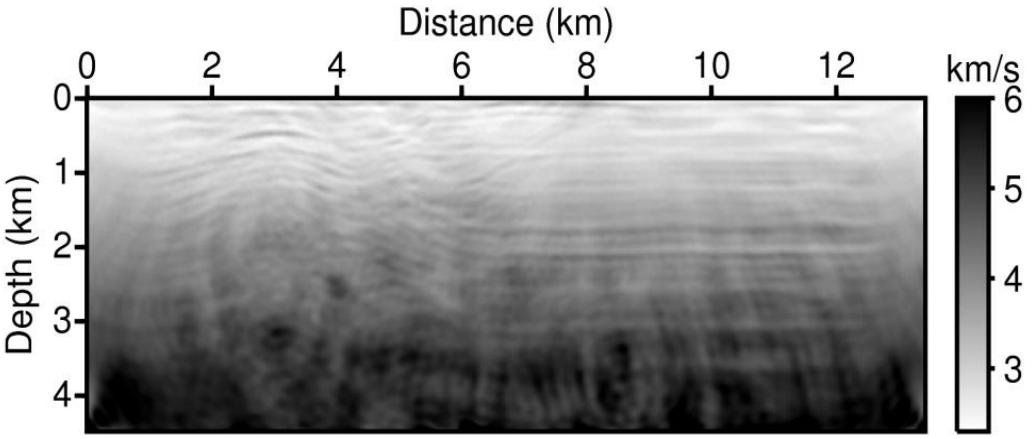

(c)

Figure 4.5. Inverted velocity models with logarithmic objective function and 250th iteration from (a) CDR macro-velocity model, (b) Laplace-domain inverted model and (c) linearly increasing model.

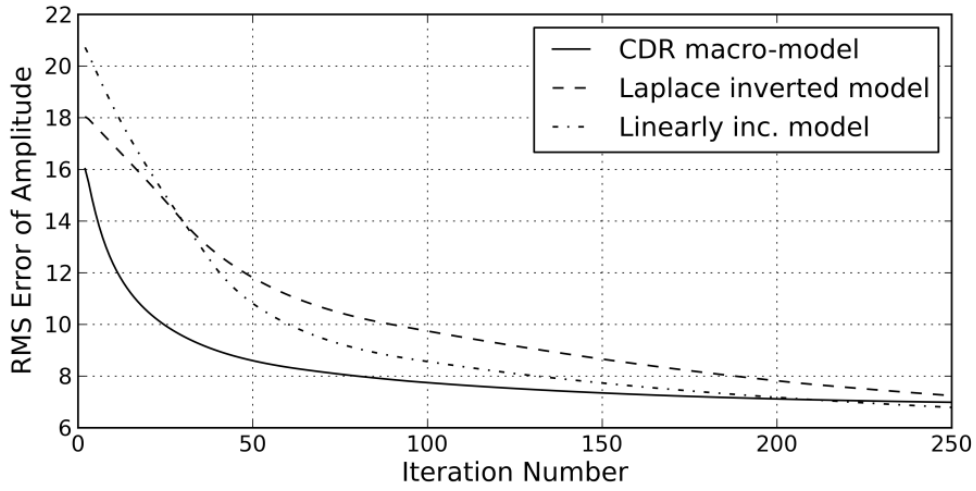

(a)

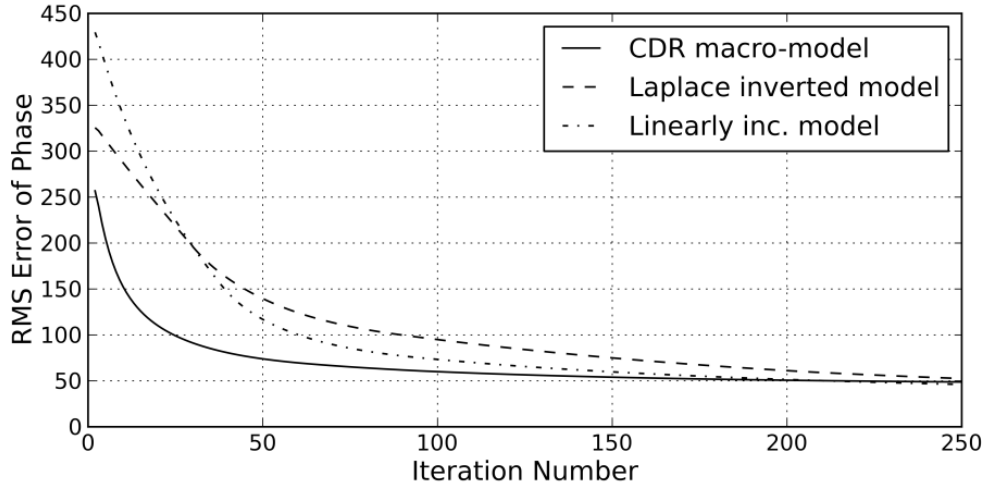

(b)

Figure 4.6. The RMS error curve of (a) the amplitude and (b) the phase in the l2-norm objective function. The RMS errors of three models show a tendency to converge to a constant value.

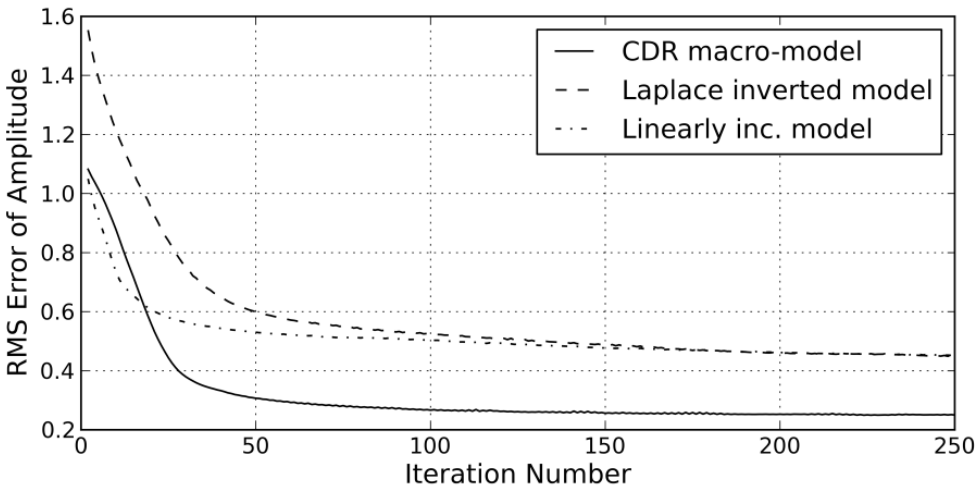

(a)

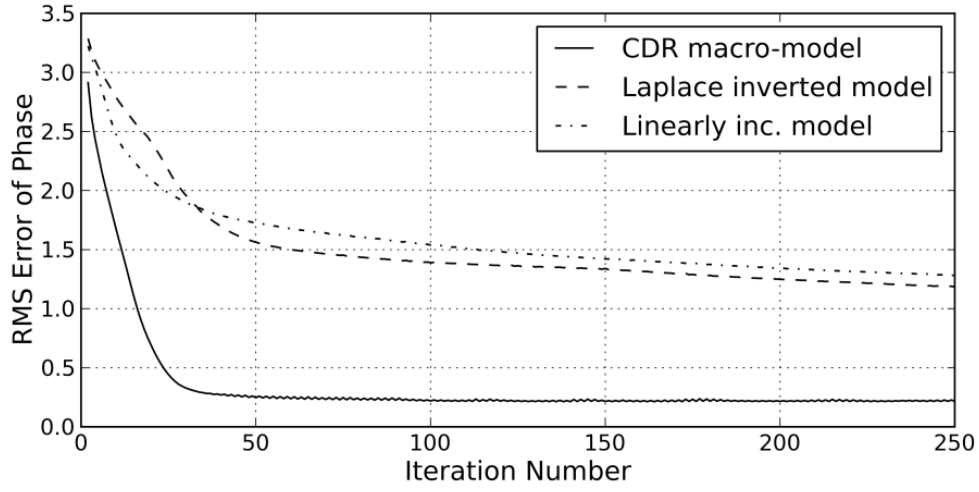

(b)

Figure 4.7. The RMS error curve of (a) the amplitude and (b) the phase in the logarithmic objective function. The RMS errors of the amplitude and the phase are shown the smallest value in the CDR model. The errors of other two models are very similar, but the Laplace model has a little smaller error.

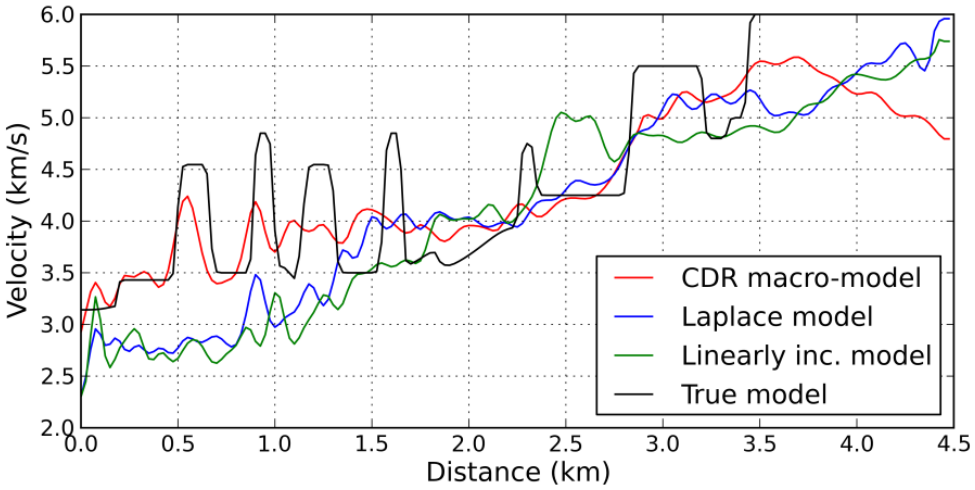
Velocity (km/s)
Distance (km)
CDR macro-model
Laplace model
Linearly inc. model
True model

(a)

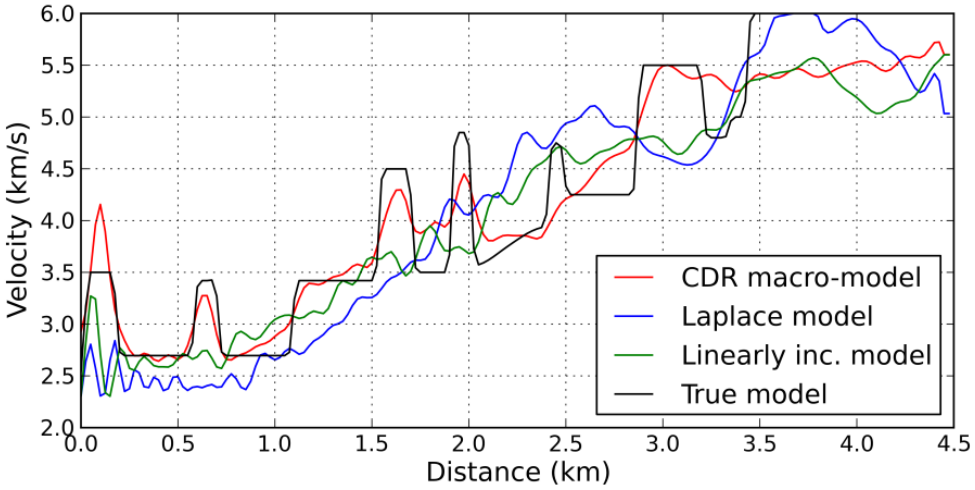
Velocity (km/s)
Distance (km)
CDR macro-model
Laplace model
Linearly inc. model
True model

(b)

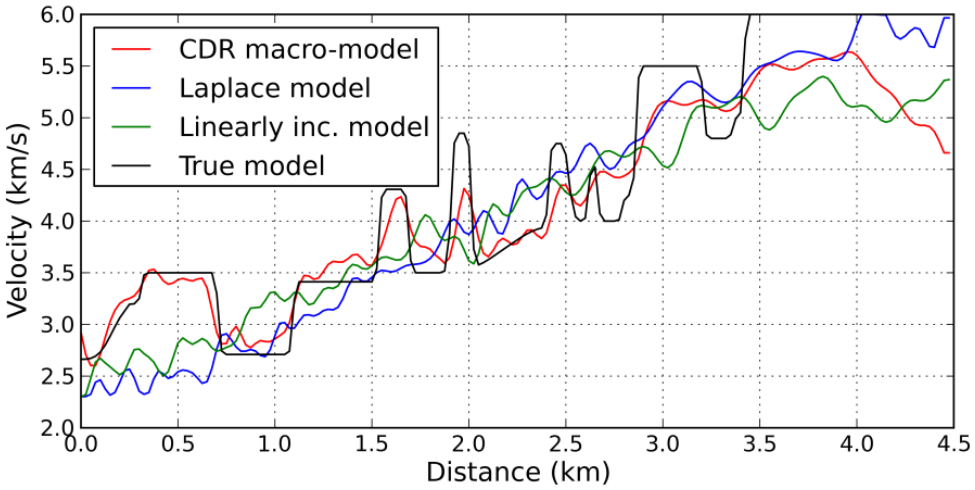

(c)

Figure 4.8. Depth profiles of inverted models Figure 4.5 at (a) 4 km, (b) 7 km and (c) 10 km point. The velocity of CDR model follows very similar trend with true velocity than of Laplace inverted model especially in (b) and (c).

This realistic synthetic seismic data has very short recording time and complex structure. The recording time is only 2.8 sec. The short recording time and shallow high velocity layers affect adversely to recover the deep velocity structure. For this reason, the inversion of three methods showed poor results in the deep structure.

The weathered zone also gives a great influence on the inversion results. This Overthrust model has a weathered zone near surface, and it leads to near-surface instability. To avoid these instabilities, the true velocity values are fixed on topside of the initial model during full waveform inversion (Ravaut et al., 2004; Ben-Hadj-Ali et al., 2011) or the model topside is artificially augmented (Sourbier et al., 2009). We used the first method to improve the inversion results. The true model is put to the 100 m depth of the each initial model and it is shown in Figure 4.9. The new initial model has same condition on the model size, gird size, shots and receivers, but it has only a fixed top layer of 100 m.

The inverted results corresponding to the initial model of Figure 4.9 is Figure 4.10. The 250 iterations were performed like the previous inversion. The inverted models showed the improved results than Figure 4.5, especially the Laplace model (Figure 4.10(b)). Comparing the RMS error of three results in Figure 4.11, we can see that the Laplace model showed a lot of improvement. The Laplace inverted model did not find velocity structure well in the previous seismic data with non-fixed weathered zone but it recovered velocities well in this seismic data with fixed weathered. On the other hand, CDR macro-model appeared good inverted results regardless of weathered

zone. This demonstrates that the CDR macro-model has strength when the FWI is applied to the seismic data with weathered zone.

This experiment was possible because the Overthrust data is a synthetic model. Knowing the presence and location of the weathered zone contributes largely to fixing accurate points. With the real data you cannot pinpoint the geological structure, so it is difficult to fully apply this method as a synthetic data. Therefore, the CDR model is more advantageous on the real seismic data inversion.

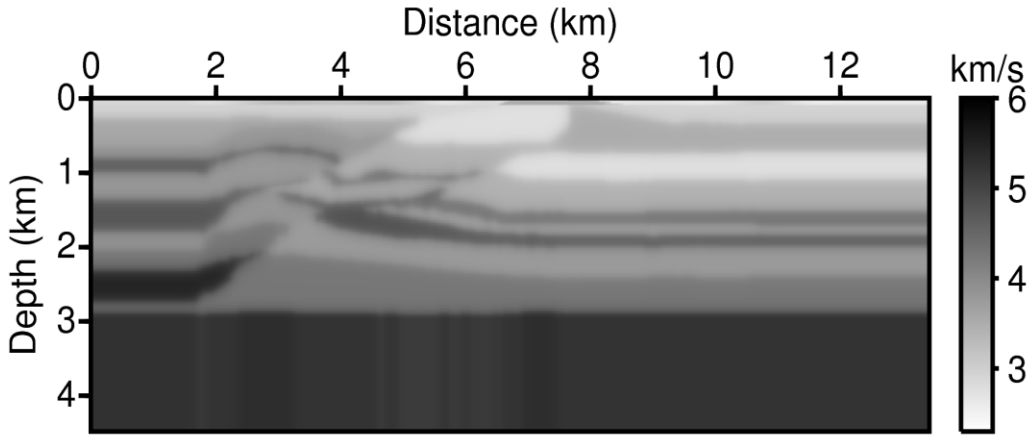
Distance (km)
0
2
4
6
8
10
12
km/s
6
5
4
3
Depth (km)
0
1
2
3
4

(a)

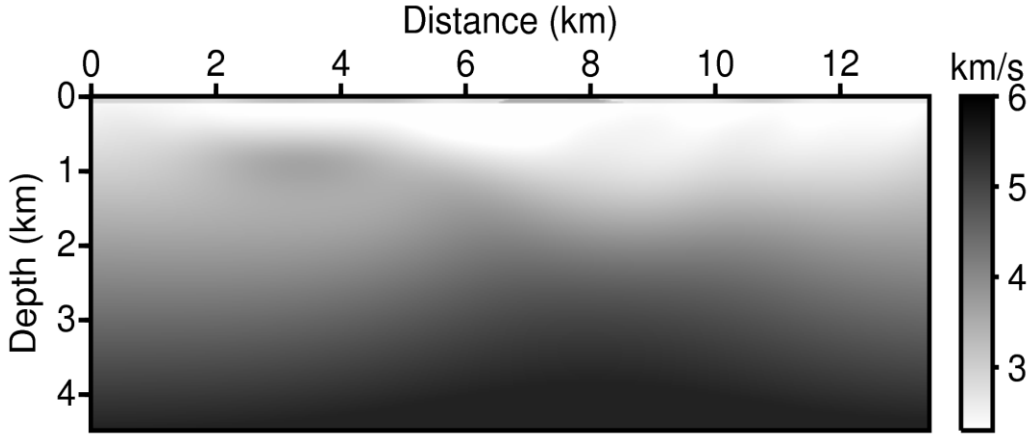
Distance (km)
0
2
4
6
8
10
12
km/s
6
5
4
3
Depth (km)
0
1
2
3
4

(b)

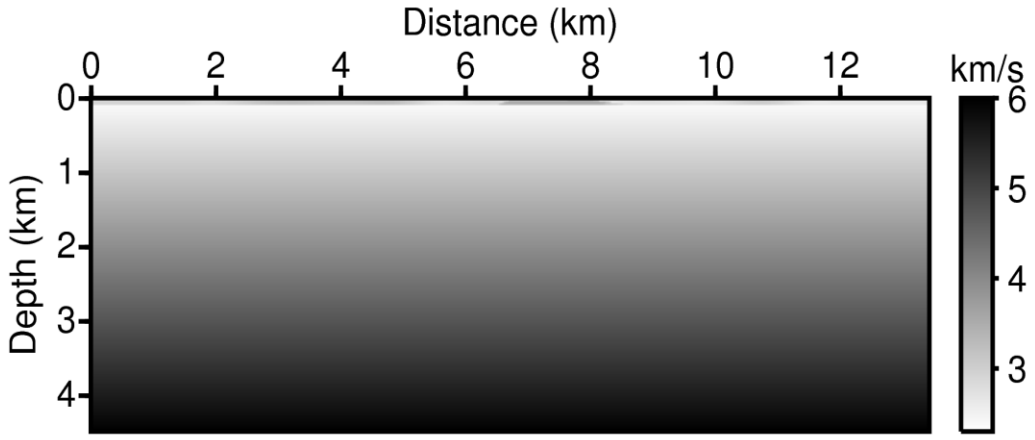

(c)

Figure 4.9. Initial models of new velocity model by using (a) CDR macro-velocity model, (b) Laplace-domain inverted model and (c) linearly increasing model. The topside (100 m) is fixed on true velocity.

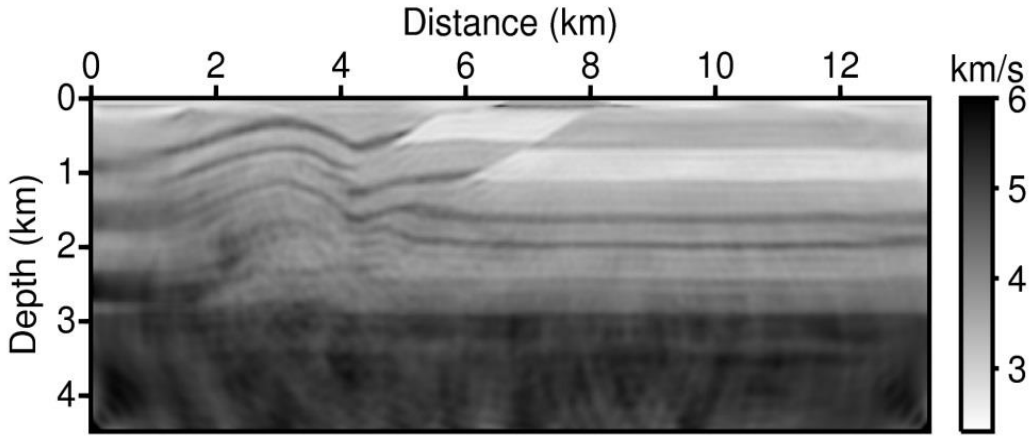
Distance (km)
0
2
4
6
8
10
12
km/s
6
5
4
3
Depth (km)
0
1
2
3
4

(a)

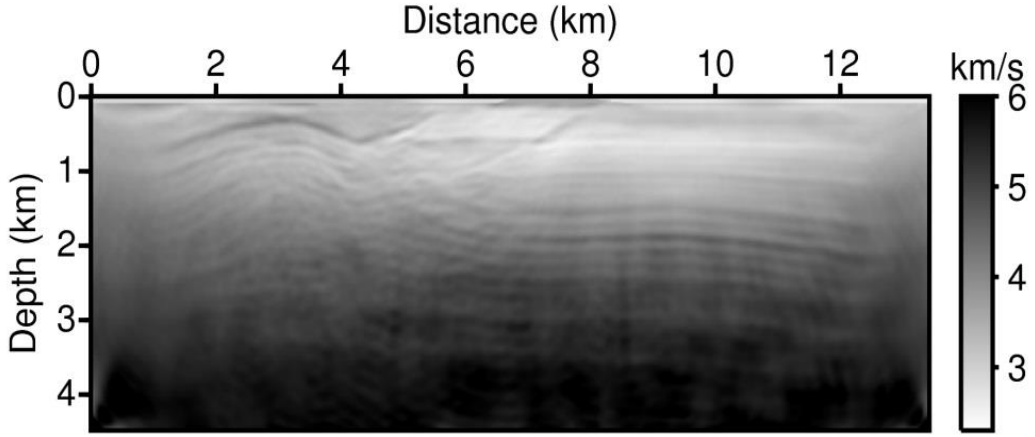
Distance (km)
0
2
4
6
8
10
12
km/s
6
5
4
3
Depth (km)
0
1
2
3
4

(b)

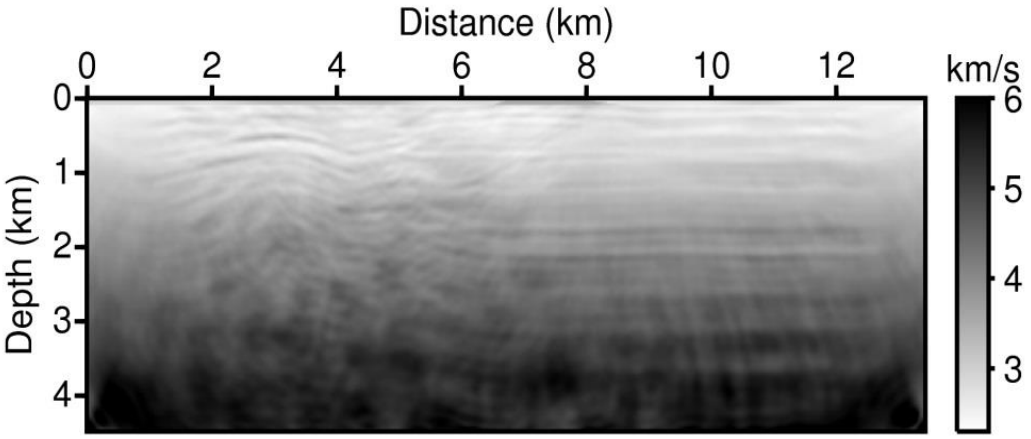

(c)

Figure 4.10. Inverted models of new velocity model with logarithmic objective function and from (a) CDR macro-velocity model, (b) Laplace-domain inverted model and (c) linearly increasing model.

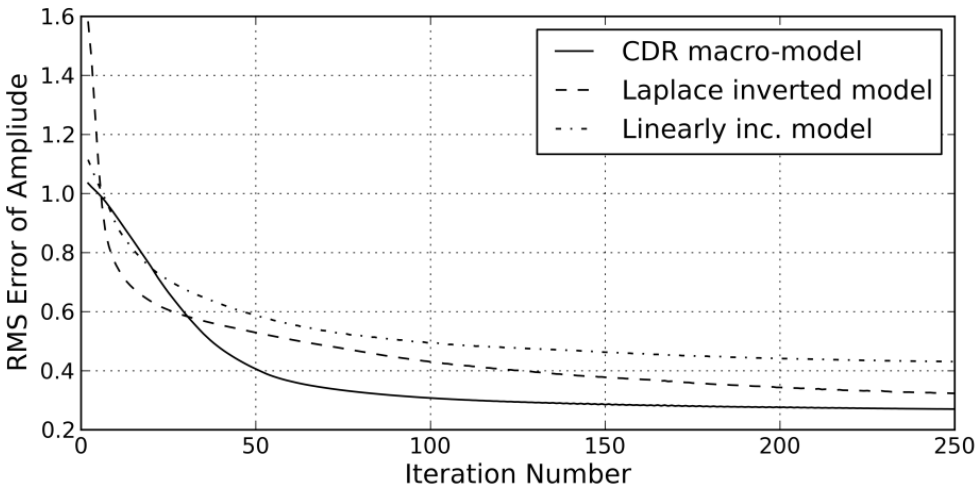

(a)

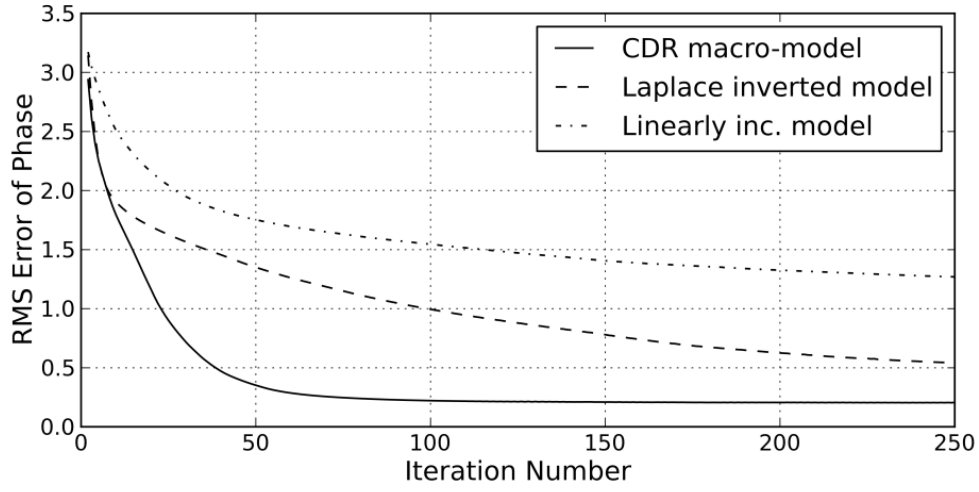

(b)

Figure 4.11. The RMS error of (a) amplitude and (b) phase of three inverted results. we can see that the Laplace model showed a lot of improvement.

In this time, we performed multi-parameter FWI for evaluating the scalability and availability of the CDR macro-model about it. In recent years, the ocean-bottom system (OBS) seismic data is sometimes acquired with the streamer seismic data during field exploration. The streamer and OBS are a kind of receivers. While streamer floats on the sea surface, OBS is placed on the seabed. In this case, the p-wave velocity model can be obtained from the CDR velocity analysis with the streamer data. We tested if this CDR velocity model can be used for multi-parameter inversion.

The streamer and OBS seismic data were made with the Overthrust velocity model. True velocity models was used the entire length of the Overthrust model and the water depth is 250 m (Figure 4.12). The streamer seismic data has only the pressure component using only p-wave velocity model (Figure 4.12(a)). On the other hand, the OBS seismic data has three components – pressure, horizontal and vertical displacement. Therefore, we can invert s-wave velocity and density as well as p-wave velocity from these three components. In the Figure 4.12(a) and (b), the p-wave and s-wave models seem to represent same velocities, but they have different velocity range (figure legend). In both seismic data, 121 shots were used with 100 m interval and 801 receivers were used with 25 m interval. The recording time is 8 sec.

Initial velocity models for multi-parameter FWI are shown in Figure 4.13. The initial model of p-wave velocity was obtained from the strip-off CDR velocity analysis on streamer data. The initial models of s-wave velocity and density were generated by using the Gadner's equation with p-wave velocity.

The Gadner's equation represents an empirical relationship among p-wave velocity, s-wave velocity and density.

$$v_s = 0.57 \times v_p \,, \qquad dens = 0.31 \times \left(v_p \times 10^3\right)^{0.25} \,, \tag{39}$$

where v_p is p-wave velocity, v_s is s-wave velocity and $dens$ is density of substructure.

The grid size is 25 m and the model size is 20 km x 5 km for inversion. Figure 4.14s are 500th inverted results with logarithmic objective function. The p- and s-wave velocity models are well-inverted, that is very similar to the true velocity models. Especially the marked area was well developed in detail even though it has high-velocity or complex value in shallow part. Therefore, we confirmed applicability on multi-parameter inversion of the CDR macro-model from these results.

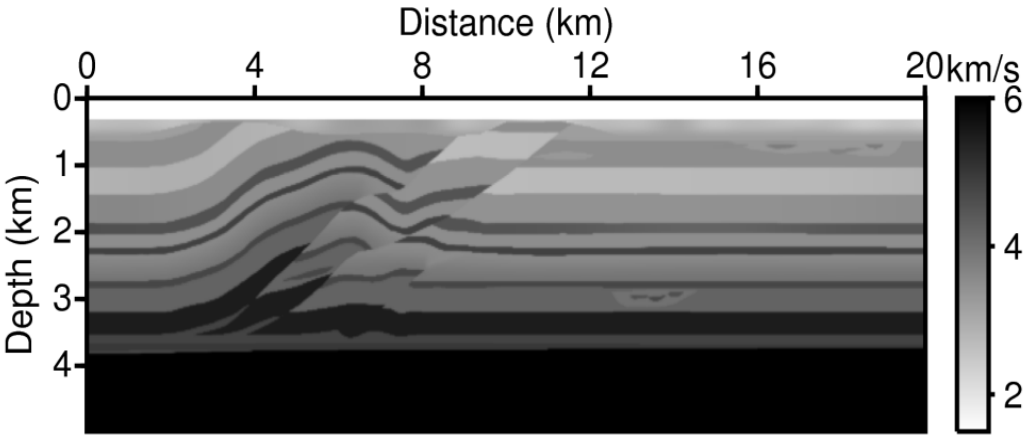
Distance (km)
0
4
8
12
16
20
km/s
Depth (km)
0
1
2
3
4
6
4
2

(a)

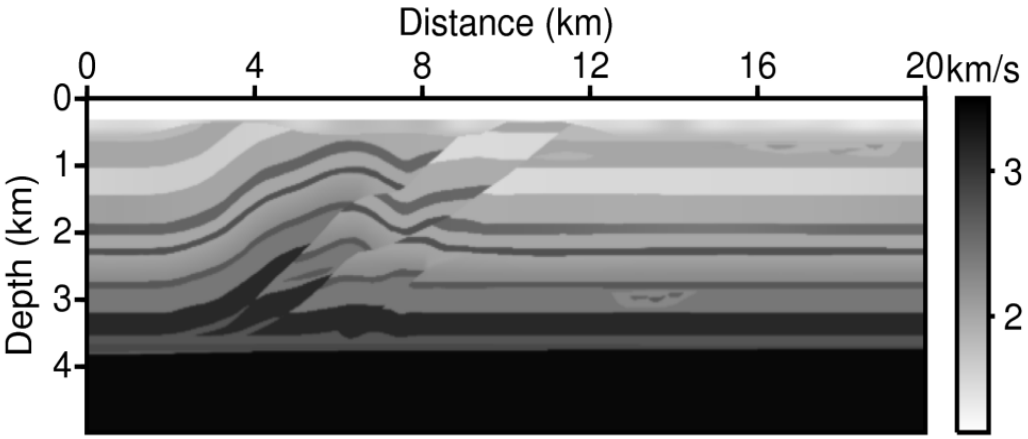
Distance (km)
0
4
8
12
16
20
km/s
Depth (km)
0
1
2
3
4
3
2

(b)

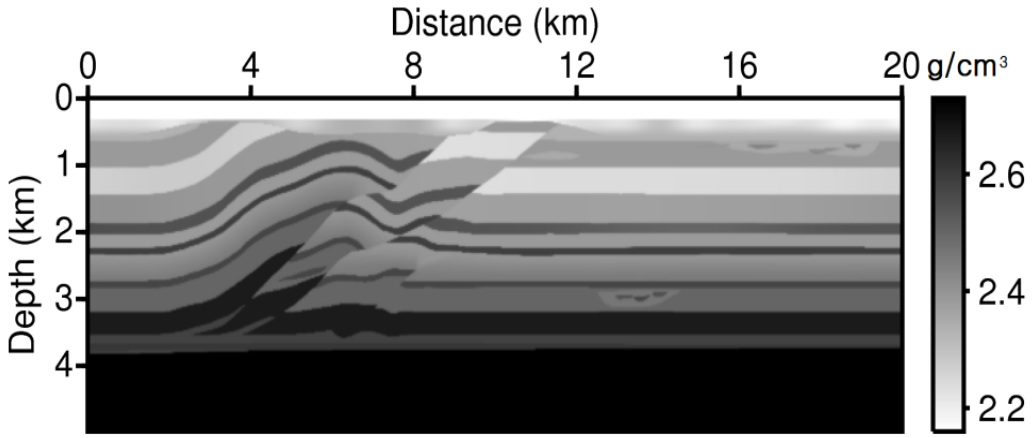

(c)

Figure 4.12. True models of (a) p-wave velocity, (b) s-wave velocity and (c) density. The ocean-bottom system (OBS) seismic data is acquired in the seabed.

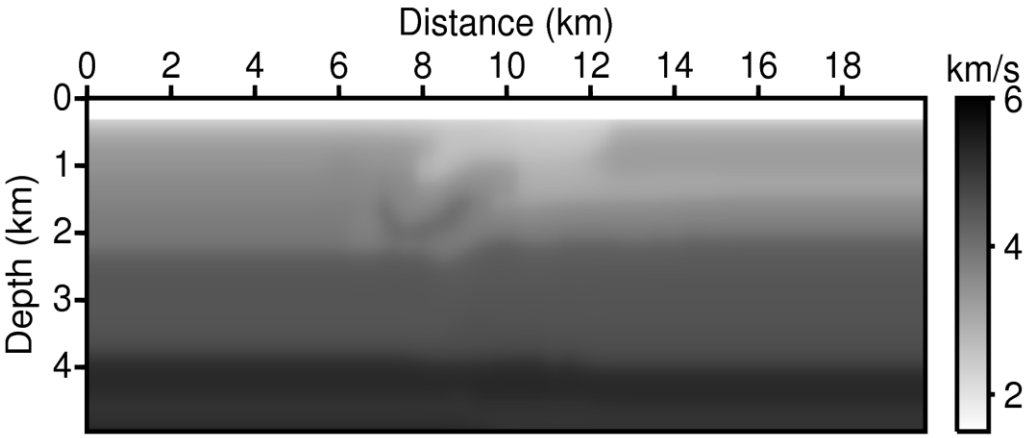
Distance (km)
0 2 4 6 8 10 12 14 16 18
km/s
6
4
2
Depth (km)
0 1 2 3 4

(a)

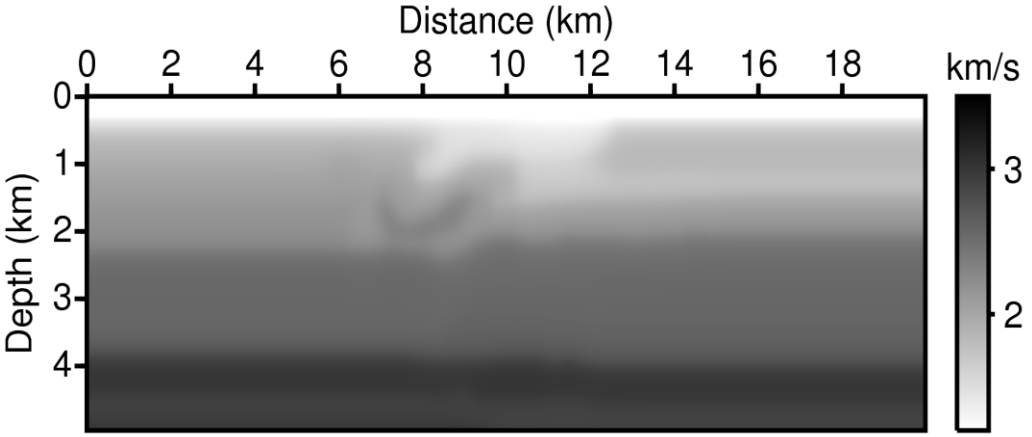
Distance (km)
0 2 4 6 8 10 12 14 16 18
km/s
3
2
Depth (km)
0 1 2 3 4

(b)

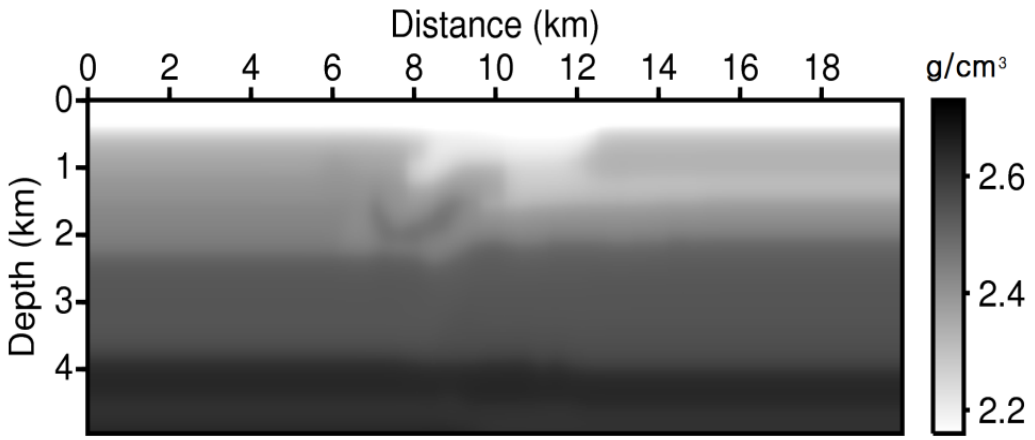

(c)

Figure 4.13. Initial models of (a) p-wave velocity, (b) s-wave velocity and (c) density using CDR macro-model. The initial model of p-wave velocity was obtained from the strip-off CDR velocity analysis on streamer data. The initial models of s-wave velocity and density were generated by using the Gadner's equation with p-wave velocity.

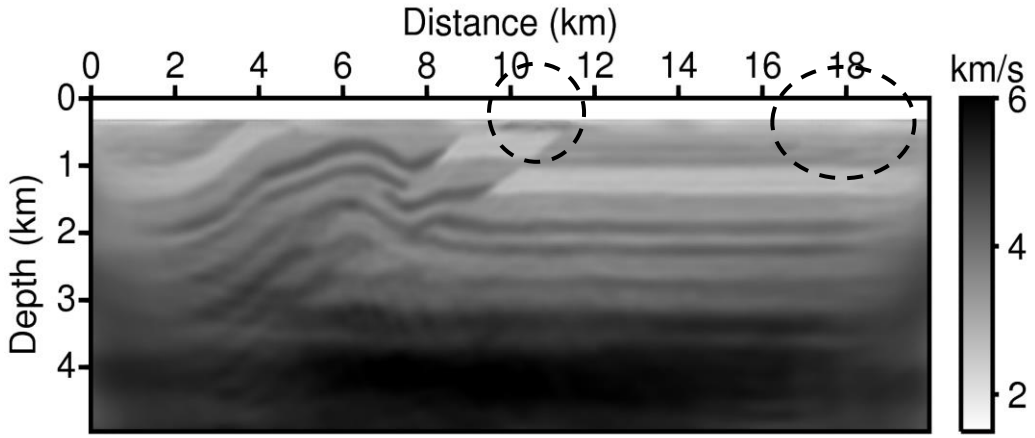
Distance (km)
0
2
4
6
8
10
12
14
16
18
km/s
6
4
2
Depth (km)
0
1
2
3
4

(a)

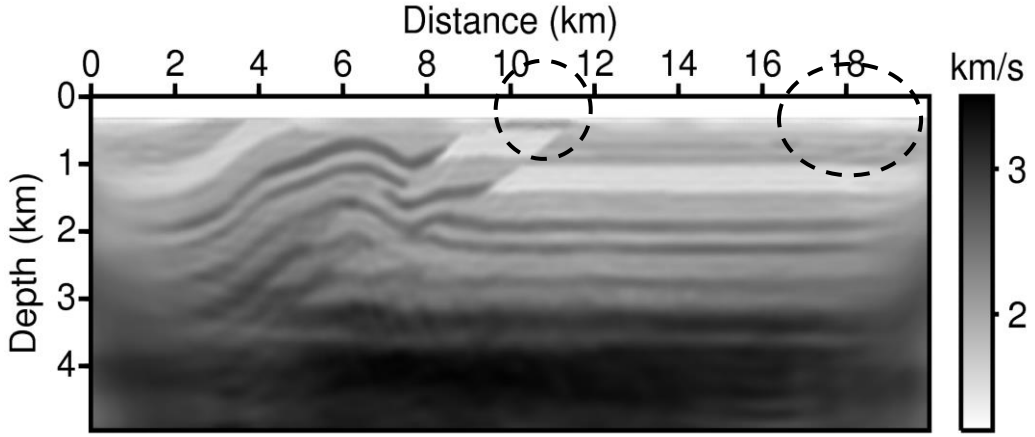
Distance (km)
0
2
4
6
8
10
12
14
16
18
km/s
3
2
Depth (km)
0
1
2
3
4

(b)

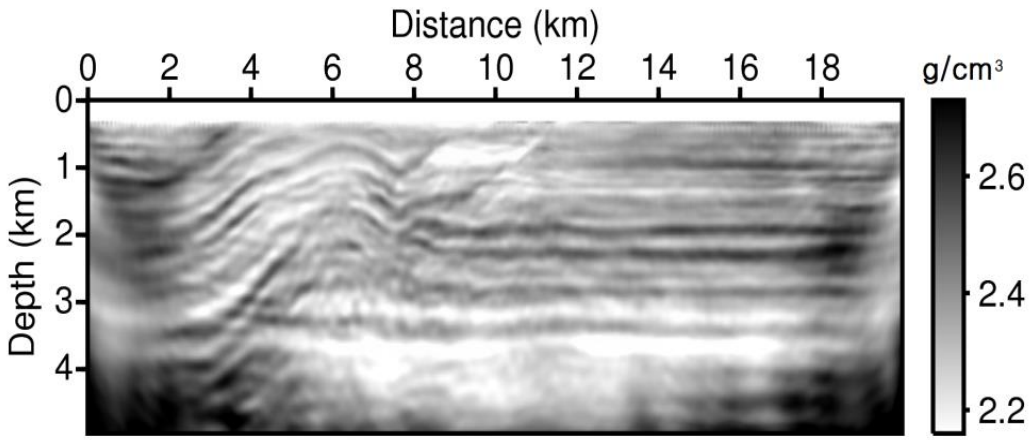

(c)

Figure 4.14. Inverted models with logarithmic objective function (500th iteration) of (a) p-wave velocity, (b) s-wave velocity and (c) density using the CDR macro-model. The p- and s-wave velocity models are well-inverted, that is very similar to the true velocity models. Especially the marked area was well developed in detail even though it has high-velocity or complex value in shallow part.

4.2 Marmousi synthetic model

Marmousi model is also synthetic model that made based on real subsurface structure (Figure 4.15). The released seismic data obtained by assuming the real acquisition environment with this realistic synthetic model has several problems such as very short offset and thin water layer. The offset ranges from 200 to 2,575 m and the water depth ranges from 24 to 40 m. There are 240 shots with a shot interval of 25 m and 96 receivers with a receiver interval of 25 m. The maximum recording length is 2.89 s and the time sampling interval is 4 ms.

The initial velocity models were displayed in Figure 4.16. Figure 4.16(a) is obtained by the same CDR method as introduced in the section 3. Figure 4.16(b) is obtained from Laplace-domain full-waveform inversion. Six Laplace damping constants are used from 2 to 12 with an interval of 2, and a logarithmic objective function is applied. It used 50^{th} iteration result as an initial model based on the error curve. Figure 4.16(c) is linearly increasing model from 1.5 to 5.5 km/s.

We drew up the depth profile of two points. 3 km vertical line has a complex velocity structure with faults and 5 km vertical line has high velocity zone in the deep part. The resulting graph is shown in Figure 4.17. We can see that the CDR macro-model follows the trend of the true model well. CDR macro-model didn’t find high or low velocity layer well, but it gently follow the true velocity with median level values. On the other hand, Laplace inverted model is more sensitive on high velocity of true model. The tendency

about following the high velocity is shown well in both Figure 4.17(a) and (b).

FWI was performed by using the initial model of Figure 4.16. We also used both l_2-norm and logarithmic objective function. The model size is 8.0 km x 3 km and the grid interval is 25m, so it has 320 x 120 elements. The shot for inversion is used 210 with 25 m interval. Frequencies are selected from 0.5 to 15.2 Hz with 0.3 Hz intervals for inversion. The 200^{th} inverted results are shown in Figure 4.18 and 4.19.

In the Marmousi model, the results of both objective functions are hard to discriminate between merits and demerits. The results of the l_2-norm objective functions (Figure 4.18) showed the overall smooth velocity model while the results of the logarithmic objective function (Figure 4.19) expressed more precise boundary of layers. Anyway, the CDR macro-model show best result in both objective functions. We drew the RMS error curve to compare the residuals. Because the residual scale of both objective functions differ each other, these are represented each in Figure 4.20 and 4.21. The phase error of the l_2-norm objective function (Figure 4.20(b)) is reduced more rapidly as the number of iteration increases. The error of Laplace inverted model is a little smaller in the beginning, but the error of CDR macro-model decreases markedly after the 60^{th} iteration. The phase error of the logarithmic objective function (Figure 4.21(b)) is reduced more slowly as the number of iteration increases. The error of CDR macro-model represents reliably smallest error from the beginning.

Figure 4.22 shows the depth profile of the inverted results at 3 and 5 km

point. The results of both objective functions of the CDR macro-model and Laplace inverted model are represented with the true velocity model. The velocities of CDR macro-model show high fitness particularly in the shallow part, and the Laplace model are inverted generally into high velocity than true velocity. It is difficult to find true velocity in Laplace inverted model because the initial model was estimated already into very high velocity. In order to compare the results of both objective functions in detail, we drew the depth profile to only 1 km depth (Figure 4.23). These graphs were made by using only the result of CDR macro-model that showed the best result among three models. The result of l2-norm objective function was less sensitive to sudden changes in velocity but represented a smooth velocity changes. On the other hand, the result of logarithmic objective function was more sensitive to velocity changes, so the velocities were sometimes over-estimated in high velocity and under-estimated in low-velocity. We judged that this phenomenon was related to the scale of residual. In shown in error curve of Figure 4.20 and 4.21, the residual scale of l2-norm objective function is 5-6 times greater than that of logarithmic objective function. Therefore, the logarithmic objective function showed clearer boundaries in Figure 4.19 because of small scale of measurement tool.

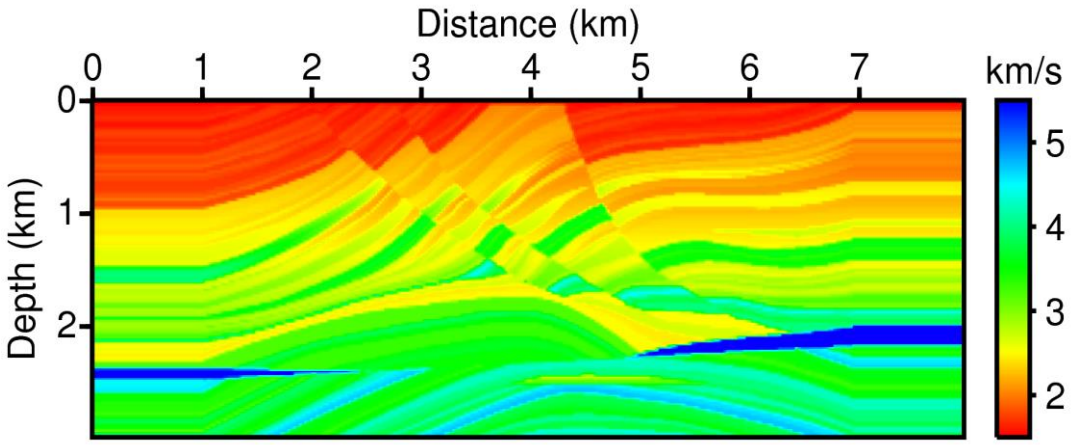

Figure 4.15. Marmousi velocity model. It is also synthetic model that made based on real subsurface structure. The released seismic data obtained by assuming the real acquisition environment and it has several problems such as very short offset and thin water layer.

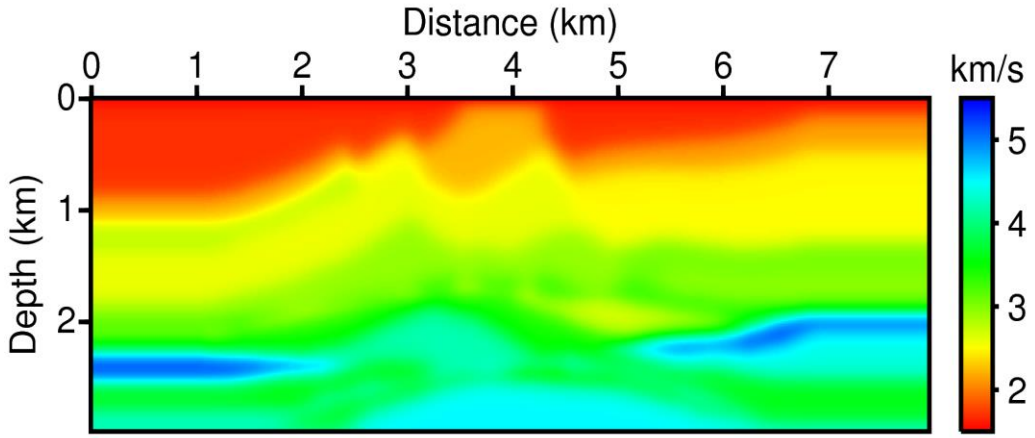
Distance (km)
0
1
2
3
4
5
6
7
km/s
Depth (km)
0
1
2
5
4
3
2

(a)

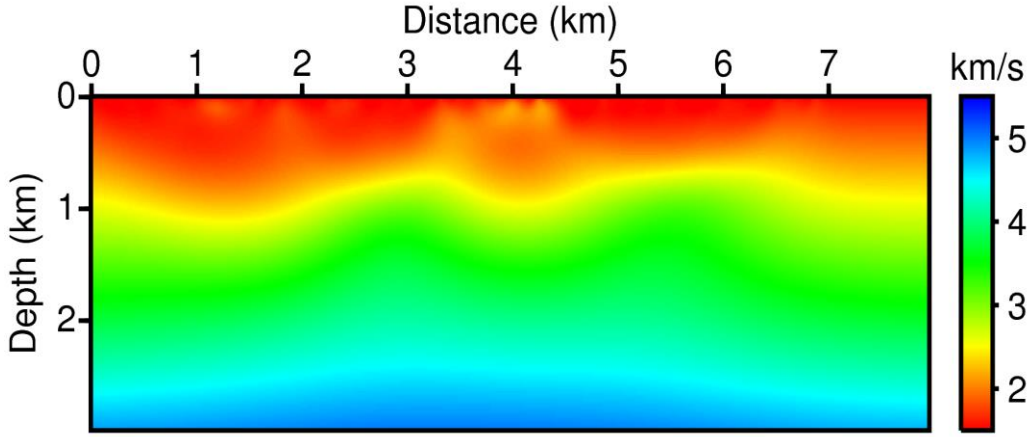
Distance (km)
0
1
2
3
4
5
6
7
km/s
Depth (km)
0
1
2
5
4
3
2

(b)

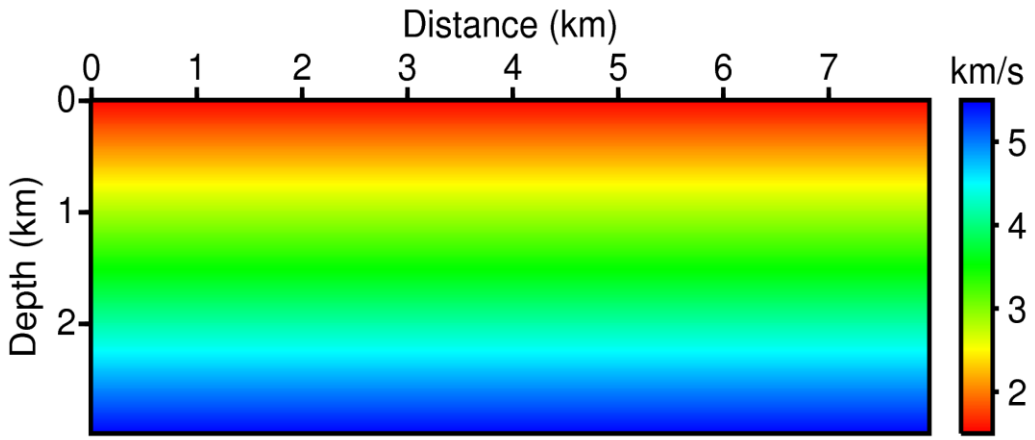

(c)

Figure 4.16. Initial models of Marmousi velocity model by using (a) CDR macro-velocity model, (b) Laplace-domain inverted model and (c) linearly increasing model. In the Laplace-domain FWI, six Laplace damping constants are used from 2 to 12 with an interval of 2 (50^{th} iteration result). The velocities of (c) are linearly increasing from 1.5 to 5.5 km/s.

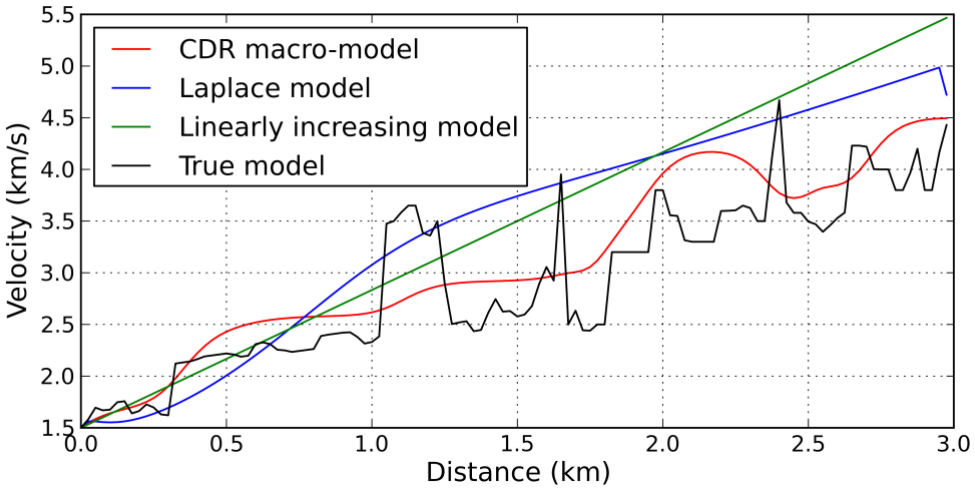

(a)

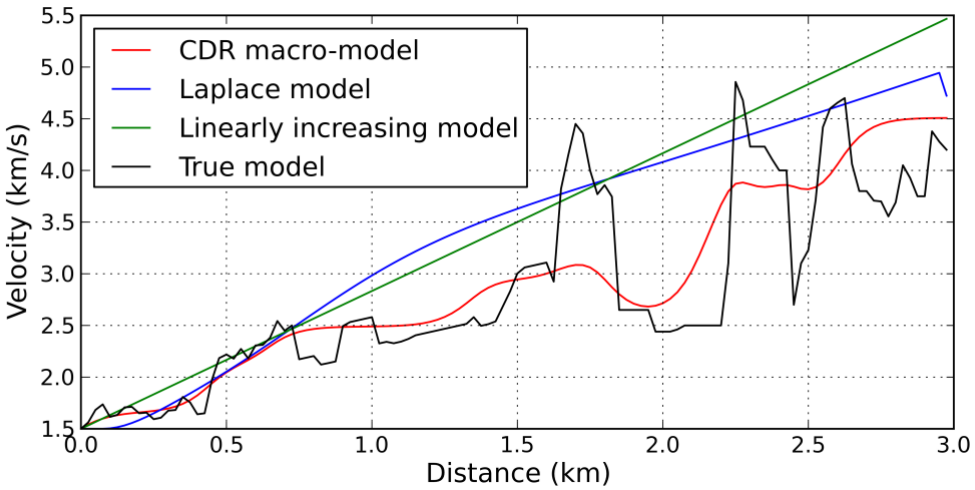

(b)

Figure 4.17. Depth profiles of initial models at (a) 3 km and (b) 5 km point. 3 km vertical line has a complex velocity structure with faults and 5 km vertical line has high velocity zone in the deep part.

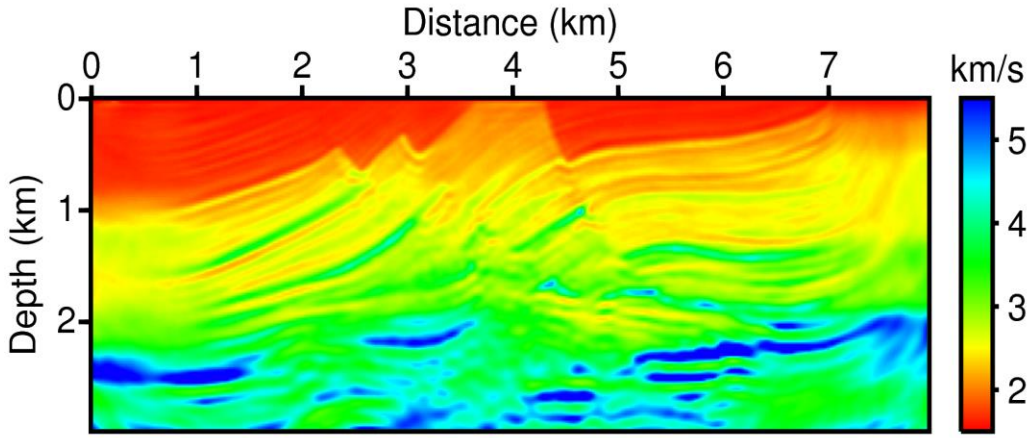
Distance (km)
0
1
2
3
4
5
6
7
Depth (km)
0
1
2
km/s
5
4
3
2

(a)

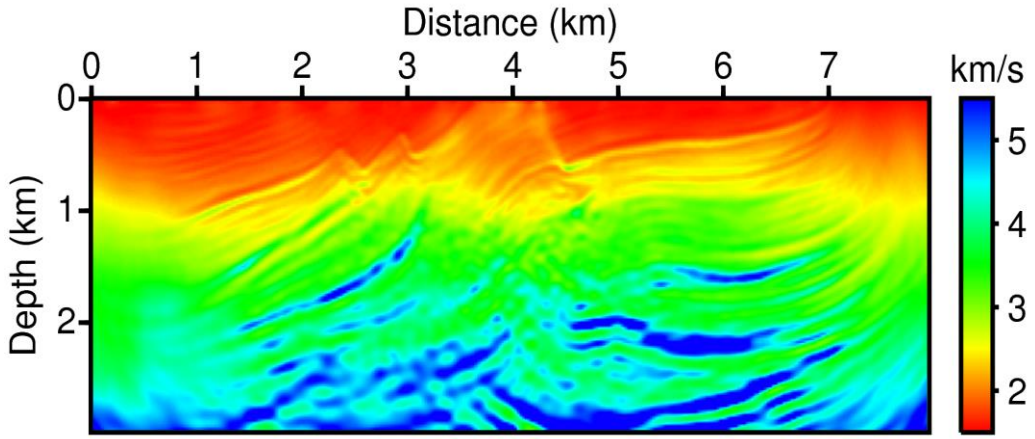
Distance (km)
0
1
2
3
4
5
6
7
Depth (km)
0
1
2
km/s
5
4
3
2

(b)

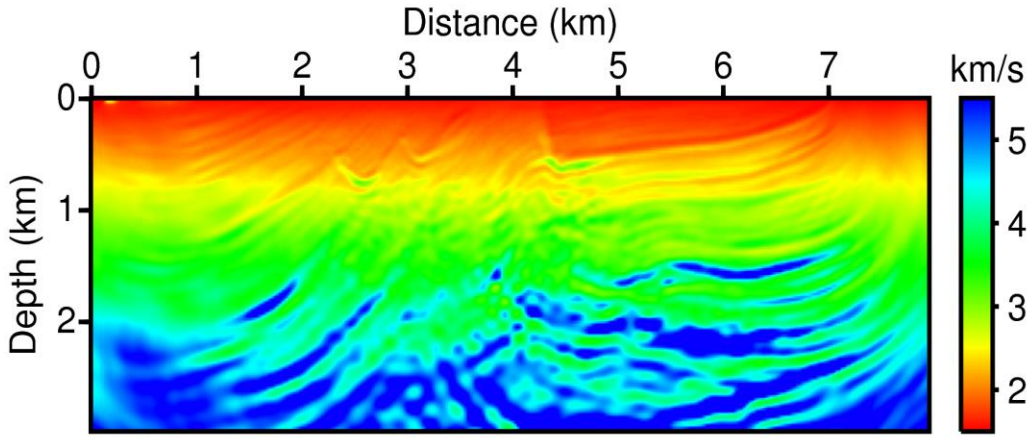

(c)

Figure 4.18. Inverted velocity models with l2-norm objective function and 200th iteration from (a) CDR macro-velocity model, (b) Laplace-domain inverted model and (c) linearly increasing model.

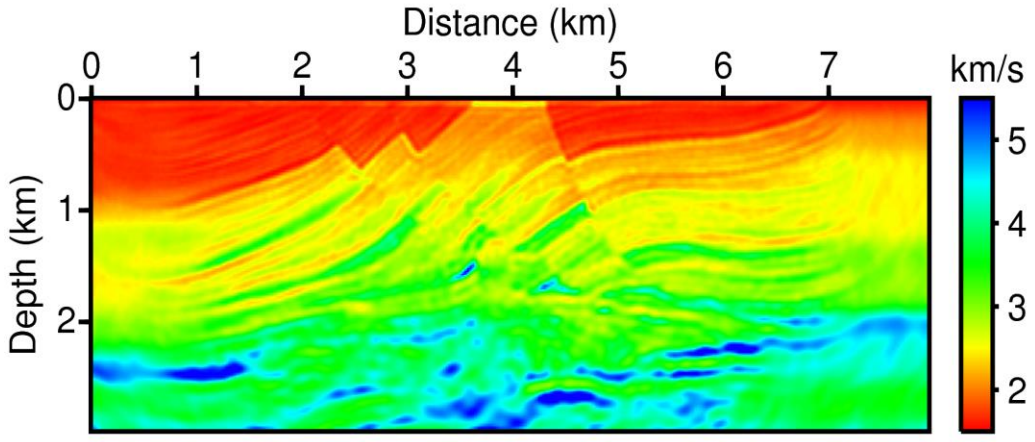
Distance (km)
0
1
2
3
4
5
6
7
Depth (km)
0
1
2
km/s
5
4
3
2

(a)

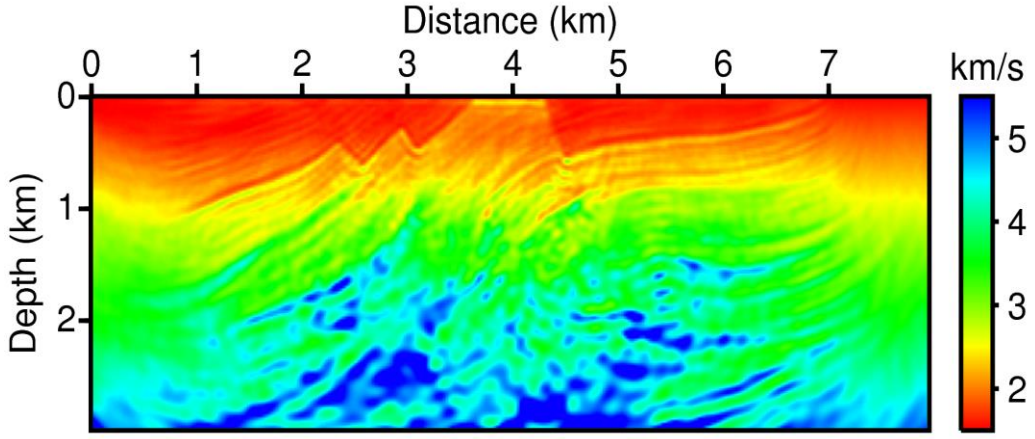
Distance (km)
0
1
2
3
4
5
6
7
Depth (km)
0
1
2
km/s
5
4
3
2

(b)

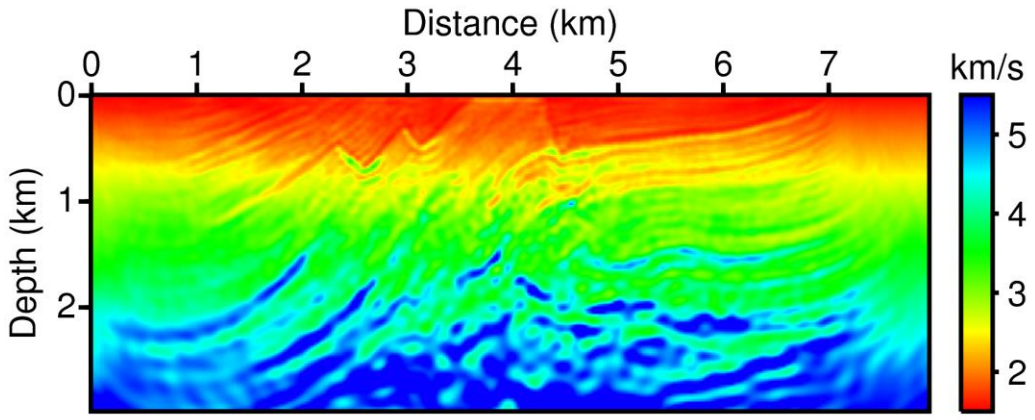

(c)

Figure 4.19. Inverted velocity models with logarithmic objective function and 200th iteration from (a) CDR macro-velocity model, (b) Laplace-domain inverted model and (c) linearly increasing model.

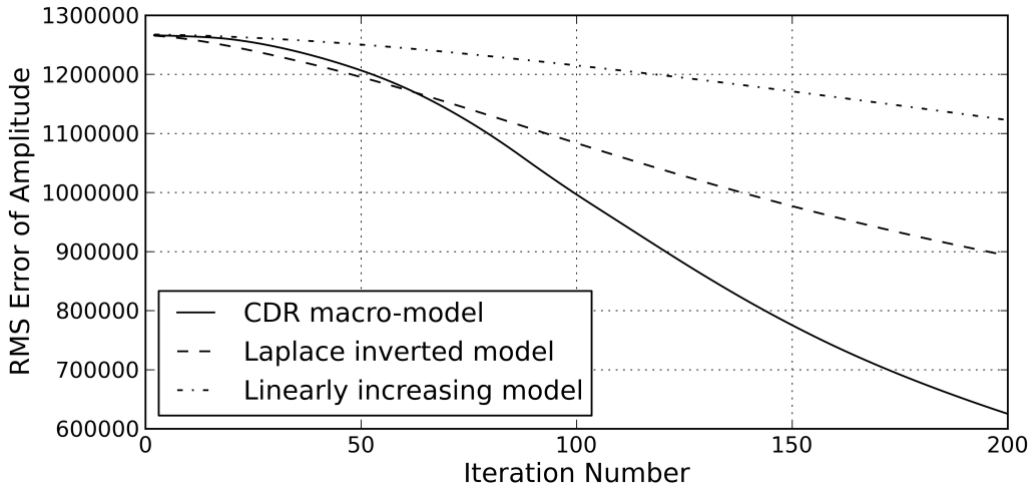

(a)

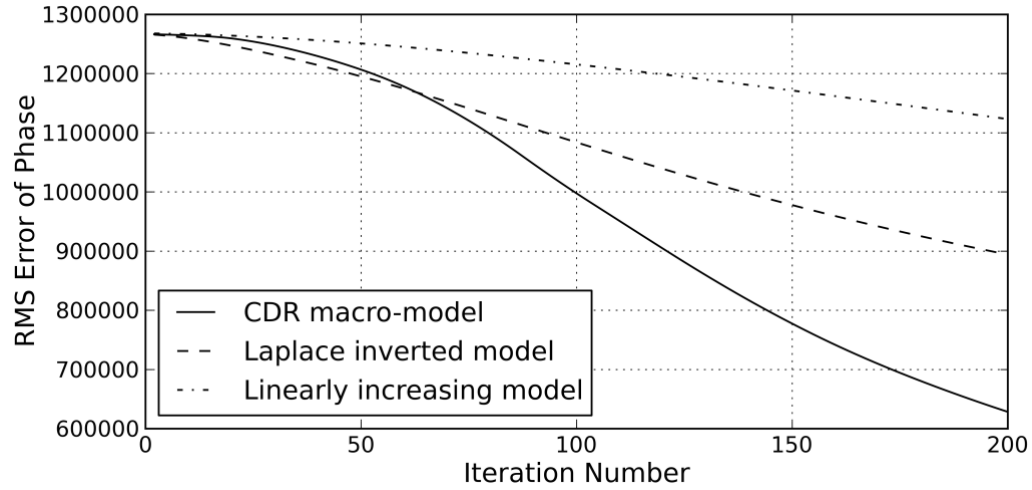

(b)

Figure 4.20. (a) Amplitude and (b) phase RMS error curve of the inverted model by the l2-norm objective function.

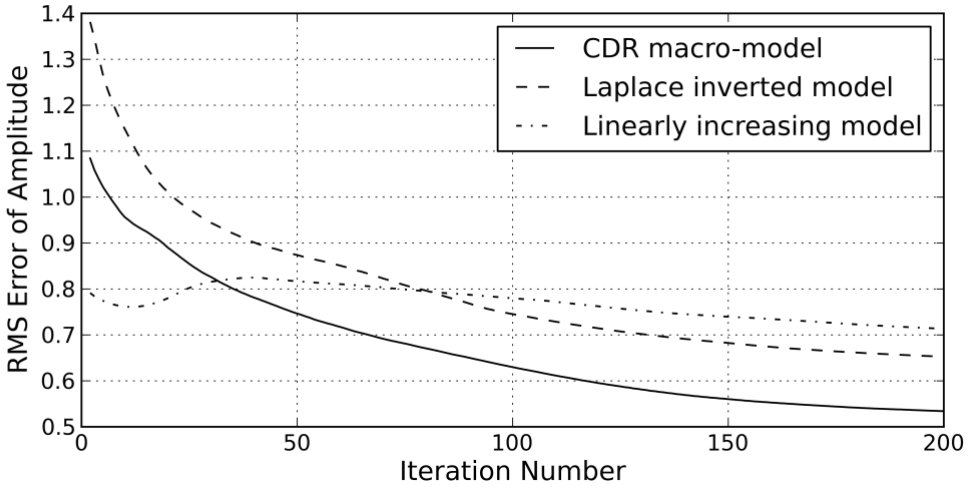

(a)

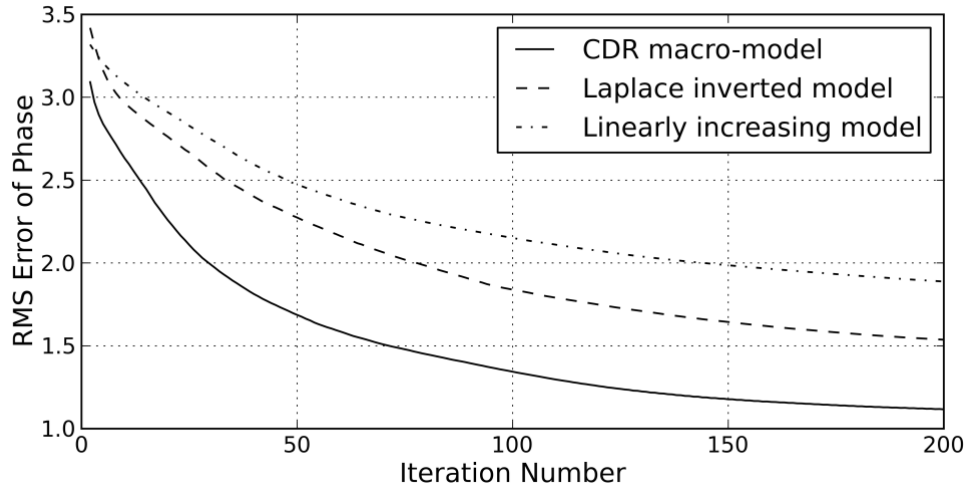

(b)

Figure 4.21. (a) Amplitude and (b) phase RMS error curve of the inverted model by the logarithmic objective function.

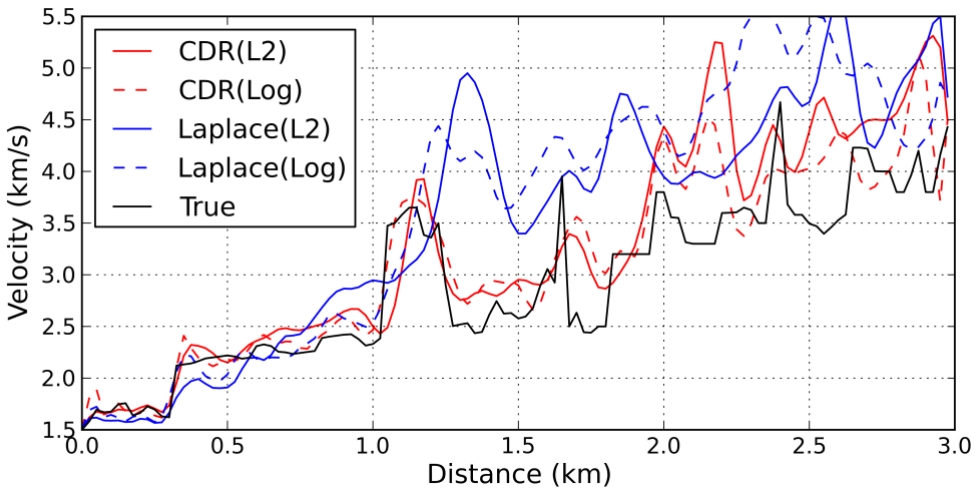

(a)

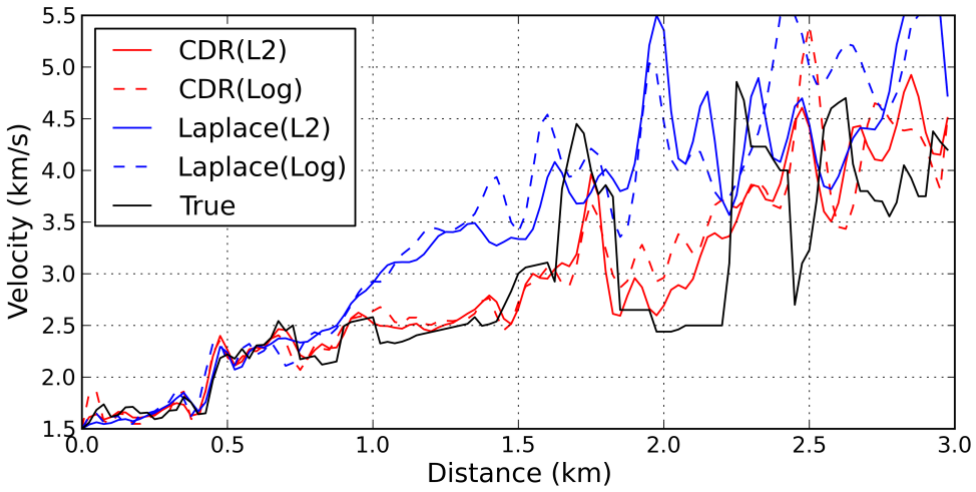

(b)

Figure 4.22. Depth profiles of inverted models at (a) 3 km and (b) 5 km point. The velocities of CDR macro-model show high fitness particularly in the shallow part, and the Laplace model are inverted generally into high velocity than true velocity.

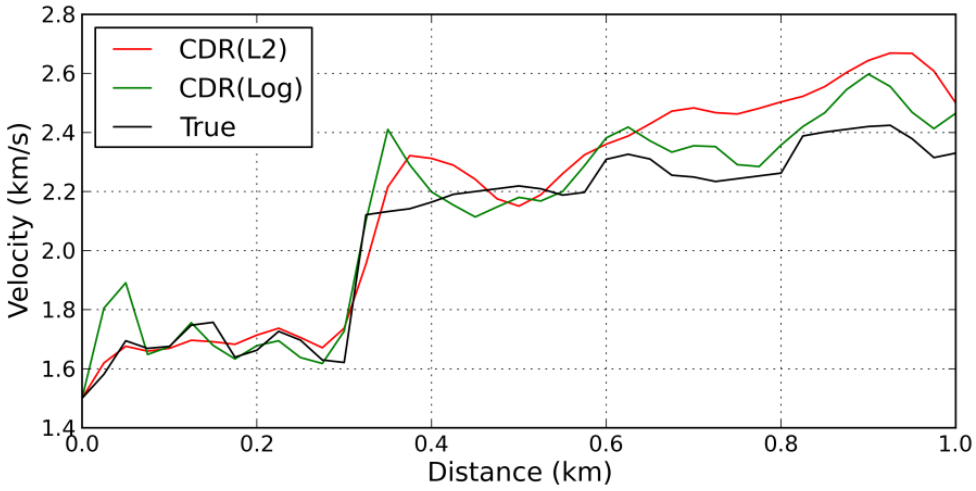

(a)

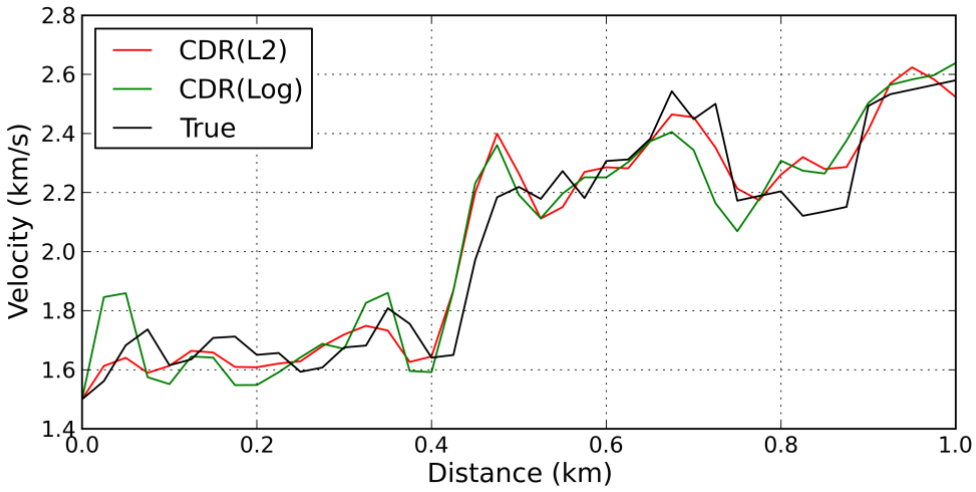

(b)

Figure 4.23. 1 km depth profiles of inverted models of CDR macro-model at (a) 3 km and (b) 5 km point. The result of logarithmic objective function was more sensitive to velocity changes, so the velocities were sometimes over-estimated in high velocity and under-estimated in low-velocity.

The next to original Marmousi model, we experimented with a new synthetic seismic data obtained by increasing the offset and recording time at the same Marmousi velocity model. This data had 641 receivers with 12.5 intervals, so the offset ranges to 8 km long. The offset of the previous seismic data was just about 2.4 km. The recording time was also increased from 2.89 to 8 sec.

The initial velocity models are shown in Figure 4.24. Figure 4.24(a) and (b) were obtained on the new seismic data by performing each the CDR velocity analysis and the Laplace-domain inversion. New Marmousi data with long offset and recording time has more complex seismic signal than previous open seismic data. This complex information gives a difficulty to determine the boundary and the velocity of layers. So, we reduced the number of layers for the velocity analysis even if the overall accuracy falls slightly. The damping constants for the Laplace inversion are used from 2 to 12 with interval of two. The 35^{th} result was chosen as the best velocity model with minimum RMS error.

We inverted the initial models of Figure 4.24 on new seismic data in frequency domain by using logarithmic objective function. The 500^{th} inverted results are shown in Figure 4.25. We can see that two inverted results were improved than Figure 4.19. The velocity structure of the deep part as well as the shallow part was found because of long offset and recording time. Also, Laplace inverted model (Figure 4.25(b)) showed definitely better results than Figure 4.19(b) each in the previous test.

We drew the RMS error curve and depth profile for further analysis. In Figure 4.26, the initial error of the CDR macro-model is greater than of the Laplace inverted model. The error of CDR model decreases rapidly after about 150^{th} iteration, and it becomes smaller than of Laplace model from 315^{th} iteration of amplitude and 319^{th} iteration of phase. Finally, the RMS errors of two inverted models have similar values.

Furthermore, the shape of two depth profile also appears quite similar to approximately 1.5 km depth in Figure 4.27. This means that Laplace inverted model as well as CDR macro-model can produce good result if the seismic data has long offset and recording time. In other words, CDR macro-model has the advantage when we perform frequency domain inversion algorithm on the seismic data with the short offset and recording time.

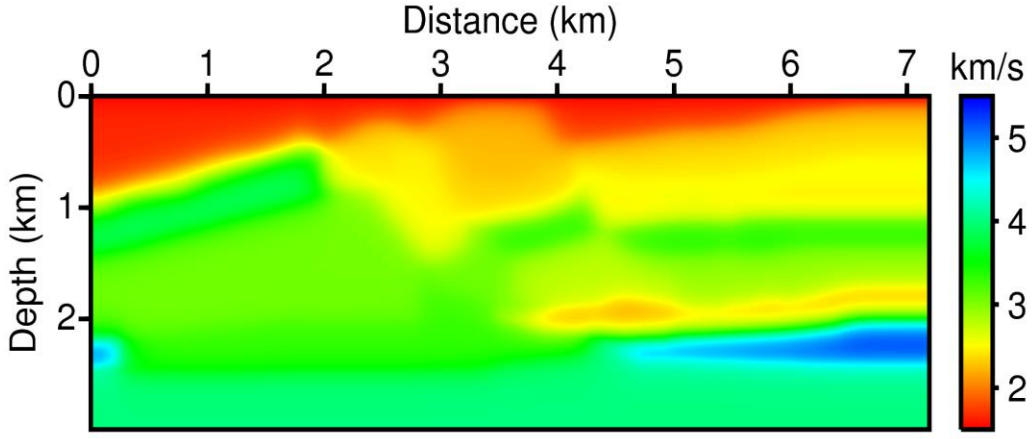

(a)

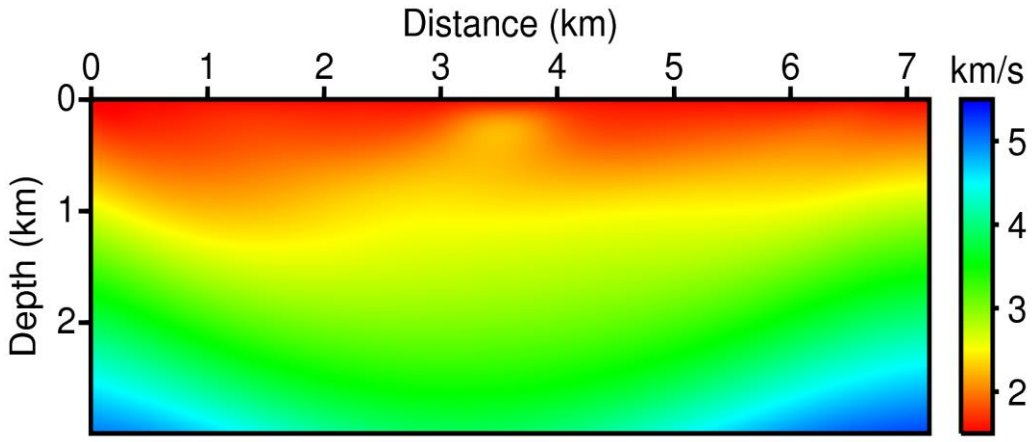

(b)

Figure 4.24. The initial velocity models from (a) the CDR velocity analysis and (b) Laplace-domain inversion. They were obtained on the new seismic data by performing each the CDR velocity analysis and the Laplace-domain inversion.

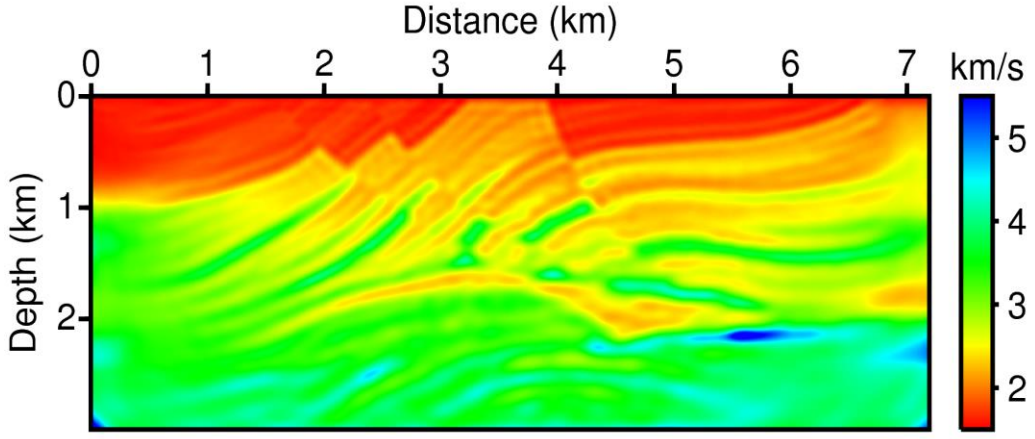

(a)

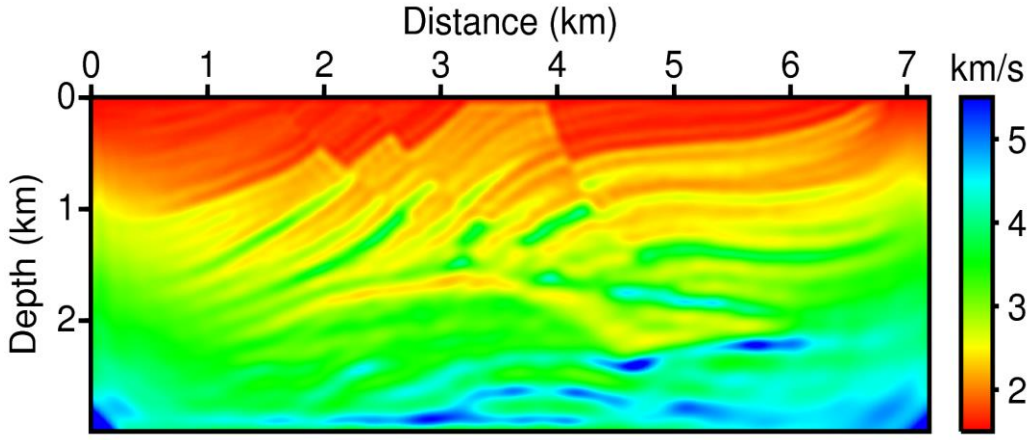

(b)

Figure 4.25. The inverted velocity models with logarithmic objective function and 500th iteration from (a) CDR macro-velocity model and (b) Laplace-domain inverted model.

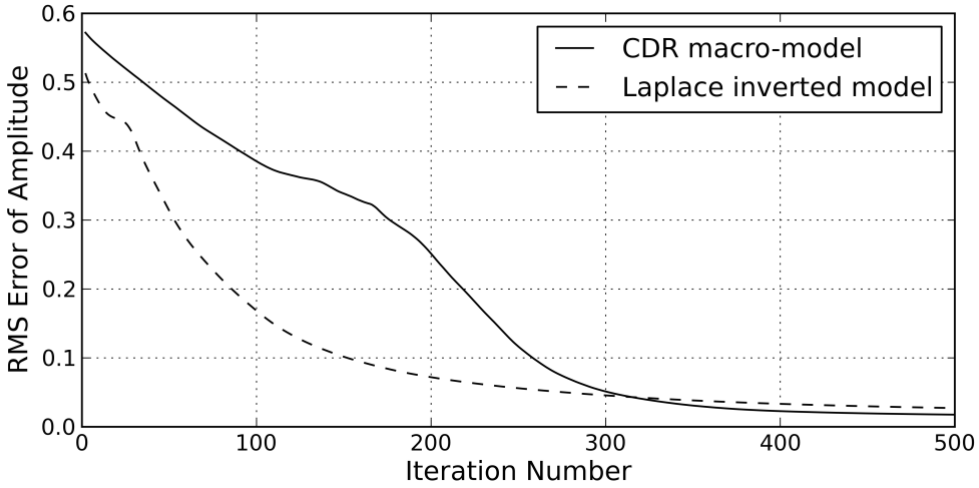

(a)

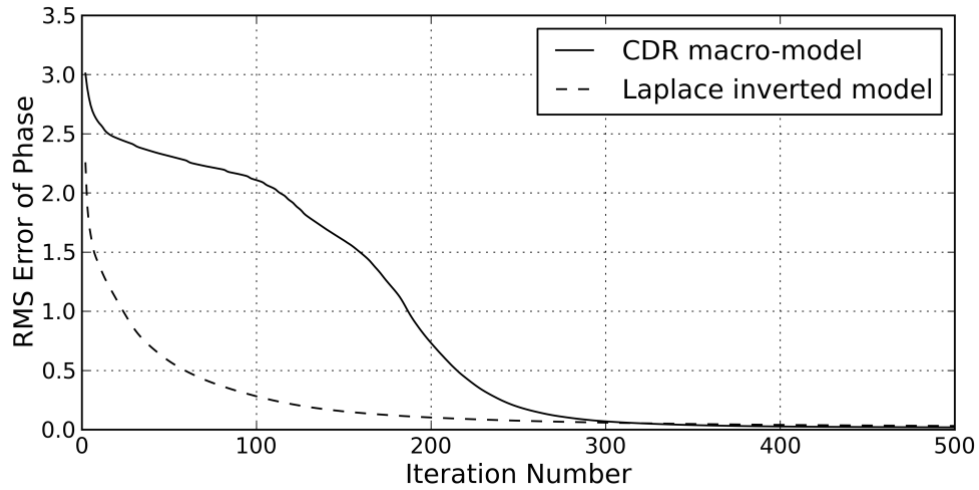

(b)

Figure 4.26. The RMS error curve of (a) amplitude and (b) phase of inverted models on new Marmousi seismic data.

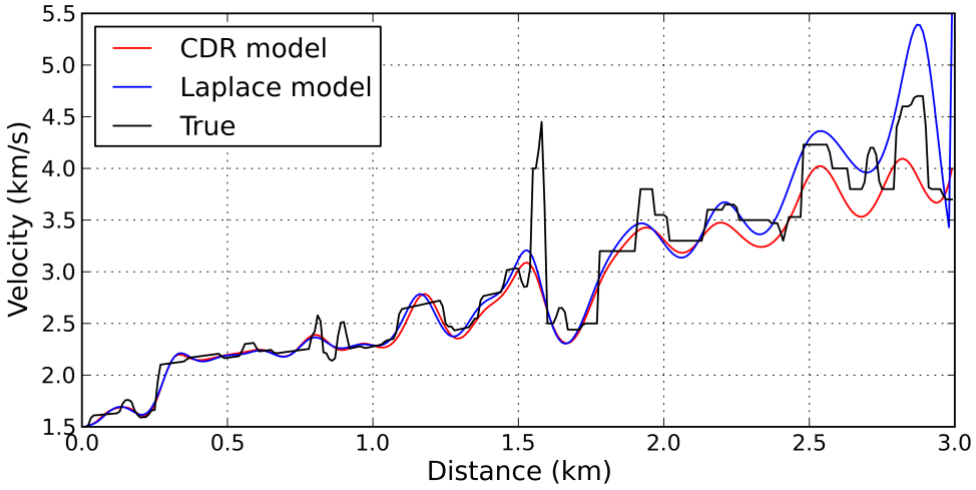

(a)

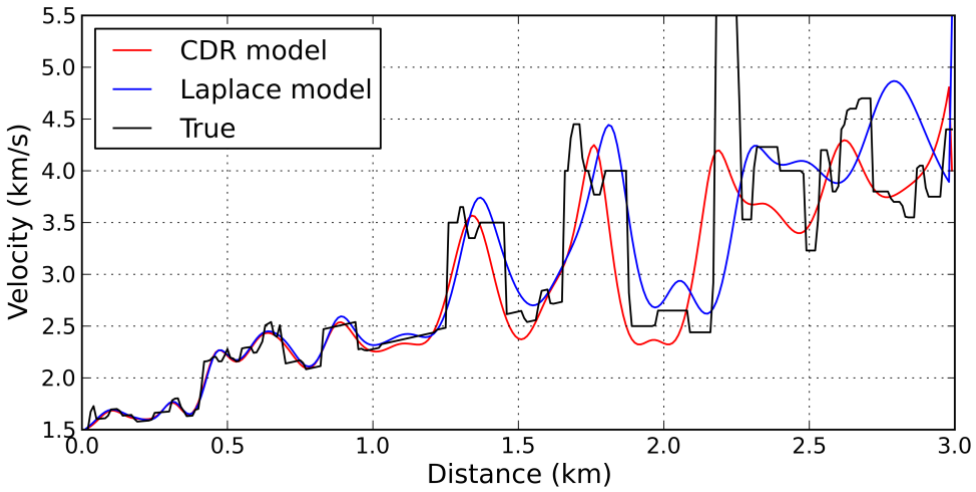

(b)

Figure 4.27. The depth profiles of (a) 3 km and (b) 5 km of inverted models on new Marmousi seismic data.

5. Application to the real data

In this section, it will be explained on real data set test using CDR method. This real seismic data was acquired in Angola, Africa. The 3-demensional exploration is performed about 6000 km^2 area of deep offshore in 2010. It is named after the local place name and called Diaba data. Diaba data sets are consisted of several exploration line data and 08-3 line is selected among them. The data of 08-3 line has total 1,156 shots and we cut 267 shots for the CDR and inversion processing. Since each shot has 804 receivers, the number of total traces is 214,668. Offset ranges from 165 to 10202.5 m and the water depth ranges from 1399.053 to 1653.096 m. The water depth is expressed in Figure 5.1. The sampling time interval is 0.004 sec and total recording time is 12 sec. Figure 5.2 shows the seismogram of the 100^{th} shot. Closing up data to 8 sec is represented in Figure 5.2(b).

5.1 CDR processing

The first necessary thing for applying CDR method is a data binning process. Real seismic data can't have constant interval of shots or receivers unlike synthetic data. However, it is needed to match a constant interval for performing the local slant stack. Because the shot and receiver intervals are roughly adjusted in seismic exploration, the actual error is small within several tens of centimeters. Therefore, we conducted the processing to move the source and receiver points into fixed grid points. The header information of seismic data was arranged before and after binning process in Table 5.1. We can see that the shot point (sx) and receiver point (gx) are changed. By

checking the information of each trace, the regular interval of shot and receiver was confirmed. Figure 5.3 shows the receiver intervals to 50^{th} trace in the first shot gather. The irregular intervals (Figure 5.3(a)) become constant as 12.5 m after binning process (Figure 5.3(b))

A near offset gather was made using receivers closest to shot, namely the offset data of 165 m was used in composing near offset gather. The near offset gather was drawn in Figure 5.4 and it showed to only 6 sec. We can confirm through the near offset gather that the binning process works well because it gathered constant offset point as 165 m. Also, near offset gather represents the overall subsurface structure. It looks the layered structure with folds and faults.

The picked event data was obtained after sorting, stacking and combining process. The detailed description of the processes was omitted because it had already been explained in section 3. Figure 5.5 and 5.6 show picked events corresponding each CSG or CRG. The CSG of Figure 5.5(a) is obtained at 79237.5 km source point and it has 726 traces with 12.5 m spacing. The strong signals are well represented, but weak signals are not appeared in Figure 5.5(b). The CRG of Figure 5.6(a) is obtained at 77685 km receiver point and it has 201 traces with 37.5 m interval. So, the resolution of CRG image is lower than CSG image. The low resolution increases the probability to generate a misfit like a red dotted circle parts. However, this misfit problem will be solved when the CSG and CRG data are combined. Other problem is that the direct wave signal didn't pick at both gathers. It can be solved to some extent by using the water depth data

obtained during the seismic exploration.

Figure 5.7 is a process for determining layer boundaries by using migrated image as background image. After obtaining the last layer, it was smoothed for FWI. A damped least squares technique was used with the damping parameter 10. The completed initial velocity model is same with Figure 5.8(a).

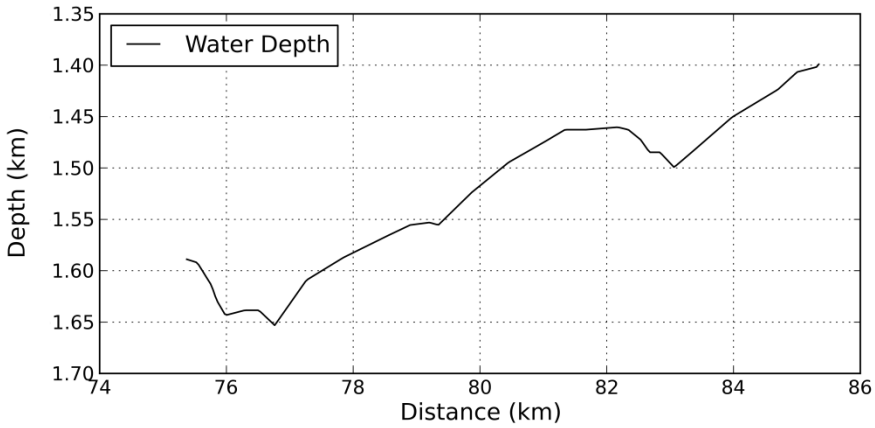

Figure 5.1. Sea water depth of Diaba seismic data set. The water depth ranges from 1399.053 to 1653.096 m in deep offshore area.

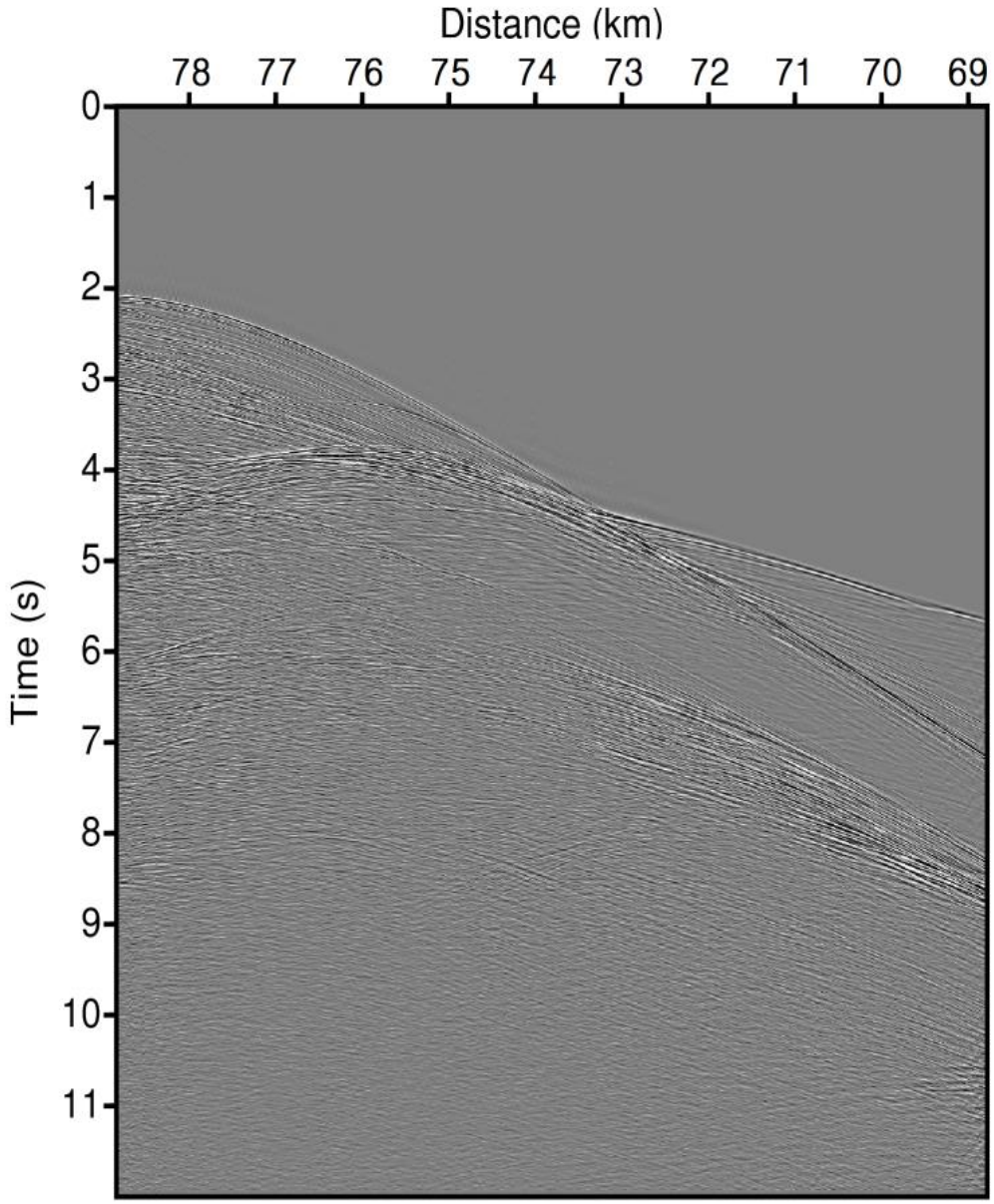

(a)

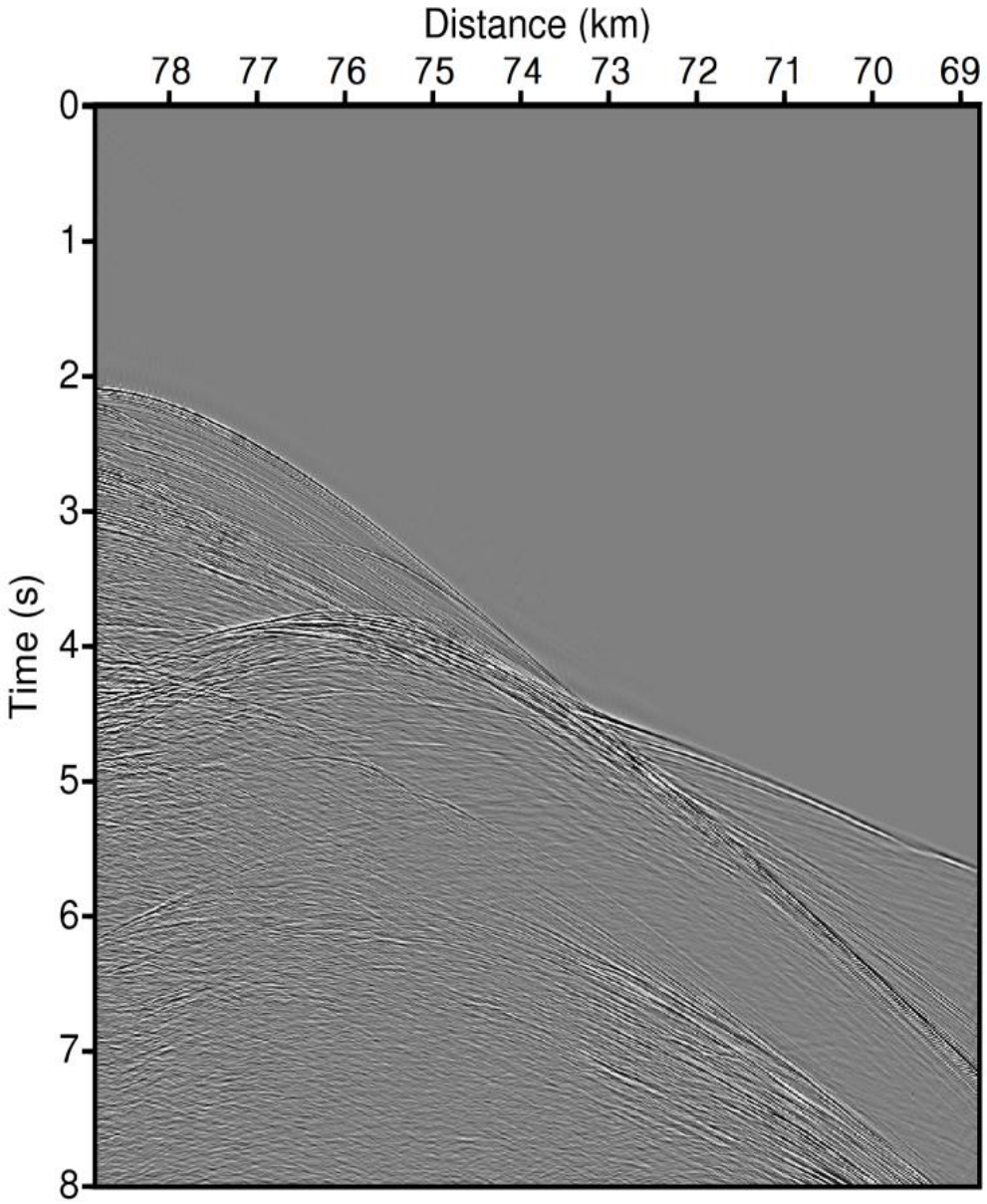

(b)

Figure 5.2. The 100th Shot gather of Diaba seismic dataset to (a) 12 sec and (b) 8 sec.

	Header before binning	Header after binning
tracl	1 - 214668	1 - 214668
fldr	1001 - 1266	1001 - 1267
tracf	1 - 804	1 - 804
offset	16500 - 1020250	16500 - 1020250
scalco	-100	-100
sx	7537455 - 8534533	7537500 - 8535000
gx	6516104 - 8517993	6517250 - 8518500
ns	3000	3000
dt	4000	4000

Table 5.1. The header information of Diaba seismic data before and after binning process. The shot point (sx) and receiver point (gx) are changed.

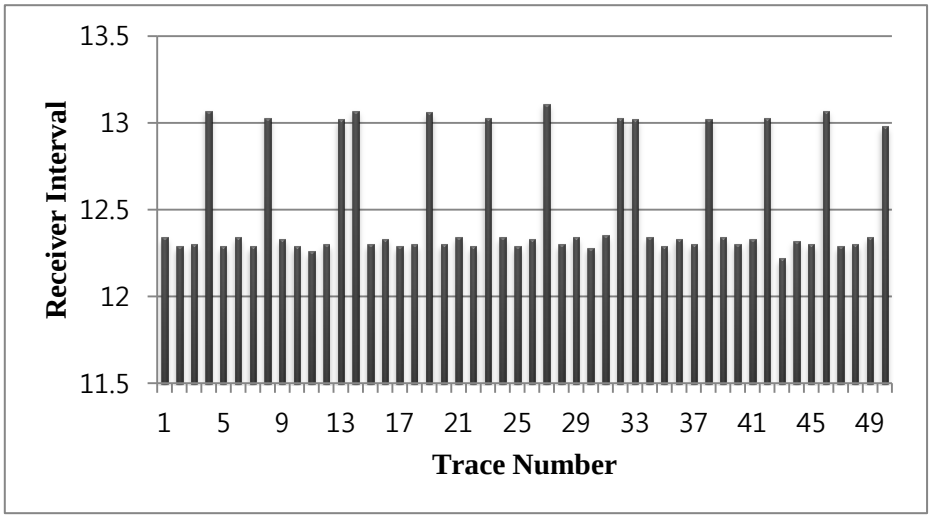

(a)

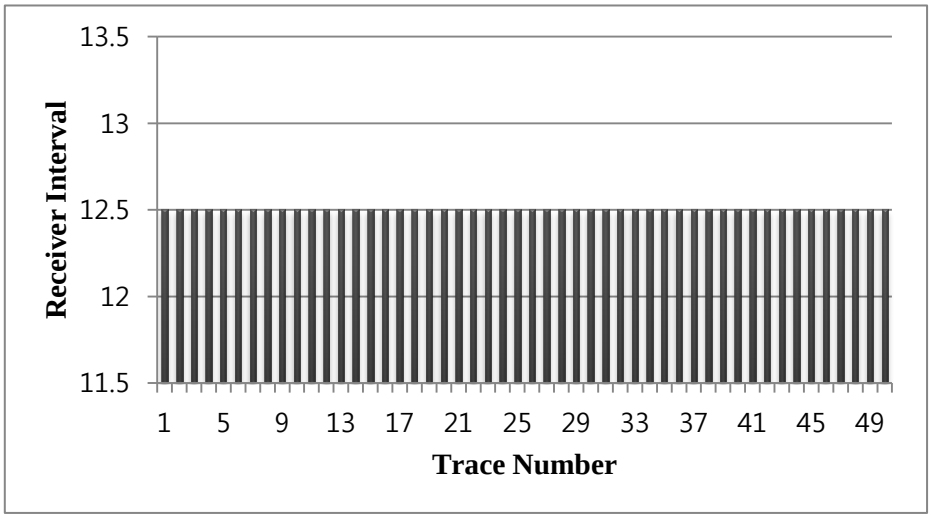

(b)

Figure 5.3. The receiver interval to 50th trace in the first shot gather (a) before and (b) after binning. After binning, the receiver interval becomes constant.

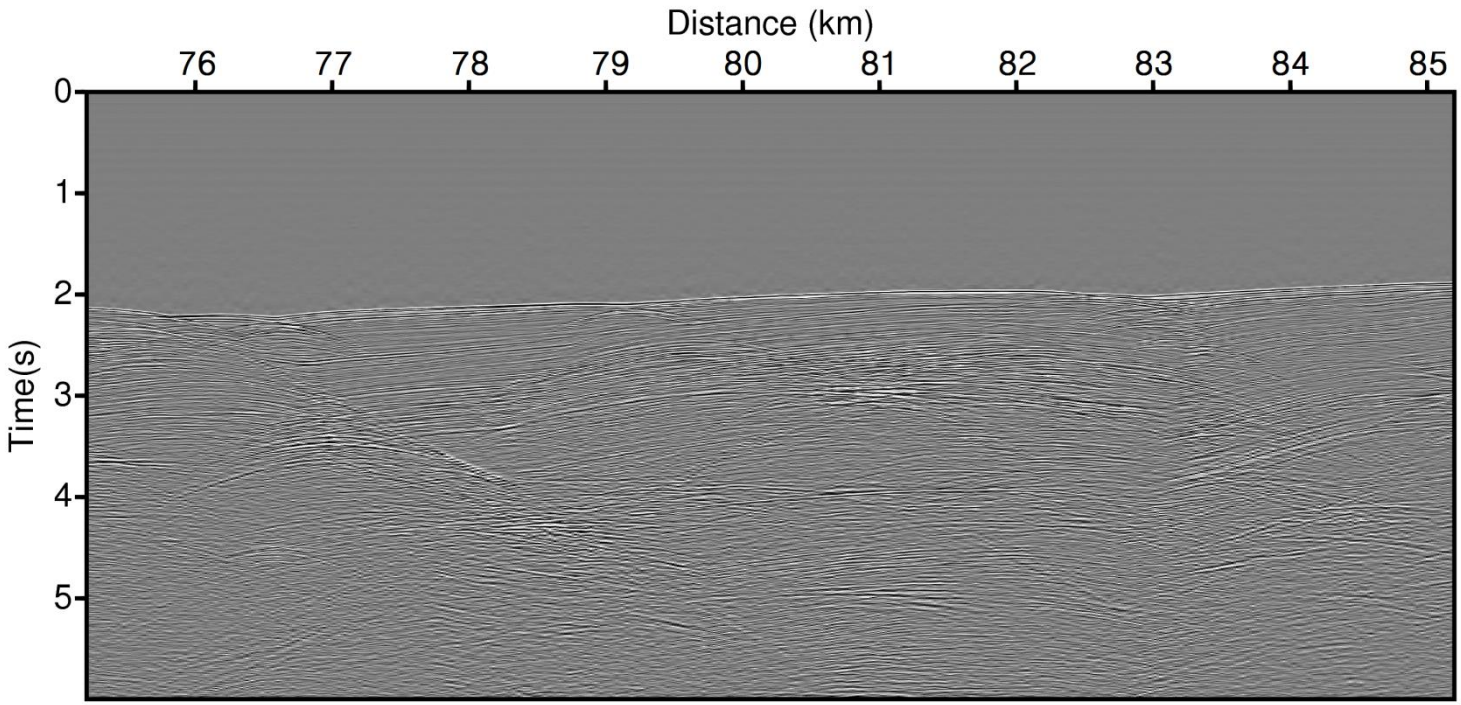

Figure 5.4. Near offset gather of first offset (135m). It shows that the binning process works well because it gathered constant offset point. Also, it represents the overall subsurface structure.

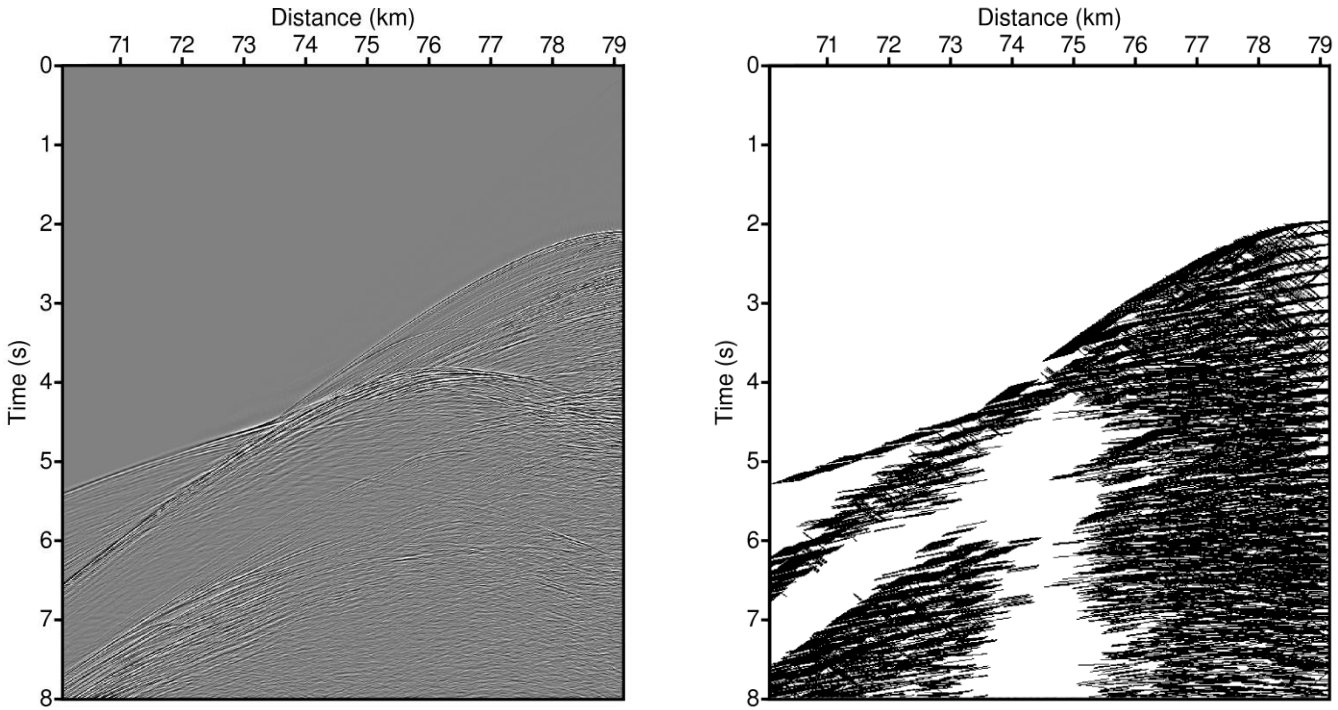

(a) (b)

Figure 5.5. (a) The CSG of sx=79237.5 km and (b) its picked events. The strong signals are well represented, but weak signals are not appeared.

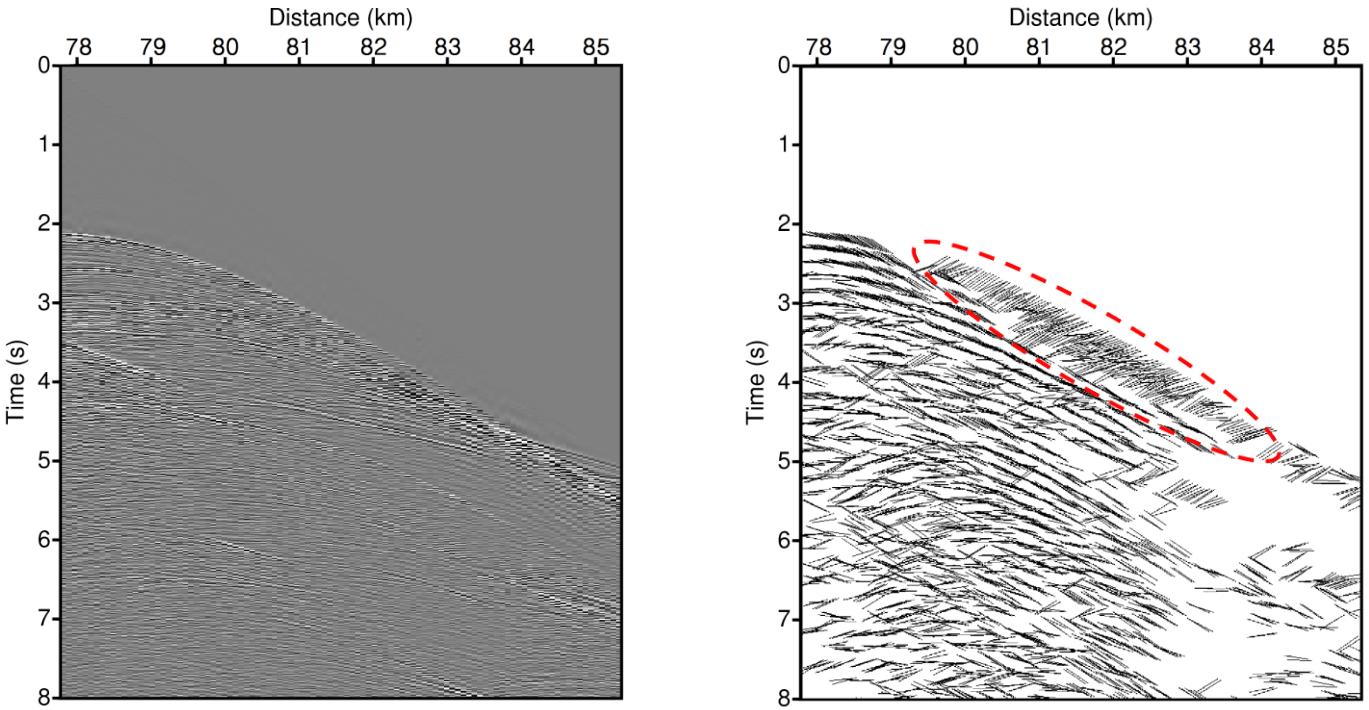

(a) (b)

Figure 5.6. (a) The CRG of gx=77685 km (b) its picked events. The low resolution of CRG increases the probability to generate a misfit like a red circle part. However, this problem will be solved when the CSG and CRG data are combined.

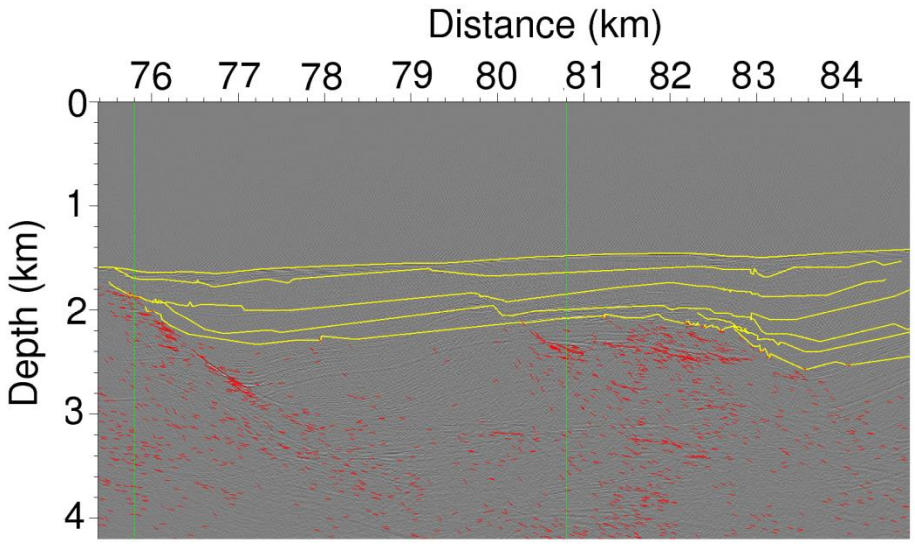

(a)

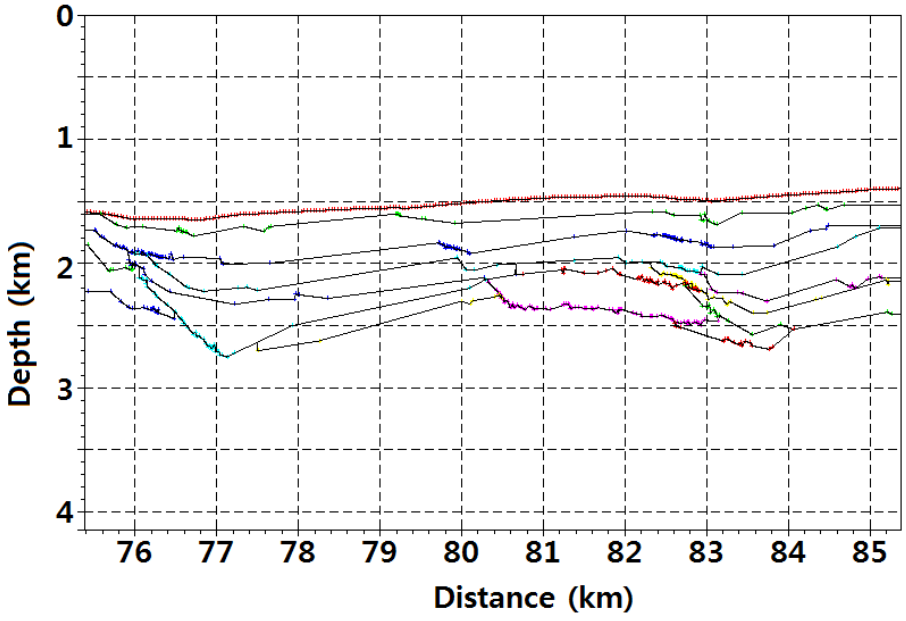

(b)

Figure 5.7. The processing of determining layer boundaries by using migrated image as background image. (a) A boundary selecting panel. The red points are reflection point within a specified velocity range and yellow

lines indicate determined layer boundaries. The green vertical lines represent the horizontal range for velocity analysis. (b) The model generating panel. The line followed by red dots on top represents the seafloor boundary. Selected layers and velocities are allocated on the gird.

5.2 FWI & migration results

We performed FWI using CDR macro-model and Laplace-inverted model as initial model (Figure 5.8). Laplace inverted model (Figure 5.8(b)) was used six damping constants from 3 to 13 and 30^{th} result was selected as initial model. The model size for inversion is 1038 x 400 with 12.5 m grid. 267 shots were used with 37.5 m intervals and frequency was used from 3.0 to 13.44 with 0.36 intervals.

The inverted result is shown in Figure 5.9. Figure 5.9(a) shows the velocity structure well than Figure 5.9(b). To 3 or 4 km depth, it is estimated at low velocity of approximately from 1.7 to 2.3 km/s, which is similar to the p-wave velocity of the sedimentary rock (Table 5.2). In fact, under the seafloor of the exploration area in Angola is mainly covered by shale and sandstone to several kilometers and the salt layer appears under it. We cannot know whether it is salt layer in deeper part because both inverted results didn't appear it.

For comparison, we drew the RMS error of amplitude and phase as iteration number (Figure 5.10). In the phase RMS error in Figure 5.10(b), the error of CDR macro-model is smaller than that of Laplace inverted model except for first 20 iterations. We can't know true velocity model of real seismic dataset, so it is difficult to compare inverted results directly. Therefore, we used migration scheme for checking the inversion results.

The migrated images generated from the velocity models in Figure 5.9 are shown in Figure 5.11. We use the simple Kirchhoff migration algorithm.

Figure 5.11(a) shows subsurface structures such as fault and layer in the shallow depth. In order to verify the accuracy of the velocity models and the migrated images, we make the common image gathers (CIGs) in the offset domain. While the migrated images are obtained by overlapping images of all shot points, CIGs are obtained by horizontally arraying images of a specific point. Therefore, CIGs should have flat structures theoretically if the estimated velocity is exact. Figure 5.12 shows the CIGs obtained from 180^{th}, 430^{th} and 680^{th} offset. The CIGs of the first group (Figure 5.12 (a)-(c)) is obtained using the inverted velocity model of the CDR macro model and the second group (Figure 5.12 (d)-(f)) are made from Laplace model. The CIGs of the first group are more flat than second group. Therefore, we can confirm that the CDR macro-model can be applied to field dataset.

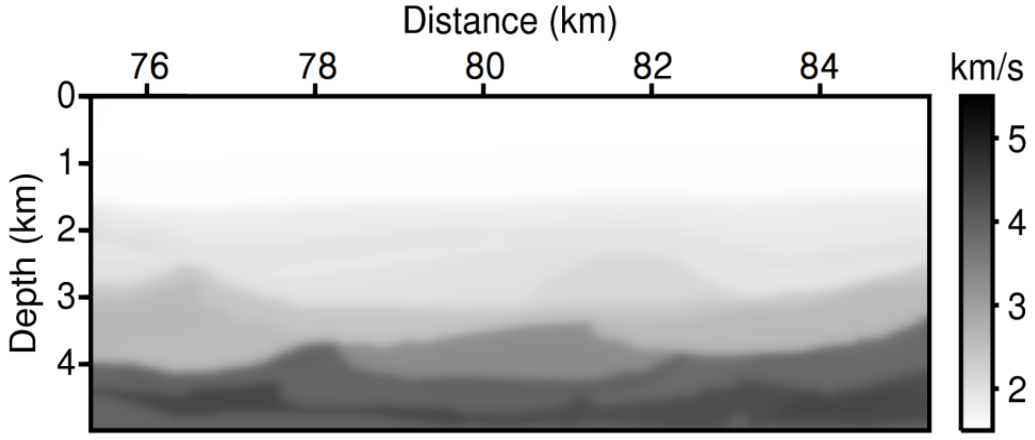

(a)

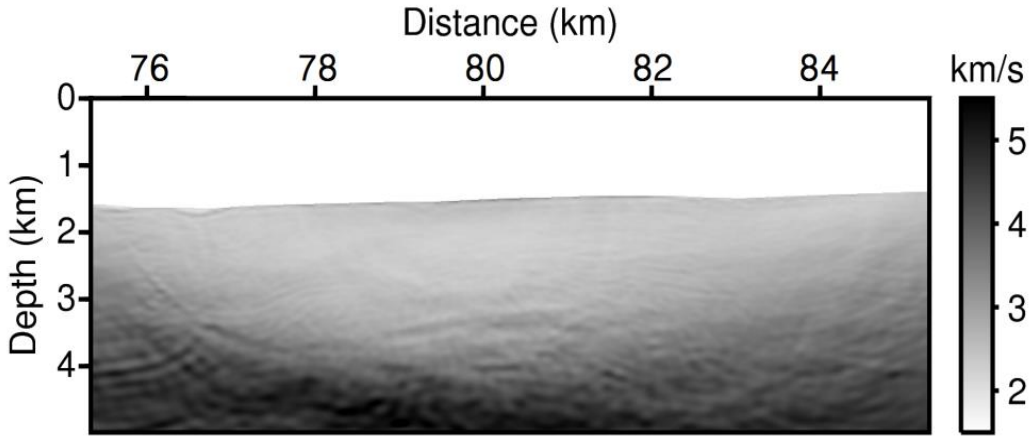

(b)

Figure 5.8. Initial velocity model of Diaba real data set for FWI using (a) CDR macro-model and (b) Laplace inverted model. The Laplace inverted model was used six damping constants from 3 to 13 and 30th result was selected as initial model.

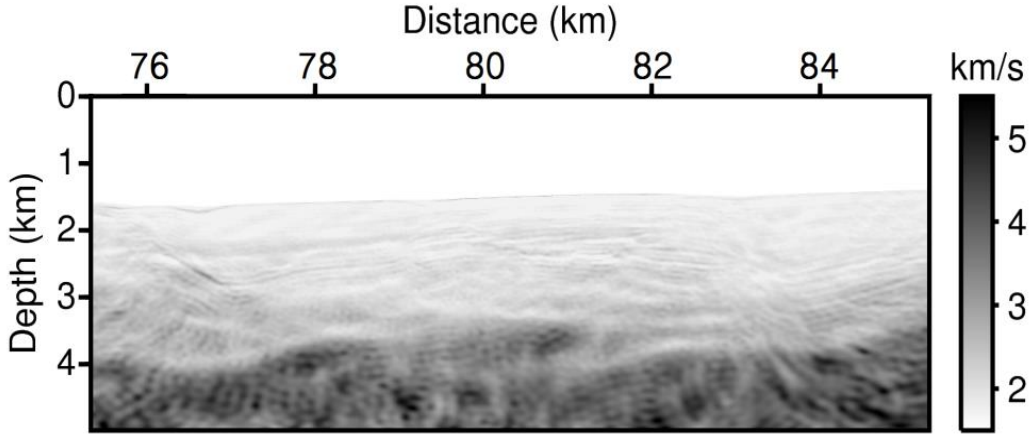

(a)

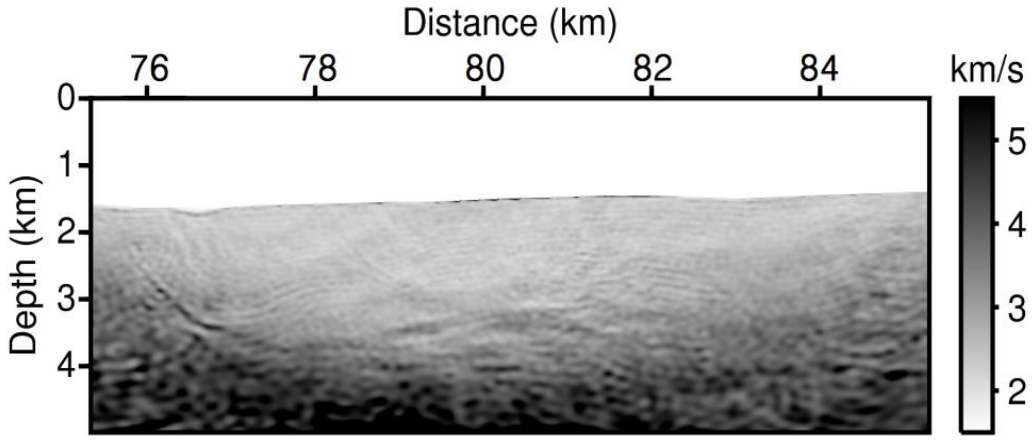

(b)

Figure 5.9. Inverted velocity model of the Diaba real data set using (a) CDR macro-model and (b) Laplace inverted model. The CDR model shows the velocity structure better than the Laplace model.

	P-wave velocity (m/s)	S-wave velocity (m/s)
Shale	2,123	1,469
Siltstone	2,318	1,523
Limestone	2,750 - 3,632	1,718 - 2,319
Quartzite	4,964	3,274
Sandstone	2,487	1,701
Slate	4,336	2,859
Schist	4,679 - 5,289	2,920 - 3,239
Gneiss	3,188	2,052
Marble	3,642 - 5,587	2,355 - 3,316
Granite	3,692 - 3,967	2,468 - 2,722
Gabbro	5,042	3,202
Diabase	6,569	3,681
Basalt	5,123	3,069
Andesite	4,776	2,983
Tuff	996	659

Table 5.2. The seismic velocity of the common rocks. Generally sedimentary rocks have a lower velocity than igneous and metamorphic rocks.

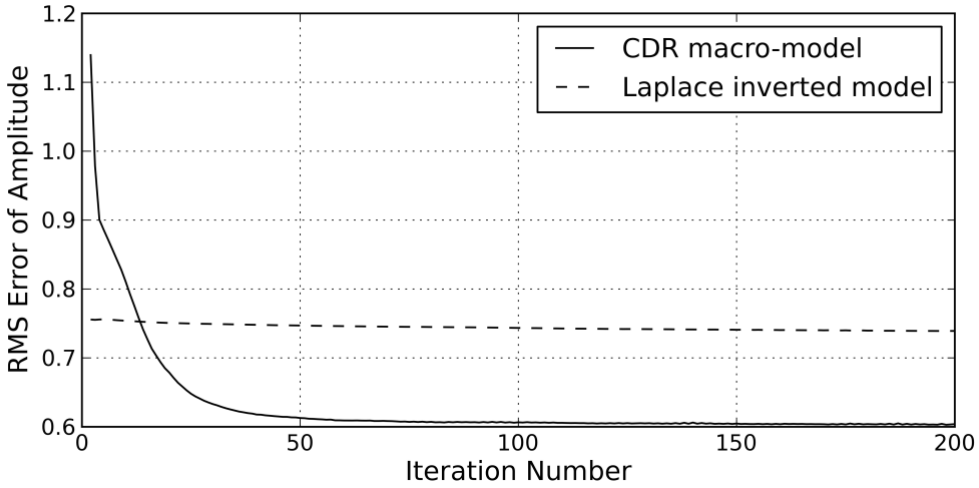

(a)

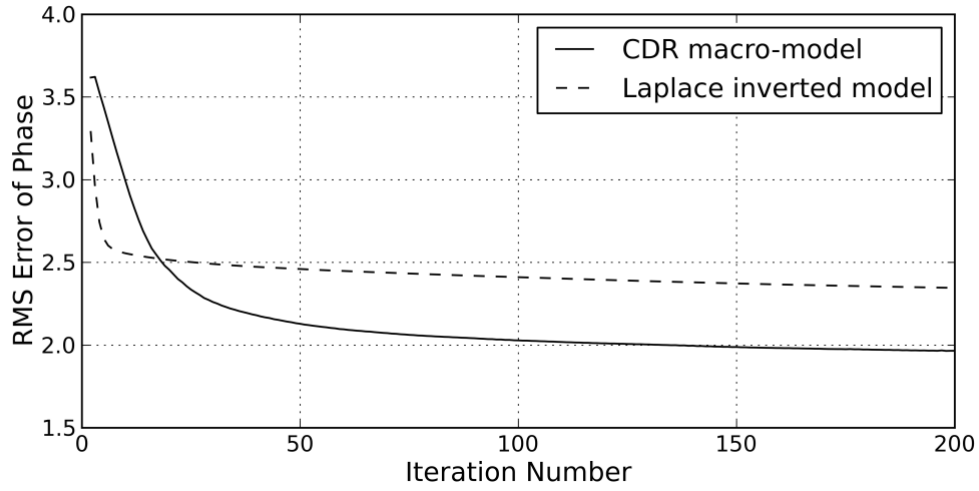

(b)

Figure 5.10. The RMS error curve at iteration number of (a) amplitude and (b) phase. The errors of CDR macro-model are smaller than that of Laplace inverted model except for first 20 iterations.

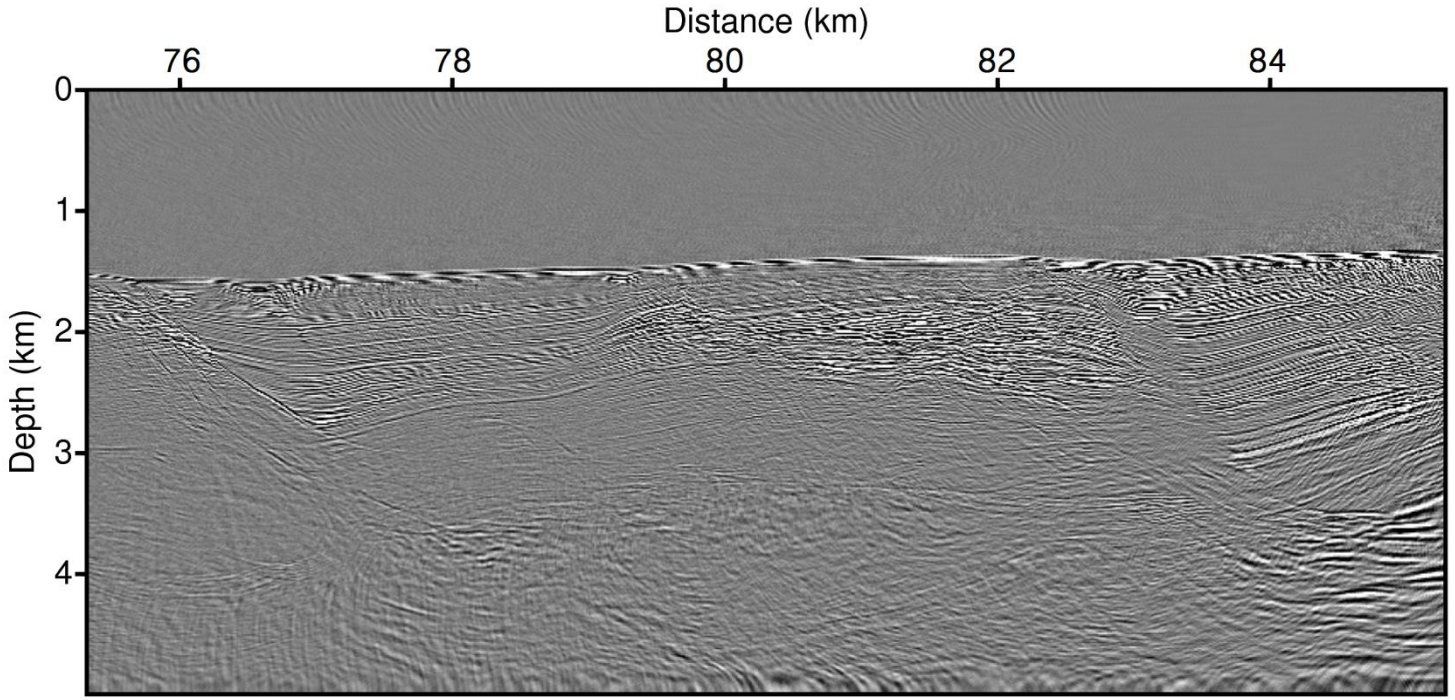

(a)

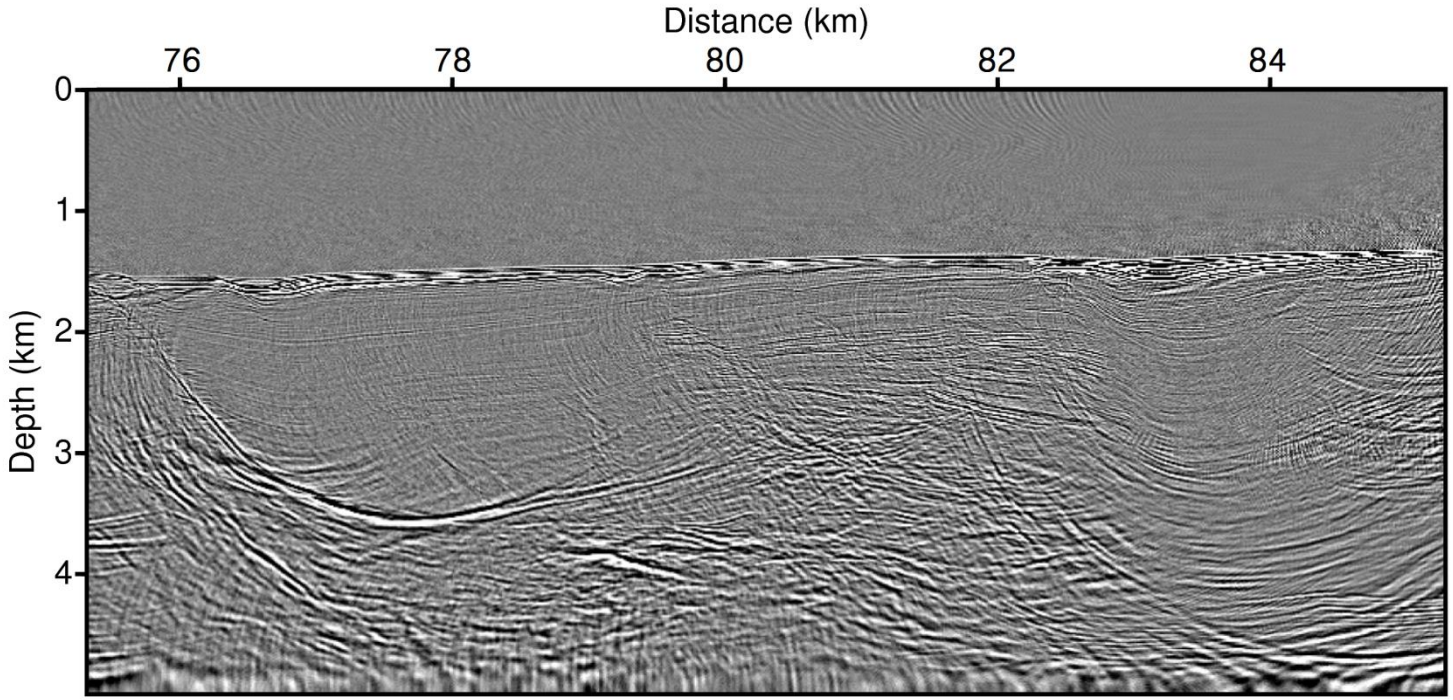

(b)

Figure 5.11. The Kirchhoff migrated results from (a) Figure 5.9 (a) and (b) Figure 5.9 (b).

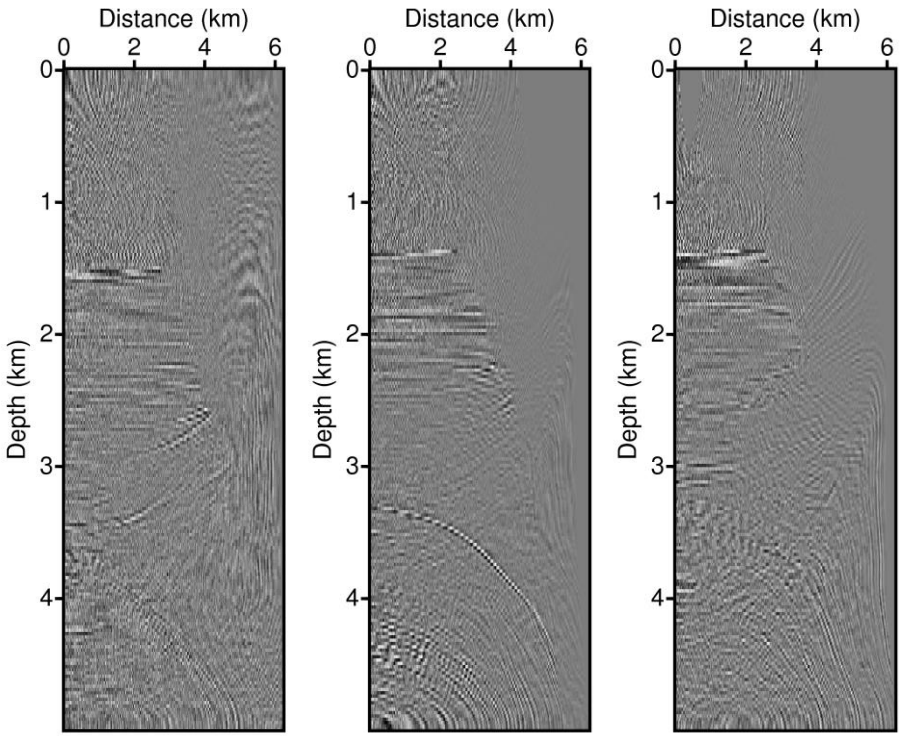

(a) (b) (c)

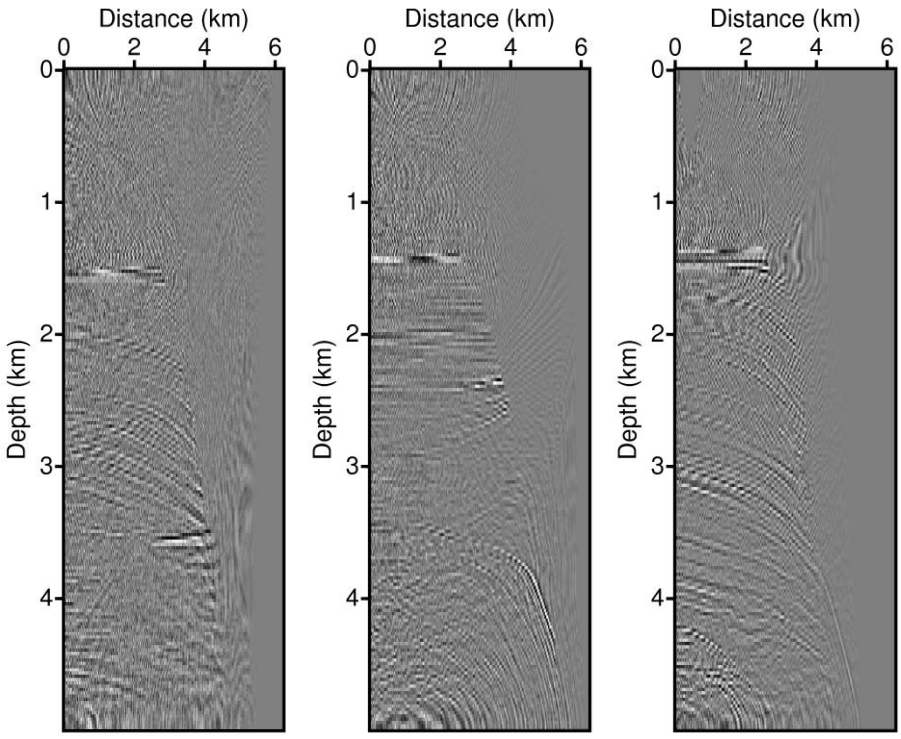

(d) (e) (f)

Figure 5.12. The CIGs obtained from 180th ((a) and (d)), 430th ((b) and (e)) and 680th ((c) and (f)) offset. (a)-(c) are obtained from Figure 5.11(a) and (d)-(f) are obtained from Figure 5.11(b). The CIGs of (a)-(c) are more flat than (d)-(f).

6. Discussion & Interpretation

6.1 Improvement of strip-off CDR method

In this paper, we used the strip-off CDR method for constructing initial velocity model. Some improvements are made while using the conventional method. First, we used the shot and receiver selectively to increase the resolution of the CRG. Because most seismic data has small number and wide spatial interval of shots, it may cause problems of low resolution of CRG in the local slant stack. The information of CSG and CSG used in the Overthrust model of this paper are shown in Table 6.1. Because the trace interval of the CRG is twice longer than the CSG, more CSG seismograms are selected in wider range. As a result, the total number of effective traces used for analysis is almost same each other, and the difference is smaller than 1%.

Also, we performed the local slant stack and the ray parameter picking at the same time for saving computation time and storage. The computation time and storage is represented in Table 6.2 comparing to the conventional separated method. The Overthrust and Marmousi seismic data was used for calculation. As shown in Table 6.3, local slant stack takes up huge computer storage capacity as well as consumes a lot of time. Therefore, we can reduce the computing time and storage by calculating ray parameters immediately after the local slant stack. The computing time decreased by only about 2 % than conventional method. It didn’t save much computing time because we cannot reduce the calculation amount for obtaining same result. We can only save the time to write and read the result of LSS. However, the storage

capacity was greatly reduced to more than 99 % than conventional method. This was possible because we don’t need to store separately the LSS results which occupy a lot of computer memory.

Finally, we can increase accuracy when determining boundary of velocity model by using migrated image as back ground image. Also, we introduced the binning process for applicability to the real seismic data.

	CSG	CRG
Range	4.8 - 15.25 km	3.5 - 16.55 km
Trace interval	25	50
No. of Seismogram	210	523
No. of trace per a seismogram	331	60 - 168
No. of total trace	69510	63240

Table 6.1. The information of CSG and CSG used in the Overthrust model of this paper. More CSG seismograms are selected in wider range, so the total number of effective traces used for analysis becomes similar.

		Present method	Conventional method		Saving (%)
			LSS	Picking	
Computing time (sec)	Overthrust	637	590	59	1.85
			649		
	Marmousi	496	462	43	1.78
			505		
Storage (Mb)	Overthrust	57	7,952	46	99.29
			7,998		
	Marmousi	35	6,209	28	99.44
			6237		

Table 6.2. The computation time and storage of the local slant stack and the ray parameter picking in the Ovethrust and Marmousi model.

6.2 Model-generation time and accuracy

In this section, we compared the model-generating time and accuracy of three models of Overthrust and Marmousi seismic data. The each model-generating time for three initial models is shown in Table 6.3(a). Generating CDR model takes more than 10 times longer than the Laplace model. One of the reasons why computing time shows big difference is parallel computation. Laplace domain inversion can greatly reduce the computing time by using many computer cores because it is possible to parallelize the calculation. In contrary, only one core is used in calculating CDR process because this method is not parallelized. The strip-off CDR method is difficult to parallelize because it is sequential process. Also, the CDR velocity analysis is a semi-automatic technology, so it requires the involvement of people in the middle process. The computing time shown in Table 6.3(a) indicates a running time of algorithm. Therefore, the total model-generating time can be increased depending on the researcher's proficiency.

In order to compare the entire model-generation time, it should be also considered pre-processing time. The pre-processing of the CDR velocity analysis method contains sorting, local slant stack, picking and combining process. In this step, it is possible to make automatic algorithm as well as parallelized algorithm. If we create automatic parallelized algorithm, it is expected to significantly reduce time especially local slant stack. The Laplace domain FWI doesn’t require pre-processing in synthetic data. However, the Laplace inversion on the field data spends a lot of time for pre-processing such as filtering and muting. Thus the difference in the total model-generating

time can be reduced in the field data application.

The reason for using the CDR velocity analysis is due accuracy despite the calculating time takes longer. Table 6.3(b) shows the RMS error of initial and inverted models of Overthrust and Marmousi data with logarithmic objective function. The initial error of the amplitude is the smallest in the linearly increasing model, but after inversion the CDR model has the smallest error value. We can see that good initial velocity model helps to find the true velocity value well although the initial error is a little higher. Also, the CDR velocity model shows good results particularly in the phase error. The initial phase error is the smallest among three models and it shows a large decline until final error. In Overthrust model, the phase error of CDR model decreased more than 90 %. In sum, the RMS error of inverted CDR model is 1.2 to 6 times smaller than other models.

Even though fast computational time is important, it is also worth if we can get a more accurate velocity model. In particular, it is expected to give good results in difficult data to raise the accuracy from the conventional method such as seismic data with weathered zone or short offset. Also, the CDR velocity analysis may be useful to work to favor higher accuracy than fast calculation time such as some resource exploration and geological survey. In the large-scale and long-term seismic exploration, sending a few hours or days for generating the initial model doesn't often have significant impact on the overall operation. Furthermore, the good initial model can reduce the computing time for inversion as well as increase the accuracy of inverted results. When comparing the computing time until the same error level, the

better initial model has shorter time. The time difference according to the iteration is not large in the seismic data used in this paper because they are 2D data of a relatively small capacity. However, it will be reduced a lot of time in huge seismic data or 3D data.

Also, the advantage of this method is that it can adjust the accuracy and computation time. For instance, if you want to get a broad velocity model over wide area, the computing time can be saved by reducing the number of layers to analyze even accuracy falls a little.

		Pre-processing (min)	Generating velocity model		
			No. of core	Iteration	time (min)
Overthrust	CDR	28	1	23	120
	Lap.	0	6	42	12
	L.I.M	0	1	1	0.2
Marmousi	CDR	23	1	27	140
	Lap.	0	6	30	3
	L.I.M	0	1	1	0.1

(a)

		RMS error			
		Amplitude		Phase	
		initial	final	initial	final
Overthrust	CDR	1.082301	0.2501483	2.913549	0.215743
	Lap.	1.553560	0.4489022	3.287612	1.183911
	L.I.M	1.050048	0.4535103	3.224056	1.283367
Marmousi	CDR	1.084371	0.5341002	3.091920	1.116534
	Lap.	1.381475	0.6526318	3.419335	1.536899
	L.I.M	0.791415	0.7133400	3.318063	1.888043

(b)

Table 6.3. (a) The pre-processing and model-generating time for three initial models and (b) the RMS error of the initial and inverted models in the Overthrust and Marmousi data.

6.3 Discussion on FWI results

We can use two realistic synthetic data sets and a real seismic data for inversion test. It will be briefly discussed by synthesize their results.

First, the overthrust synthetic model was used, which this seismic data has very short recording time, complex structure and weathered layer. Despite of these problems, the CDR macro-model was inverted with good velocity structure. For comparison, we tested the velocity model with top fixed layer. In the top fixed model, the Laplace model showed an improved inversion result than previous open data. However, the CDR macro-model appeared good inverted results regardless of fixed layer. This demonstrates the CDR macro-model has strength to seismic data with weathered layer. Also, in other Overthrust model test, we confirmed applicability on multi-parameter inversion of the CDR macro-model from these results.

The second synthetic data was Marmousi model that has very short offset and recording time. The CDR macro-model showed good inverted result at shallow part even though deep depths didn't find well because of short offset. In order to confirm the effects on FWI of offset length, we made seismic data with long offset. In this test, the Laplace inverted model as well as the CDR macro-model showed good results. The Laplace model didn't invert well in the seismic data with short offset. This means that the CDR macro-model is less sensitive on offset length of seismic data. In other word, the CDR macro-model has the advantage for short offset data.

Finally, we performed real data test on Diaba seismic data. Although we can't know true velocity model about real seismic data, we confirm that the RMS error of the CDR model is less values than Laplace inverted model. The migrated images and CIGs also proved that the inverted CDR model shows good result.

7. Conclusion

In this paper, we explained the process of constructing velocity model with strip-off CDR method and performed FWI by using this obtained model as initial model. Ii is significant that the CDR model is first applied as the initial model of FWI. Also, we confirm good inverted results from two realistic synthetic data sets and a real seismic data test, when compared with the results using conventional Laplace inverted model and linearly increasing model.

When compared to the conventional CDR method, the strip-off CDR velocity analysis increased the resolution of CRG and reduced computer storage space dramatically. Also, it could improve the accuracy of the velocity model by using the migrated image as background panel during velocity analysis.

The strip-off CDR velocity analysis is disadvantageous in the computing time than the Laplace domain inversion. However, the development of automatic and parallelized algorithm in pre-processing is expected to reduce the computation cost. Even if the computation time is greater, it has great value in the high accuracy.

In conclusion, the macro-model by obtained from the CDR strip-off method is suitable for frequency domain FWI. As increasing the exploration in complex terrain or as 3-dimensional geometry, it is expected to generate to seismic data with short offset or recording time. In this case this method will

be a good solution for building initial model of FWI. Furthermore, it can be also expected to applying into land or OBS seismic data and extending into other inversion field such as multi-parameter inversion.

Reference

Al-Yahya K. 1989. Velocity analysis by iterative profile migration. *Geophysics* 54, No. 6, 718-729.

Bae H.S., Shin C., Cha Y.H., Choi Y. and Min D.J. 2010. 2D acoustic-elastic coupled waveform inversion in the Laplace domain. *Geophysical Prospecting* 58, 997-1010.

Bagaini C. 2008. Low-frequency vibroseis data with maximum displacement sweeps. *The Leading Edge*, 27(5), 582-591.

Ben-Hadj-Ali H., Operto S. and Virieux J. 2011. An efficient frequency-domain full waveform inversion method using simultaneous encoded sources. *Geophysics*, Vol. 76, No. 4, pp. R109-R124.

Billette F. and Lambaré G. 1998. Velocity macro-model estimation from seismic reflection data by stereotomography. *Geophys. J. Internat*., Vol. 135, No. 2, pp. 671-680.

Biondi B. 1990. Seismic velocity estimation by beam stack, PhD thesis. Stanford University, USA.

Biondi B. 1992. Velocity estimation by beam stack. *Geophysics*, Vol. 57, No. 8, pp. 1034-1047.

Bunks C., F.M. Saleck, S. Zaleski and G. Chavent. 1995. Multiscale seismic waveform inversion. *Geophysics* 60, 1457−1473.

Cha Y.H. and Shin C. 2010. Two-dimensional Laplace-domain waveform inversion using adaptive meshes: and experience of the 2004 BP

velocity-analysis benchmark data set. *Geophysical Journal International* 182, 865-879.

Chauris H., Noble M. and Taillandier C. 2008. What initial velocity model do we need for full waveform inversion? *70th EAGE Conference & Exhibition*, Italy.

Choi Y., Shin C. and Lee S. 2014. Development of the Strip-off CDR Veloicty Analysis for a Constant Velocity Macro-model. *J. Korean Soc. Miner. Energy Resour. Eng.* 51, No.2, 178-192.

Doherty S. and Claerbout J. 1976. Structure independent velocity estimation. *Geophysics*, Vol. 41, No. 5, 850-881.

Gao Z., Pan Z., Gao J. and Zhang X. 2014. Building an Initial Model for Full Waveform Inversion Using a Global Optimization Scheme. *SEG Denver 2014 Annual Meeting*, USA.

Geller R.J. and T. Hara. 1993. Two efficient algorithms for iterative linearized inversion of seismic waveform data. *Geophysical Journal International* 115, 699−710.

Ha W., Chung W., Park E. and Shin C. 2012. 2-D acoustic Laplace-domain waveform inversion of marine field data. *Geophys. J. Int.*, 190, 421–428.

Ha W., Pyun S., Yoo J. and Shin C. 2010. Acoustic full waveform inversion of synthetic land and marine data in the Laplace domain. *Geophysical Prospecting*, 58, 1033–1047.

Lailly P. 1983. The seismic inverse problem as a sequence of before stack migrations. In: *Conference on Inverse Scattering: Theory and Application* (eds J.B. Bednar, R. Redner, E. Robinson and A. Weglein). SIAM.

Levenberg K. 1944. A Method for the Solution of Certain Non-Linear Problems in Least Squares. *Quarterly of Applied Mathematics* 2, 164–168.

Liu Z. and Bleistein N. 1995. Migration velocity analysis: theory and an iterative algorithm. *Geophysics* 60, No. 1, 142-153.

MacKay S. and Abma R. 1992. Imaging and velocity estimation with depth-focusing analysis. Geophysics 57, No. 12, 1608-1622.

Marquardt D. 1963. An Algorithm for Least-Squares Estimation of Nonlinear Parameters. *SIAM Journal on Applied Mathematics* 11, No. 2, 431–441.

Meier M., Lewallen K., Otero J., Heiney S. and Murray T. 2015. Low Frequency Seismic Acquisition Innovations Approaching One Hertz. *Offshore Technology Conference*, 04-07 May, Houston, Texas, USA

Moldoveanu N., Combee L., Egan M., HAampson G., Sydora L. and Abriel W. 2007. Over/under towed-streamer acquisition: A method to extend seismic bandwidth to both higher and lower frequencies. *The Leading Edge*.

Operto S., Ravaut C., Improta L., Virieux J., Herrero A. and Dell'Aversana P. 2004. Quantitative imaging of complex structures from dense wide-aperture seismic data by multiscale traveltime and waveform inversions: A case study. *Geophysical Prospecting* 52, 625−651.

Operto, S., Virieux J., Dessa J.X. and Pascal G. 2006. Crustal seismic imaging from multifold ocean bottom seismometer data by frequency domain full waveform tomography: Application to the eastern Nankai trough. *Journal of Geophysical Research*, 111, B09306.

Park E., Ha W., Chung W., Shin C. and Min D.J. 2013. 2D Laplace-Domain Waveform Inversion of Field Data Using a Power Objective Function. *Pure Appl. Geophysics* 170, 2075−2085.

Pratt R.G. 1999. Seismic waveform inversion in frequency domain—Part 1: Theory and verification in physical scale model. *Geophysics* 64, 888−901.

Pratt R.G., Shin C. and Hicks G.J. 1998. Gauss-Newton and full Newton methods in frequency-space seismic waveform inversion. *Geophysical Journal International* 133, 341−362.

Prieux V., Lambar´e G., Operto S. and Virieux J. 2012. Building starting models for full waveform inversion from wide-aperture data by stereotomography. *Geophysical Prospecting*, 1−29.

Pyun S., Son W. and Shin C. 2011. 3D acoustic waveform inversion in the Laplace domain using an iterative solver. *Geophysical Prospecting* 59, No.3, p386-399.

Ravaut C., Operto S., Improta L., Virieux J., Herrero A. and P. Dell'Aversana. 2004. Multiscale imaging of complex structures from multifold wide-aperture seismic data by frequency-domain full-waveform tomography: application to a thrust belt. *Geophysical Journal International* 159, 1032-1056.

Riabinkin L.A., Napalkov Yu.V., Znamenskiy V.V., Voskresenskiy Yu.N. and Rapoport M.B., 1962, Teoriya I praktika seysmicheskogo metoda RNP (Theory and practice of the CDR seismic method): Trudy Moskovskogo Instituta Neftekhimicheskoy I Gazovoy Promyshlennosti im, *Gubkina* 39.

Rieber F. 1936. A new reflection system with controlled directional sensitivity. *Geophysics* 1, 97–106.

Shin C. and Cha Y.H. 2008. Waveform inversion in the Laplace domain. *Geophysical Journal International* 173, 922−931.

Shin C. and Cha Y.H. 2009. Waveform inversion in the Laplace-Fourier domain. *Geophysical Journal International* 177, No. 3, 1067-1079.

Shin C. and Ha W. 2008. A comparison between the behavior of objective functions for waveform inversion in the frequency and Laplace domains. *Geophysics* 73, No. 5, VE119-VE133.

Shin C. and Min D.J. 2006. Waveform inversion using a logarithmic wavefield. *Geophysics* 71, R31−R42.

Shin C., Jang S. and Min D.J. 2001. Improved amplitude preservation for prestack depth migration by inverse scattering theory. *Geophysical Prospecting* 49, 592-606

Shin C., Pyun S. and Bednar J.B. 2007. Comparison of waveform inversion, part 1: conventional wavefield vs logarithmic wavefield. *Geophysical Prospecting* 55, 449−464.

Shin J. 2015. Laplace-domain waveform inversion using a single damping constant. PhD Thesis, Seoul National University, KOR.

Shipp R.M. and Singh S.C. 2002. Two-dimensional full wavefield inversion of wide-aperture marine seismic streamer data. *Geophysical Journal International* 151, 325−344.

Shirangi M.G and Emerick A.A. 2016. An improved TSVD-based Levenberg–Marquardt algorithm for history matching and comparison with Gauss–Newton. *Journal of Petroleum Science and Engineering* 143, 258-271.

Sourbier F., Operto S., Virieux J., Amestoy P. and L'Excellent J.Y. 2009. FWT2D: A massively parallel program for frequency-domain full-waveform tomography of wide-aperture seismic data, Part 2: Numerical examples and scalability analysis: *Computers & Geosciences* 35, 496-514.

Sword C.H. 1984. The method of controlled directional reception. SEP-41, Stanford University, 369-393.

Sword C.H. 1986. Tomographic determination of interval velocities from picked reflection seismic data. *Expanded Abstract of SEG 56th Annual International Meeting*, Houston, Soc. Expl. Geophys., Expanded Abstracts, 657-660.

Sword C.H. 1987. Tomographic determination of interval velocities from reflection seismic data: The method of controlled directional reception. PhD Thesis, Stanford University, USA.

Symes W.W. 2008. Migration velocity analysis and waveform inversion. *Geophysical Prospecting* 56, 765-790.

Symes W.W. and Carazzone J.J. 1991. Velocity inversion by differential semblance optimization. *Geophysics* 56 (5), 654-663.

Tarantola A. 1984. Inversion of seismic reflection data in the acoustic approximation. *Geophysics* 49, 1259–1266.

Tsingas C., Kim Y. and Yoo J. 2015. Broadband Acquisition, Deblending and Imaging Employing Dispersed Source Arrays. *EAGE conference 2015*.

Warner M., Ratcliffe A., Nangoo T., Morgan J., Umpleby A., Shah N., Vinje V., Štekl I., Guasch L., Win C., Conroy G. and Bertrand A. 2013. Anisotropic 3D full-waveform inversion. *Geophysics* 78, No.2, R59–R80.

Woodward M., Nichols D., Zdraveva O., Whitfield P. and Johns T. 2008. Adecade of tomography. *Geophysics* 73, No.5, VE5-VE10.

Worthington M.H. 1984. An Introduction to geophysical tomography. *First Break* 2(11), 20-26.

Yilmaz O. and Chambers R., 1984, Migration velocity analysis by wave-field extrapolation, *Geophysics* 49, No. 10, 1664-1674.

Zelt C.A. and Barton P.J. 1998. Three-dimensional seismic refraction tomography: A comparison of two methods applied to data from the Faeroe Basin. *Journal of Geophysical Research* 103, 7187-7210.

초 록

박은진
협동과정 계산과학전공
서울대학교 대학원

CDR(Controlled Directional Reception) 방법은 파선 추적을 이용한 속도 분석법이다. 이는 기울기값(slope) 또는 파선 매개변수(ray-parameter)를 이용한 토모그래피 방법 중 하나이기 때문에 “슬로프 토모그래피 방법(slope tomography method)”이라고도 불린다. 이 방법은 주시 토모그래피처럼 사전 피킹(pre-picking) 작업이 필요하지 않다. 국소 경사 중합(local slant stack)으로부터 자동추출된 정보는 탄성파 자료에서 직접 추출한 반사 주시보다 더 신뢰성 있다. 또한 MVA(Migration-based Velocity Analysis)에서의 이미징 연산자보다 좀 더 세밀한 무브아웃 정보를 제공한다. 그러므로 이 논문에서는 strip-off CDR 속도 분석법을 이용하여 매크로 속도모델을 구축했다. 기존의 CDR 방법과 비교했을 때 공통수신원모음(CRG, common receiver gathers) 자료의 정확도를 높이고 컴퓨터 저장용량을 줄였다. 또한 속도분석 과정에서 마이그레이션 이미지를 배경 패널로 사용함으로써 속도모델의 정확도를 높였다.

이 방법을 통해 얻은 결과는 완전파형역산의 초기속도모델로 사용되었다. 완전파형역산에서 좋은 초기속도모델은 불안정성을 줄이고 전역 최소값(Global minimum)에 수렴할 확률을 높여주기 때문에 매우 중요하다. CDR 로 얻은 속도모델이 완전파형역산의 초

기모델로 적용되는 것은 처음이기 때문에 큰 의의가 있다. 기존의 라플라스 역산 모델과 단순 선형 증가 모델을 초기속도로 한 역산 결과와 비교했을 때 CDR 방법이 좋은 결과를 보인다는 것을 실제 구조와 비슷한 두 합성 자료를 통해서 검증했다. 그리고 CDR 매크로 모델은 풍화대나 짧은 오프셋을 가지는 탄성파 자료에 대해서 강점을 가진다는 것도 확인했다. 또한 이 방법을 다변수 역산에도 적용할 수 있었다. 마지막으로, 실제 탄성파 탐사자료에 대해서도 속도모델링을 수행해보았다. 실제 탐사자료는 속도모델의 참값을 알 수 없기 때문에 정확히 비교하기는 힘들지만 RMS 에러를 통해서 CDR 모델의 역산 결과가 좋음을 간접적으로 확인할 수 있었다. 또한 키르히호프 마이그레이션 결과와 그 것의 공통이미지모음(CIGs, common image gathers)을 통해서도 역산된 CDR 속도모델이 좋은 결과를 보인다는 것을 증명했다.

이 논문에서 쓰인 strip-off CDR 속도 분석법은 라플라스 영역 파형역산보다 계산 시간이 오래 걸린다는 단점이 있다. 하지만 이 방법은 계산 시간이 더 크더라도 높은 정확도를 가진다는 것에 큰 가치가 있다. 특히 풍화대나 짧은 오프셋을 가지는 탄성파 탐사자료와 같이 기존 방법으로 정확도를 높이기 힘든 자료에서 좋은 결과를 줄 것으로 기대된다. 또한 이 방법은 일부 자원 탐사나 지질조사와 같이 빠른 계산 시간보다 높은 정확도를 선호하는 작업에서 유용하다. 게다가 좋은 초기 속도 모델은 완전파형역산 과정에서 정확도를 높여줄 뿐만 아니라 계산 시간을 줄여주기도 한다.

종합하면, 이 논문에서 얻어진 CDR 매크로 모델은 주파수 영역 완전파형역산에 적합하다. 앞으로 복잡한 지형에서의 탐사나 3차원 탐사가 늘어나면서 오프셋 또는 기록시간이 짧은 탄성파 자

료들이 생겨날 것인데, 이 방법은 이런 자료에 대해 강점을 보일 것이다. 또한 이 것은 앞으로 육상 탐사 자료나 해저면 시스템으로 얻어진 탐사 자료에도 적용할 수 있으며 다변수 역산과 같은 다른 역산 영역으로 확장할 수 있을 것으로 기대된다.

주요어 : Controlled directional reception (CDR), 속도 분석, 초기 모델, 완전파형역산, 파선 매개변수
학 번 : 2012-30115